Università degli Studi di Napoli *Federico II*

DOTTORATO DI RICERCA IN

FISICA

Ciclo *XXXI*

Coordinatore: prof. Salvatore Capozziello

Search for exotic neutrino sources with the KM3NeT telescope

Settore Scientifico Disciplinare FIS/04

Dottorando
Rosa Mele

Tutore
Prof. Pasquale Migliozzi

Anni 2015/2018

Contents

List of Figures

List of Tables

List of Acronyms

AC Alternating Current. , 44

ADC Analog-to-Digital Converter. , 38

AGN Active Galactic Nuclei. iii, 9, 10, 9

AMANDA Antarctic Muon And Neutrino Detector Array. , 29

ANTARES Astronomy with a Neutrino Telescope and Abyss environmental RESearch. i, ii, iv, vi, ix, 1, 2, 3, 28, 33, 34, 35, 36, 37, 38, 39, 38, 40, 41, 42, 43, 44, 46, 41, 48, 50, 51, 56, 51, 81, 82, 83, 85, 83, 87, 88, 89, 97

ARCA Astroparticle Research with Cosmics in the Abyss. vii, 43, 51, 93

ARS Analogue Ring Sampler. , 38

ASCII American Standard Code for Information Interchange.

BDUNT Baikal Deep Underwater Telescope. , 28

BR Branching Ratio. , 25

CC Charged Current. , 22, 23, 24, 51, 54, 55

CMB Cosmic Microwave Background. , 6, 10, 14

CORSIKA COsmic Ray SImulations for KAscade. , 56

cps Counts Per Second. v, ix, , 65, 73

CPU Control Processing Unit. , 57

CR Cosmic Ray. iii, 5, 6, 7, 8, 9, 10, 14, 10, 26

DAQ Data Acquisition. , 38

DC Direct Current. , 44, 70

DM Dark Matter. ii, vi, 90, 91, 93, 95, 99

DOF Degree Of Freedom. , 83

DOM Digital Optical Module. iv, 29, 40, 41, 43, 44, 41, 51, 58, 73

DU Detection Unit. iv, 43

DUMAND Deep Underwater Muon and Neutrino Detection. , 28

DWDM Dense Wavelength Division Multiplexing. , 38, 44

EDFA Erbium-Doped Fiber Amplifier. , 44

EG Extra Galactic. , 90, 91

EM Electromagnetic. , 24, 56, 57, 58

ESA European Space Agency. iii, , 8

FPGA Field Programmable Gate Array. , 69

FWHM Full Width at Half Maximum. , 41, 65, 71, 74

GENHEN GENerator of High Energy Neutrino. ii, v, , 1, 51, 53, 54, 55, 51, 97

GPS Global Positioning System. , 33

GRB Gamma Ray Burst. , 9, 10, 38

GZK Greisen-Zatsepin-Kuz'min. , 6, 7

HEGRA High Energy Gamma Ray Astronomy. iii, , 10

HESE High Energy Starting Events. ix, 81, 83

HV High Voltage. v, , 41, 44, 65, 69, 70, 71, 72, 73

IC Inverse Compton. , 10

JB Junction Box. , 33

KS Kolmogorov-Smirnov. , 88

LAT Large Area Telescope. iii, , 10

LCM Local Control Module. , 33, 38

LED Light-Emitting Diode. iv, , 29, 35, 36, 41

LIGO Laser Interferometer Gravitational-Wave Observatory. , 1

MC Montecarlo. , 56

MDP Model Discovery Potential. , 92, 93

MEOC Main Electro-Optical Cable. , 33

MILAGRO Multiple Institution Los Alamos Gamma Ray Observatory. iii, , 10

MLCM Master Local Control Module. , 38

MUM MUons+Medium. , 51

MUPAGE MUon GEnerator for neutrino telescopes based on PArametric formulas. , 51, 56

MUSIC MUon SImulation Code. , 51, 56, 58

NASA National Aeronautics and Space Administration. iii, , 8

NC Neutral Current. , 22, 24, 54, 55

NEMO Neutrino Mediterranean Observatory. iv, , 28, 40

NESTOR Neutrino Extended Submarine Telescope with Oceanographic Research Project. iv, , 28, 40

NFW Navarro-Frenk-White. , 91

NS Neutron Star. , 8

NT Neutrino Telescope. , 88

OM Optical Module. , 33, 36, 38, 40, 57

OMF Optical Module Frame. , 33

ORCA Oscillation Research with Cosmics in the Abyss. , 43

p.e. Photoelectron. , 38, 58

PDF Portable Document Format.

PDF Probability Density Function. , 91

PMNS Pontecorvo-Maki-Nakagawa-Sakata. , 21

PMT Photomultiplier. ii, iv, v, vi, ix, 1, 26, 29, 33, 35, 36, 37, 38, 40, 41, 44, 45, 41, 51, 58, 65, 66, 67, 66, 67, 69, 70, 71, 70, 71, 72, 73, 74, 75, 74, 75, 76, 75, 77, 75, 77, 97

PWNe Pulsar Wind Nebulae. , 8

QE Quantum Efficiency. , 65, 70

QGSJET Quark Gluon String with JETs. , 12

R&D Research and Development. , 28, 33, 35

S/N Signal-to-Noise ratio. , 45

SMBH Super Massive Black Hole. , 9

SNR Supernova Remnant. iii, 8, 10, 8, 10

SPE Single PhotoElectron. ix, , 38, 65, 72, 74, 76

ToT Time over Threshold. vi, 69, 72, 76

TT Transit Time. vi, 74, 76

TTS Transit Time Spread. , 74

TVC Time-to-Voltage Converter. , 38

U.S. United States. , 28

UHECR Ultra High Energy Cosmic Ray. , 9

UV Ultraviolet. , 9

w.e. Water Equivalent. , 56

XML Extensible Markup Language. , 70

Introduction

The neutrino represents the ideal astronomical messenger. Neutrinos travel large distances without absorption and with no deflection by magnetic fields. Having a very small mass and no electric charge, the neutrino is similar to the photon as an astronomical messenger, except for the fact that it interacts on weakly with the matter. For this reason, high energy neutrinos may reach us unscathed from cosmic distances revealing the proprieties of their sources. On the other hand, their weak interactions also make cosmic neutrinos very difficult to detect.

In 1960, Markov suggested to detect high energy neutrinos using huge volumes of transparent natural material such as ice or water. High energy astrophysical neutrinos would weakly interact with one of the nucleons of the medium producing charged particle that emit Cherenkov photons which can be detected by a lattice of photomultipliers. The charged produced particles have almost the same direction of the generating neutrino and this allows to point back to the neutrino sources if the muon direction can be precisely reconstructed. The low cross section of the ν interactions and the very low predicted astrophysical neutrino flows suggest that these Cherenkov detectors should be very large, on the scale of km^3.

The ANTARES neutrino telescope, a three dimensional array of photomultipliers distributed over 12 lines, installed in the Mediterranean was completed in May 2008. It is taking data continuously since then. The main goal of the telescope is the search for high energy neutrinos from astrophysical sources. Its position in the Northern hemisphere and the possibility to look at the Galactic Centre has made it especially useful since it is complementary to the IceCube Antarctic telescope. This complementary view can provide a different insight in the cosmic signal observed only by the IceCube Collaboration.

In 2017 the IceCube neutrino telescope detected a high energy neutrino event coincident in direction and time with a gamma ray flare from the blazar TXS 0506+056 with a 3.5σ evidence. This confirms that blazars are sources of the high energy astrophysical neutrino flux and encourages the search for neutrinos from other types of astrophysical sources. Recently the IceCube, LIGO, Virgo, and ANTARES collaborations have used data from the two neutrino detectors to search for coincident neutrino and gravitational wave emission from transient sources. This study despite

having only provided a constraint on the density of these sources, marked the birth of the multimessenger astronomy that is the only path towards a deep understanding of the extreme universe. The detection of both gravitational waves and neutrinos from the same source would set a new milestone in multimessenger astronomy since it will allow a better knowledge of the processes inside the source. The joint detection would also significantly improve the localization of the source and make faster and more precise electromagnetic follow-up observations.
The encouraging results of ANTARES and IceCube during their data taking, the importance of synergy between neutrino telescopes in two different hemispheres and the advent of the multimessenger era have suggested the design of a new generation telescope in the northern hemisphere. The new telescope has to be larger than its predecessor ANTARES but must exploit all the experience acquired during the years of ANTARES operations. This new generation telescope, KM3NeT is under construction and will become the largest telescope for neutrinos in the World.
In this thesis, we studied the contribution of a combined analysis of of Icecube and ANTARES data in order to exclude the scenario for which the neutrinos detected by the two telescopes derive from a single power law model. The possibility of detecting the presence of neutrinos generated from the decay of Dark Matter particles with the new generation KM3NeT telescope was then investigated.
The last analysis requires the development of a very detailed Montecarlo code for which the potential of the simulation code currently used by the ANTARES and KM3NeT collaborations has been increased integrating the GENHEN code with the tauonic neutrino regeneration process.
Since the "eyes" through which the new generation KM3NeT telescope would scrutinize the presence of neutrinos "beyond the single power law" are the PMTs, we perform and complete characterization of the aforesaids in order to measure their characteristics. This will allow to improve the analysis and to correctly simulate their response in the Montecarlo code. The thesis is organized as follows:

- Chapter 1 presents a summary of the present knowledge of cosmic ray physics and the gamma ray astronomy and their connection to the neutrino astronomy.

- Chapter 2 gives a description of the propagation and detection neutrino mechanism and describes the characteristics and the potentiality of the main neutrino telescopes.

- Chapter 3 is dedicated to the description of the ANTARES and KM3NeT detectors.

- Chapter 4 describes the simulation codes used in this work to perform a complete simulation of the incident muon neutrinos underling my contribution in adding the complete regeneration ν_τ process.

- Chapter 5 describes the experimental setup and the analysis that allowed for the complete characterization of the KM3NeT photomultipliers.

- Chapter 6 reports our combined analysis of ANTARES and IceCube data for the test of the "single power law scenario" and a feasibility study for the search of neutrinos produced by dark matter decay with the new generation KM3NeT Neutrino Telescope.

1 Neutrino astrophysics

The CRs were discoverded in 1912 by Victor Hess [1] who measured the increment of natural radiation with the altitude using electroscopes on free balloon flights. The nature of this ionising radiation was debated a lot and in 1930 Rossi [2] and others demonstrated an east-west effect that suggested the idea that the cosmic rays were charged and mostly positive. After a brief description of the composition of cosmic rays (sec. 1.1) and of the sources of both CRs (sec. 1.2) and γ-rays (sec. 1.3), in section 1.1 we will discuss in detail about CRs origin, composition and energy spectrum.
The observation of CRs on Earth suggests the idea of the existence of cosmic accelerators in and outside our Galaxy which were the only source of high energy particles until the building of particle accelerators. This sources were and will be a very useful instrument for a deep knowledge of the particles proprieties.
The collisions of CRs in in the immediate vicinity of the source produce with great probability neutrinos. Neutrinos are neutral and weekly interacting particles and for these reasons they travel great distances carrying a trace of the direction of the source. In section 1.4 we will explain the mechanisms of neutrino production and the CR-neutrino connection which is examinated in details in [3].

1.1 Cosmic Rays composition and spectrum

The particles reaching the top of atmosphere are protons (90%) but there is a $\sim 9\%$ of α particles accompanied by heavier nuclei, electrons, γ-rays and a small quantity of antimatter.
The energy spectrum of the primary CRs covers a range from less than 10^9 to $\sim 10^{20}$ eV and the determination of CRs composition can be determinated with different techniques depending on their energy.
The direct composition measure is possible for CRs with energy below 10^{14} eV but at higher energies only indirect measurements are available because the flux is too low to collect enough statistics due to the small size of the detectors. For higher energies the detection involves very large ground array detectors that observe the particles of the extensive showers generated in the interaction of a primary CR with air nuclei in the atmosphere. These indirect measurements seem to confirm that, for energies above 10^{14} eV, CR composition becomes heavier [4].

From these measurements the energy resulting spectrum, showed in Fig. 1.1, follows an unbroken power law:

$$\frac{dN}{dE} \propto E^{-\gamma} \tag{1.1}$$

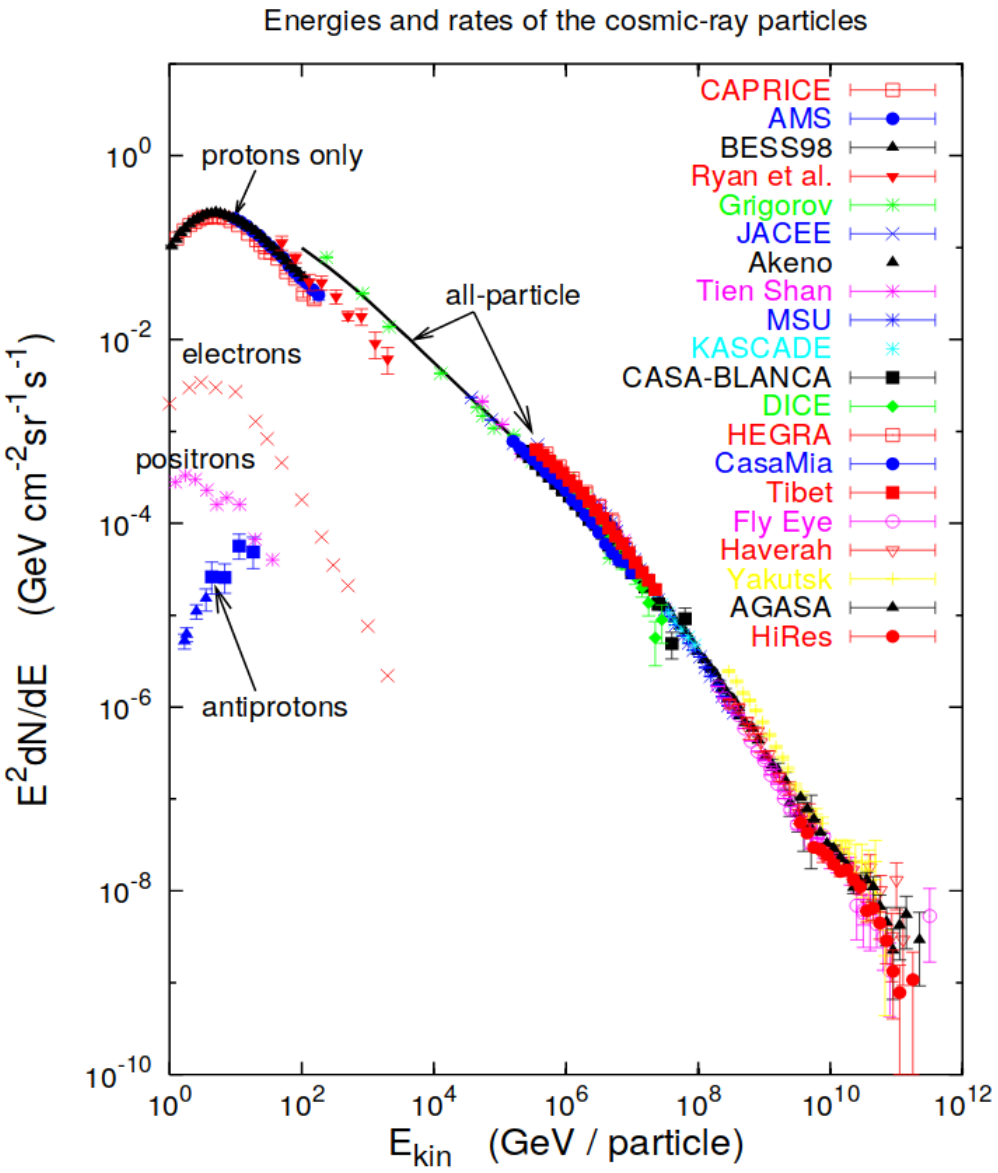

Fig. 1.1: Cosmic ray energy spectrum from 1 to 10^{12} GeV as measured by different experiments. The spectrum is multiplied by E^2 to better show its features as the knee, the ankle and a ultra-high energy cut-off [5].

The energy spectrum shows at least two changes of slope. The first one, referred as *knee* is around 10^{15} eV and the second one, called *ankle* above $10^{18.5}$ eV. The spectral index, referred as γ in eq. 1.1, has a value of ≈ 2.7 up to the knee and then rises to a value ankle, $\gamma \simeq 2.7$ and presents a cut-off at higher energies.

The change of energy spectrum slope in the knee region is still an open question, and many models have been proposed to explain this steepening [6].
The presence of different nuclear species at the galactic acceleration sites (see section 1.2) can be translated into a different cut-off energy that would be visible in a transition from a proton-rich to an iron-rich composition at the knee.
Around $10^{18.5}$ eV is visible the so-called *ankle*, where the spectrum flatten and this feature is usually attributed to a transition from galactic to extra-galactic sources of cosmic rays [7].
The CRs interaction with the Cosmic Microwave Background (CMB) photons would limit the energy of cosmic rays at about $6 \cdot 10^{19}$ eV, in the hypothesis n which the interacting particles are protons. This upper limit is called Greisen-Zatsepin-Kuz'min (GZK) effect [8, 9].
The direction of the cosmic rays arriving at the top of the atmosphere is isotropically distributed due to the presence of galactic ($\simeq 4\mu$G) and extra-galactic magnetic field. The Larmor radius:

$$R_L = \frac{mv_\perp}{|q|B} \tag{1.2}$$

of a proton in the galactic magnetic field becomes compatible with the Milky Way radius ($\simeq 200$ pc) only if its energy is above 10^{18} eV. Particles with lower energy or higher charge are deflected many times by the irregularities of the magnetic field and so confinated in the Galaxy.
The deflection of charged particles due to the Galactic field and the GZK effect make it impossible to reveal CRs point back to their sources suggesting the search for other particles emitted by the same sources such as neutrinos.

1.2 Cosmic ray sources

The acceleration process of CRs through iterative scattering processes was firstly suggested by Enrico Fermi [10, 11]. Shock waves can be produced in extreme environments such as in the proximity of black holes or after the collapse of a massive star.
In the process referred to as the Fermi second order acceleration, iterative acceleration can be explained if we assume that a particle, trapped in magnetic field inhomogeneities, increases its energy by $\Delta E = \epsilon E$ each time encounters the shock wave. The gain ϵ is proportional to β^2 in which β is the cloud velocity in units of c since it is due to the relative movement of the shock wave with respect to inhomogeneities. If the particle encounters a plane shock front the mechanism, referred as first order acceleration, it is more efficient since it is proportional to β.
The particles accelerated by Fermi acceleration mechanism have a energy spectrum described by an unbroken power law with a spectral index $\gamma \sim 2$.

The proprieties of the accelerator sites in terms of size and magnetic field are related to the energy reached by the cosmic rays as graphically described in the *Hillas plots* (Fig. 1.2).

These plots show that fixing the size of the accelerating site, higher magnetic field means a longer confinament and a further acceleration through Fermi mechanisms. At fixed magnetic field intensity, a larger site means that more encounters with the accelerating shocks are possible. A more compact object would require a higher magnetic field intensity to accelerate a CR to the same energy as a larger source.

1.2.1 Galactic sources

Supernova remnants are astrophysical sources in which the Fermi acceleration mechanism is believed to occur. A supernova is an astronomical event that occurs in the last part of massive star's life, characterized by an explosion that causes the appearance of a bright transient, visible for only several weeks or months and leaving a SNR. The SNR is surrounded by an expanding shock wave, and is composed by the material ejected and expanding from the explosion and the interstellar material. SNRs can accelerate nuclei up to $E^{max} \sim 300 \times Z$ TeV that is the energy at which a change of slope appears in the CRs energy spectrum explaining the transition over the knee as a Z dependence of the maximal energy at which cosmic rays can be accelerated by SNRs (Fig. 1.3).

Higher energies are possible if different mechanisms, providing further particle acceleration, are taken into account. A Neutron Star (NS) with a strong magnetic field can work as an additional particle accelerator if is present in the SNR environment. These object are also called Pulsar Wind Nebulae (PWNe). The presence of a proton with energies larger than 1 TeV component in the pulsar winds is still an open question but it is not excluded. The central region of our Galaxy is itself one of the possible CRs accelerator. This region has the highest density in the Galaxy and it includes the central Black Hole and several TeV γ-ray sources.

The Fermi bubbles [13] are two large structures near the Galactic center, above and below the galactic plane (Fig. 1.4). These structures are characterized by a γ-ray emission in the GeV range with a spectrum $\propto E^{-2}$ and a constant intensity over the whole spatial emission region. The Fermi bubble emission is explicated by several models [14, 15, 16] with the decay of neutral and charged pions produced during the collisions of CRs with the surrounding material. In this hypothesis the neutral pion decay would explain the gamma flux but this is associated to a neutrino flux.

Another possible class of CRs accelerator in our Galaxy is the one of microquasar or radio emitting X-ray binary system. Microquasars are compact objects (stellar-mass black holes and neutron stars) that have, on a smaller scale, some characteristic in common with quasar like strong and variable radio emission, an accretion disk surrounding system of compact objects like neutron stars or black holes with a mass

of few solar masses. In microquasars the accretion disk is very luminous and the accreted mass ensues from a normal star. The composition of the jets, and so the chance to realize an hadronic scenario, is still an open question [17].

1.2.2 Extra-galactic sources

AGN are considered the most powerful sources of radiation in the Universe. In the galaxies center is often present a Super Massive Black Hole (SMBH). AGN is the visible emission region around the SMBH, characterized by jets of particle and radiation due to accreting process. The AGN can be even more luminous than its host galaxy if its direction emission coincides with the line of sigth of the observer. A large variety of objects can be classified as AGNs because, it is possible to observe the same kind of objects from different angles as explained in Fig. 1.5. One type of AGN is called a quasar. They are very powerful sources of radiation, sometimes having luminosities thousands of times greater than entire galaxies. Nowadays we know these objects are actually the nuclei of galaxies with feeding supermassive black holes at their centers. These supermassive black holes swirl the nearby gas and dust into an accretion disk and often emit jets of particles away at nearly the speed of light. If one of these jets happens to be pointing directly at the Earth we call it a blazar.

Until today no correlation between the arrival direction of Ultra High Energy Cosmic Rays (UHECRs) and AGNs has been found [18].

Gamma Ray Bursts (GRBs) are cosmic events with a duration that goes from ms to few minutes and are characterized by an extremely bright γ-ray emission characterized by a typical energy release of 10^{51} erg, which allows to classify them among the most energetic phenomena in the Universe. The first emission is followed by an afterglow in X, UV and optical radiation. The GRBs can be classified on the basis of the burst duration in *short* (below few seconds of duration) and *long*. The first group is belived to be generated by the merging of two neutron stars or of a neutron star and a black hole. The GRB emission from neutron star merger has been somehow confirmed since, GRB 170817A, was detected by the Fermi and INTEGRAL spacecraft beginning 1.7 seconds after the GW170817 merger signal [19]. Long GRBs could be generated by a supernova collapse of extremely massive stars.

The accepted model for the description of the steady emission and the subsequent afterglow os the fireball model [20]. The jet made of highly relativistic material with Lorentz boost larger than 100-200 is activated by a huge release of gravitational energy and moves through a dense environment producing shocks and γ-rays through synchrotron processes and inverse Compton effect. The afterglow emission, at lower frequencies, is caused by the time-delayed interaction of the jet with the surrounding medium. The hypothesis of a CRs acceleration is supported by the presence of

extremely fast shocks with high Lorentz boost that can enhance the maximal energy of accelerated particles and make them reach the upper end of the CR spectrum.

1.3 γ-rays sources

The source described above can produce also γ-rays by means of two mechanism: leptonic or hadronic processes. Leptonic mechanisms, like synchrotron radiation emission, bremsstrahlung and Inverse Compton (IC) scattering [21], occur when near the source there are high energy electrons accelerated. The synchrotron emission is present when there is a strong magnetic field that causes a deflection of the electrons. the bremsstrahlung is verified when a relativistic electron interacts with the electric field of nuclei in the medium while IC is related to the inelastic scattering of fast electrons on local photons. The leptonic models can explain the most of the electromagnetic radiation from cosmic sources.
Hadronic mechanisms are due to the interaction of CR with the nuclei in the surrounding of the source. These interactions produce neutral mesons π^0 that immediately (mean lifetime 8.4×10^{-17}s) decay in two photons:

$$\begin{aligned} p + N &\rightarrow X + n\pi^0 \\ \pi^0 &\rightarrow \gamma\gamma \end{aligned} \tag{1.3}$$

The γ-ray spectrum from hadronic production is very similar to the one of the primary CR at the acceleration site, with a spectra index in $[2.0, 2.5]$, since the protons are not absorbed before interacting and generating protons. The photons produced by hadronic interactions should be higher in energy than the ones produced in the leptonic scenario as confirmed by the Fermi/LAT satellite experiment [22]. The Fig. 1.6 shows the spectral energy distribution of the SNR W44, for which is excluded the leptonic emission as the main contribution to the γ-ray emission. Fig. 1.7 shows a γ-ray sky map built through Fermi/LAT observations [23]. This map, centred at the Galactic Centre, shows an enhanced emission in the Galactic Plane in which once extracted the individual point sources is possible to isolte a diffuse component. Fig. 1.8 shows the different contributions to the γ-ray spectrum for the Galactic Plane as measured by Fermi-LAT. A quite strong discrepancy between observed data and models is present at high energies. An increasing flux at high energies could be produced considering the possible influence of cosmic rays accelerated by young sources referred as *fresh*[24].

1.4 Neutrino-cosmic ray connection

Encouraged by the Icecuce neutrino flux observations [25], several hypotheses have been proposed to explain the source of high energy neutrinos and their mechanism of production. The most realistic hypothesis has an astrophysical character and supposes a connection between CRs and neutrinos. The CRs can collide with the material surrounding their sources producing unstable mesons. The decay of these particles produces at the same time neutrinos and gamma rays. The two most plausible neutrino production scenarios are the collisions between accelerated protons and target protons (pp interaction) and the collision between accelerated protons and target photons ($p\gamma$ interaction). In our Galaxy, in the disk or in the halo, where the density of gas is respectively 1 nucleon/cm^3 and $10^{-2} \div 10^{-3}$ nucleons/cm^3, pp-interaction are favorite but in extragalactic sources, such as AGN or an GRB in which a large amount of radiation is present, it is easier to realize a $p\gamma$ interaction. This type of interaction can occur also between protons and the photons of the CMB producing the so-called *cosmogenic neutrinos*. In the following we will analyze how neutrinos are produced and the relationship between neutrinos an CRs energy. We will consider the scenario is which mesons, pions in particular, are produced in the collisions between accelerated protons and the surrounding particles and decay into neutrinos and electrons (positrons) if charged, and gamma rays if neutral.

1.4.1 Pion Decay

To understand the connection between the primary cosmic ray spectrum and the neutrino energy spectrum we will consider the case of the decay of π^+ in neutrino. The same considerations can be done with the negative meson replacing neutrinos with antineutrinos and vice versa. In the decay

$$\pi^+ \rightarrow \mu^+ \nu_\mu \tag{1.4}$$

the energies acquired by the lepton and by the neutrinos are:

$$E_\mu = \left[1 - \left(\frac{m_\mu}{m_\pi}\right)^2\right] m_\pi \simeq 0.79 m_\pi$$

$$E_{\nu_\mu} = \left[1 - \left(\frac{m_{\nu_\mu}}{m_\pi}\right)^2\right] m_\pi \simeq 0.21 m_\pi$$

The lepton produced in 1.4 soon decays giving:

$$\mu^+ \rightarrow e^+ \overline{\nu}_\mu \nu_e \tag{1.5}$$

The energy of the particles produced is about 1/3 in the rest frame. Since the muon takes about 3/4 of the pion's energy in 1.4, the total energy acquires is $\simeq 1/4$ of the total pion's energy.
The flavor composition of neutrinos obtained at the end of the decay chain is equal to :

$$(\nu_e \ : \ \nu_\mu \ : \ \nu_\tau) = (1 \ : \ 2 \ : \ 0)$$

1.4.2 pp Mechanism

The pp-interactions create mostly charged and neutral pions with a smaller contribution of kaons. An accurate calculation of neutrino spectra from pp-interaction requires strong numerical calculations, already implemented in some codes like Pythia [26],SIBYLL [27] and QGSJET [28] based on phenomenological models of pp-interactions. Although through these codes it is possible to calculate the expected photon spectrum, some considerations can easily allow to find the correspondent neutrino spectrum:

1. The interactions between relativistic protons with the protons surrounding create an equal amount of π^+, π^- and π^0 because of the isospin symmetry;

2. The neutrino energy is $\simeq 1/4$ of the generating pion that carries $\simeq 1/5$ of the energy of the primary proton;

3. The neutrino spectra has a shape very similar to the accelerated protons spectrum except for the case in which the primary spectrum shows an energy cut-off.

In the following we will analyze the case in which the energy primary spectrum is a power-law since this simple case occurs in some astrophysical environments in which the Fermi mechanism of acceleration is involved.
In the case in which the proton has a power-law spectrum also pions energy spectrum will be power law distributed. If we consider a pion spectrum with a normalization constant N and a spectral index α :

$$\Phi_\pi[E_\pi] = N E_\pi^\alpha \tag{1.6}$$

we will have a correspondent neutrino spectrum with the same shape but multiplied by a numerical factor

$$\Phi_{\nu_l}[E_{\nu_l}] = N E_{\nu_l}^\alpha \xi_{\nu_l}(\alpha) \tag{1.7}$$

where $\xi_{\nu_l}(\alpha)$ is obtained as (for details see [29]:

$$\xi_{\nu_l}(\alpha) = \int_0^1 f_{\nu_l}(X) X^{\alpha-1} dX \tag{1.8}$$

where f_{ν_l} represents the distribution of the energy carried by a neutrino with respect to the energy of pion in the laboratory frame and $X = \frac{E_\nu}{\pi}$. If $\alpha = 2$, $\xi_{\nu_l}(\alpha)$ represents the average fraction of energy carried by neutrinos. The ξ factors are important to evaluate the flavor composition at the source. The neutrinos coming from pion decay have different energy spectra so we can evaluate the ratio between the ν_μ and the ν_e spectrum :

$$r_{\mu e}(\alpha) = \frac{2\left[\Phi_{\nu_{mu}}[E_{\nu_{mu}}] + \Phi_{\overline{\nu}_\mu}[E_{\overline{\nu}_\mu}]\right]}{\Phi_{\nu_e}[E_{\nu_e}] + \Phi_{\overline{\nu}_e}[E_{\overline{\nu}_e}]} \tag{1.9}$$

The previous ratio can be expressed in terms of the only factors Φ_{ν_l} using the eq. 1.7 and taking into account that $\xi_{\nu_e}(\alpha) = \xi_{\overline{\nu}_e}(\alpha)$:

$$r_{\mu e}(\alpha) = \frac{\xi_{\nu_\mu}(\alpha) + \xi_{\overline{\nu}_\mu}(\alpha)}{\xi_{\nu_e}(\alpha)} \simeq 1.86 - 0.20(\alpha - 2) - 0.02(\alpha - 2)^2 \tag{1.10}$$

This polynomial approximation is valid for α in the range $[1.5, 3]$ and the factor $r_{\mu e}(\alpha)$ decreases at higher values of α and for $\alpha = 2$ the ratio is not so different from 2.

1.4.3 pγ Mechanism

In the case of pγ interation at the source the power law spectrum of accelerated protons is not expected to be reproduced by the spectra of secondary particles. In this case the characteristics of surrounding photons spectrum are relevant to obtain the neutrino spectra. For a simple calculation we will consider the case in which only a resonant barion Δ^+ is produced in the pγ interaction that soon decays into:

$$p\gamma \rightarrow \begin{cases} \Delta^+ \rightarrow \pi^+ n \\ \Delta^+ \rightarrow \pi^0 p \end{cases} \tag{1.11}$$

giving neutral and positive pions. The first decay occurs in $\frac{1}{3}$ of the cases and the second one in $\frac{2}{3}$. The absence of negative pions represents an important difference with respect to the pp interaction. The energy of the two final state particles in the center of mass frame is given by:

$$E_\pi = \left[1 + \left(\frac{m_\pi}{m_\Delta}\right) - \left(\frac{m_\pi}{m_\Delta}\right)^2\right] m_\Delta \simeq 0.22 m_\Delta$$

$$E_n = \left[1 - \left(\frac{m_n}{m_\Delta}\right) + \left(\frac{m_n}{m_\Delta}\right)^2\right] m_\Delta \simeq 0.78 m_\Delta$$

The pion carries about 1/5 of the total energy and the neutron (pion) about 4/5 of it. The pion will soon decays as just discussed in sec. 1.4.2 and the average energy for each neutrino turns out to be about the 1/20 of the primary proton's energy. In this approximation the flavor composition Moreover the flavor composition is approximately the same as for the pp interaction.
The differences between pγ and pp interaction are the following:

- The knowledge of the target photons spectrum is important for the calculation of the neutrino spectrum;

- The neutrino spectrum in the pγ interaction has not a power-law shape but is characterized by a bump due to the peak in the cross section at the energy sufficient for a Δ baryon creation;

- It is more difficult to connect γ-ray spectrum to the neutrino one because since the spectra of neutrinos are not power-law distributed and it is not possible to use the ξ factor like in the previous section. If γ-rays are not absorbed, the ratio between neutrinos and photons flux is smaller than the one in pp mechanism since in the pp scenario two charged pion are produced for each π^0 whereas in pγ scenario the situation is the opposite one because one charged pion is produced each two neutral pions.

- Using this simple approximation, no $\overline{\nu}_e$ are created in pγ interactions and this difference can be useful to discriminate the two mechanisms.

1.5 Neutrino astrophysics

The presence of magnetic fields causes charged particles to not point back to their sources since CRs below 10^{18} eV are unavoidably deflected by galactic magnetic fields. Only for the highest energy CRs is possible to correlate the arrival direction with the source one.
The neutral particles like neutrons, γ-rays and neutrinos, generated in the interactions of CRs with the surrounding medium, carry information from their origin since they are non deflected by the magnetic fields.
Neutrons are short-lived and strongly interacting so they cannot reach the Earth, except if they are very close, and so cannot be detected.
Photons electromagnetic interaction with the interstellar medium and the CMB causes their absorption along their path from the source to the Earth.
Neutrinos are only weakly interacting and can travel cosmic distances without being

absorbed. Observing neutrinos that point in the direction of an astrophysical object is an unequivocal sign that this is an CRs acceleration site.

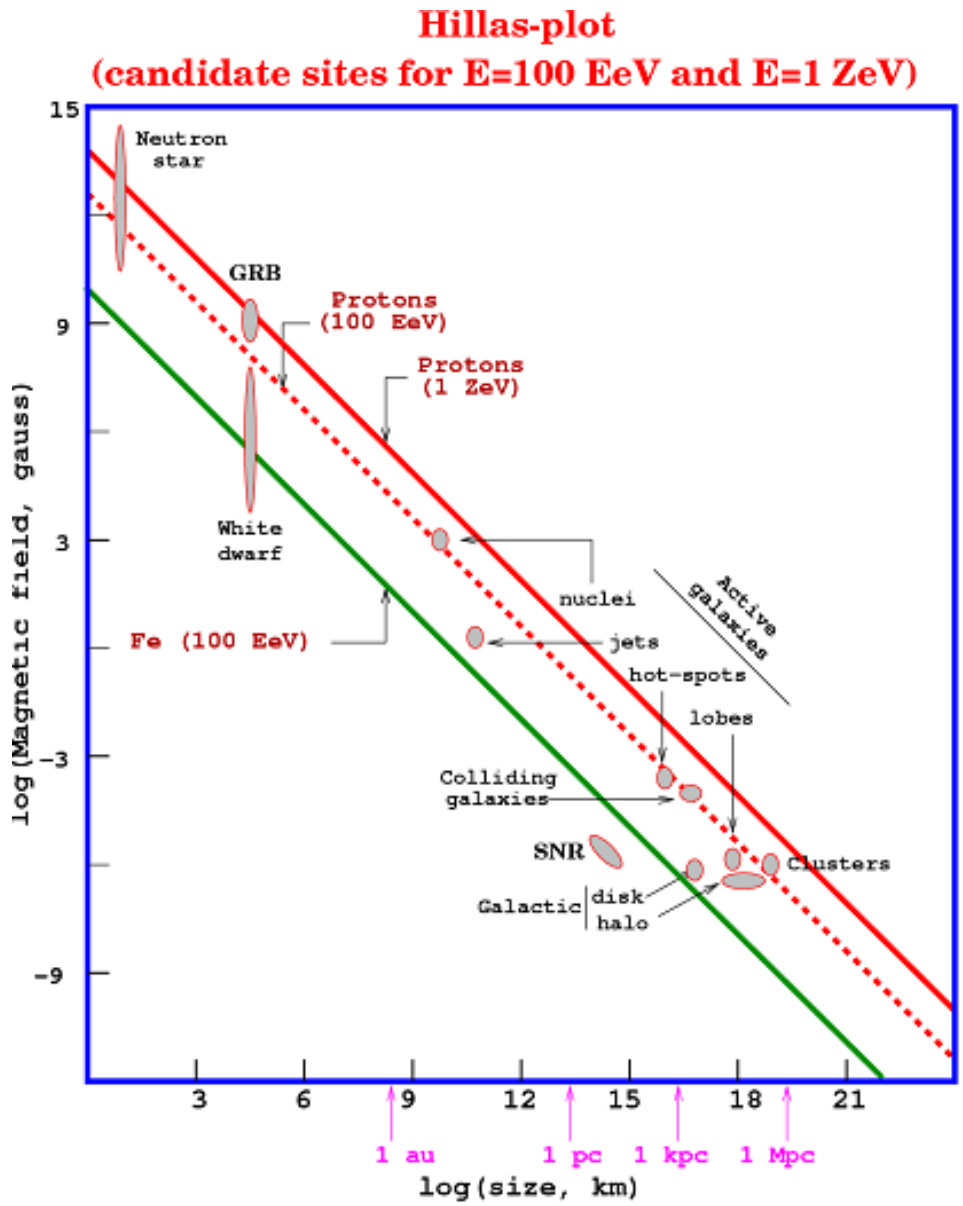

Fig. 1.2: The Hillas plot relates the properties of acceleration sites like size and magnetic field strength to the maximal energy reached by a cosmic ray. Sources above the red solid (dashed) line can accelerate protons up to 1 ZeV (1000 EeV). The green line refers to the acceleration of Iron nuclei up to 100 EeV [12].

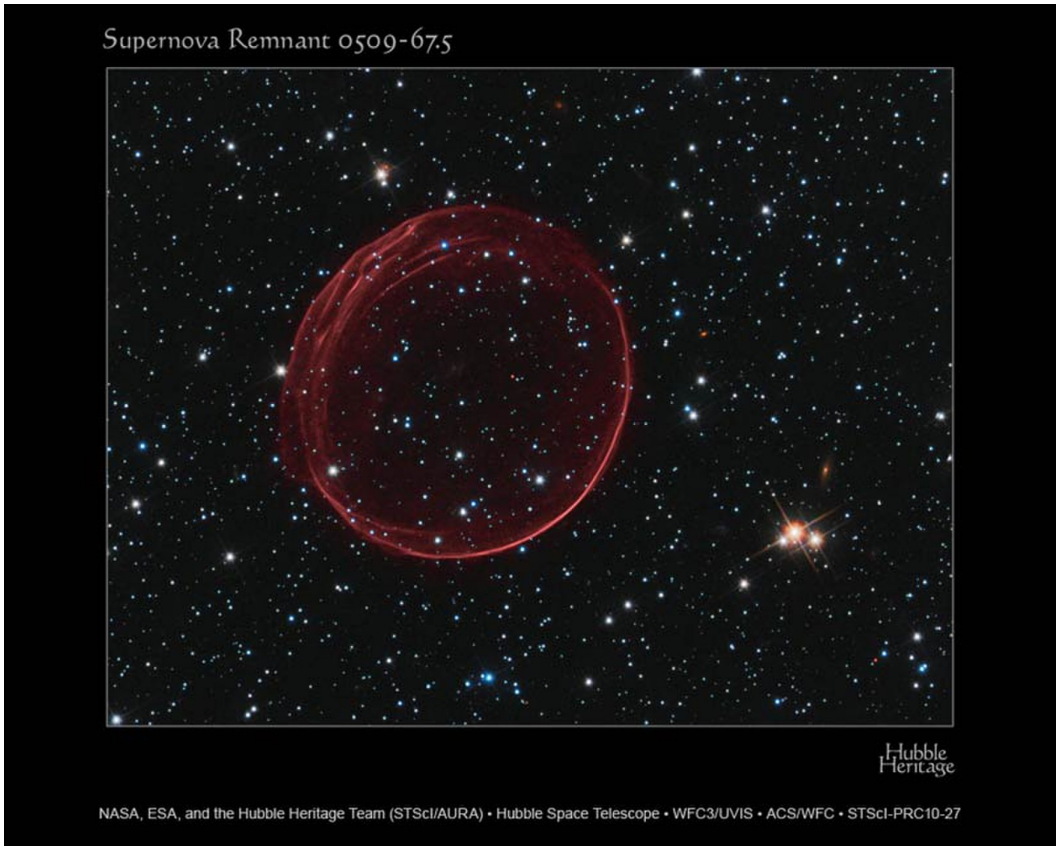

Fig. 1.3: SNR 0509-67.5, the bubble is the visible remnant of a powerful stellar explosion in the Large Magellanic Cloud, a small galaxy about 160000 light-years from Earth. Credit: NASA, ESA, and the Hubble Heritage Team (STScI/AURA).

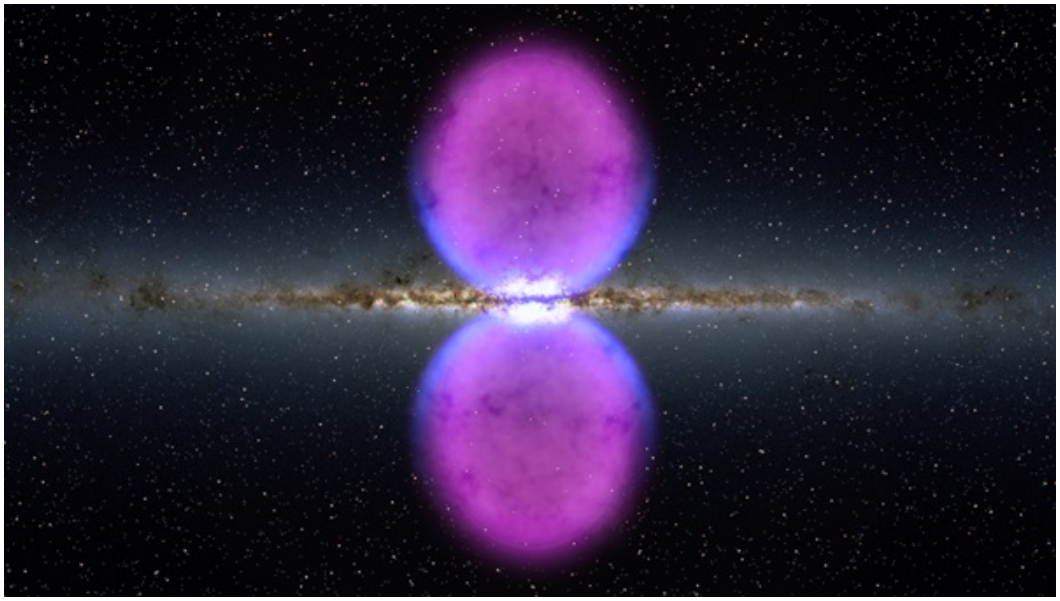

Fig. 1.4: Pictorial illustration of Fermi bubbles. Credit: NASA's Goddard Space Flight Center

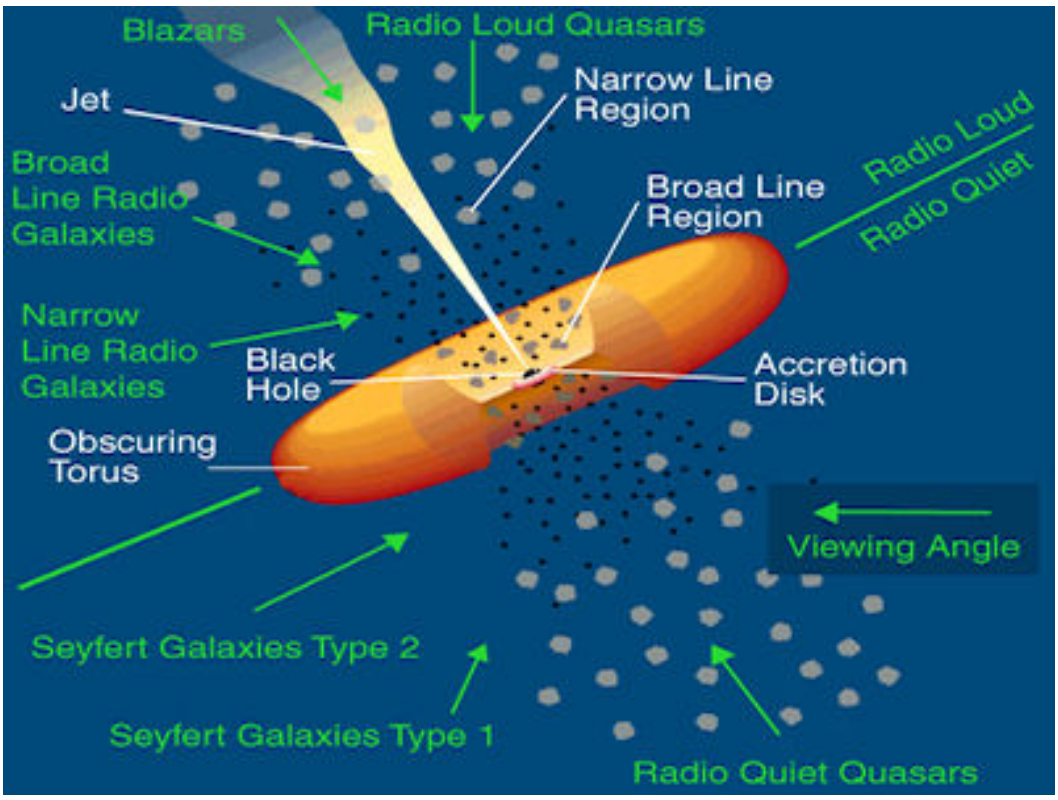

Fig. 1.5: A diagram showing the viewing angles of different AGNs. Credit: Pierre Auger Observatory.

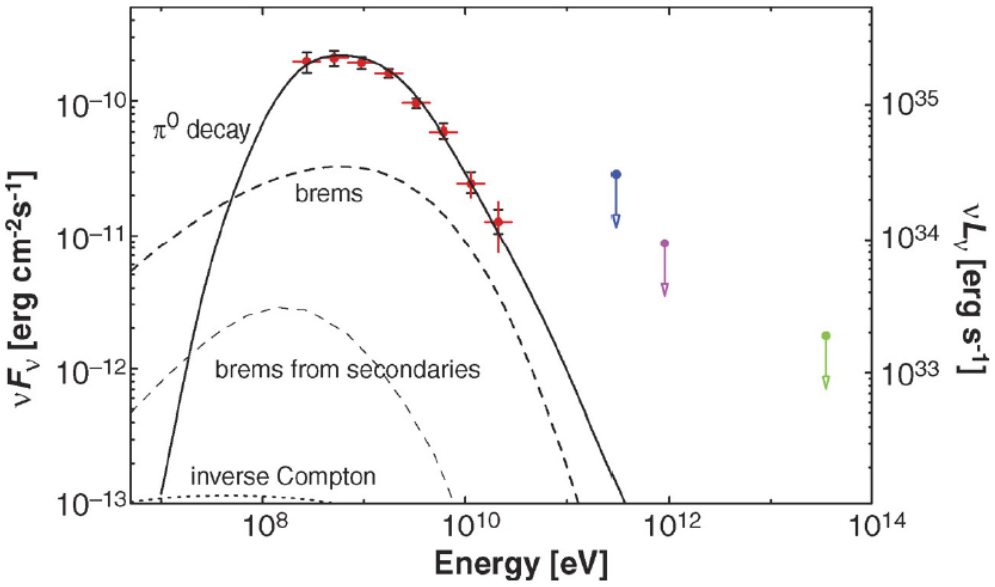

Fig. 1.6: Spectral energy distribution of the SNR W44 as observed by the Fermi/LAT experiment, with the upper limits from the Whipple (blue), HEGRA (magenta), and MILAGRO (green) experiments [22]. The experimental point are compared to the expectations from leptonic emission processes (dashed lines) (mainly from bremsstrahlung) and hadronic emission (solid line) from π^0 decay.

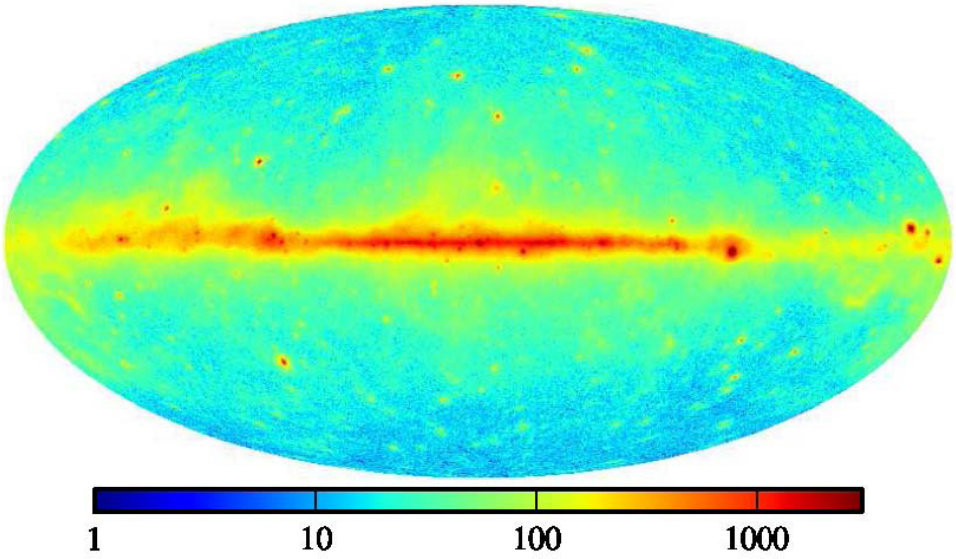

Fig. 1.7: Sky map observed by the Fermi/LAT γ-ray observatory. The color code represents the counting rate of the LAT instrument. Except some strong individual sources, most of the counting rate is related to a diffuse emission in the Galactic Plane [23].

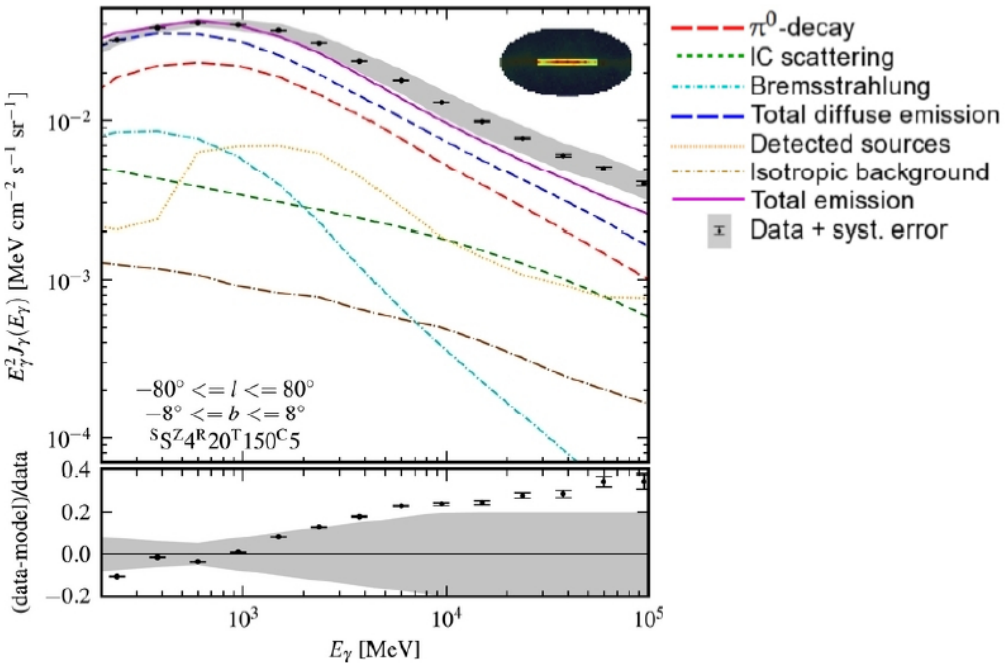

Fig. 1.8: γ ray energy spectrum for the Galactic Plane measured by Fermi/LAT. Color code as in the legend. The decay of the π^0 produced in the CR interactions gives the larger contribution to the emission. The comparison between data and expectations shows a difference at high energies that might be due to an additional component of CRs from young sources [24].

2

Propagation and detection of cosmic neutrinos

One of the most important properties of neutrino is that it interacts only weakly with the matter retaining information on the source. This special property lead us to study and use this particle as a messenger from the astrophysical source. On the other hand the small cross section of neutrinos makes their detection hard. In the first part of this chapter we will describe the neutrino propagation and oscillations. In the last part we will focus on the detection mechanism.

2.1 Neutrino oscillations

Bruno Pontecorvo [30] hypothesized a difference between the mass eigenstates and the flavor eigenstates for neutrinos. A certain neutrino of flavor l is a superposition of mass eigenstates, and during the propagation, an oscillation between different flavor eigenstates occurs. To formalize the neutrino oscillations predicted by Bruno Pontecorvo, Ziro Maki, Masami Nakagawa and Shoichi Sakata [31] introduced a matrix, known as PMNS matrix or neutrino mixing matrix. Over large distance, the probability of oscillations from a ν_l to a $\nu_{l'}$ in vacuum is given by:

$$P_{ll'} = \sum_{i=1}^{3} |U_{li}^2||U_{il'}^2| \tag{2.1}$$

in which l and l' can be e, μ and τ and U_{li} are the elements of the neutrino mixing matrix[32].
Developing this expression make it possible to explicit the dependence from a phase term:

$$\phi_{ij} = \Delta m_{ij}^2 \frac{L}{4E} \tag{2.2}$$

This term is relevant for the atmospheric neutrinos since for cosmic neutrinos, for a distance greater than some parsec, the phase term become very high. For neutrinos produced at a distance of 100 Mpc, energy $\simeq$ 1 TeV, Δm_{ij}^2 should be $\sim 10^{-16}$ eV^2 so

that the phase term is equal to 1. However we know that the present values of Δm^2 are greater :

$$|\Delta m^2_{21}| \simeq 7.5 \times 10^{-5} eV^2 \qquad (2.3)$$
$$|\Delta m^2_{31}| \simeq 2.5 \times 10^{-3} eV^2 [33]$$

therefore the oscillation pattern disappear.

2.2 High energy neutrino detection

2.2.1 Neutrino interaction

A high energy neutrino interacts with a nucleon N through either charged Charged Current (CC) or neutral Neutral Current (NC) current weak interaction :

$$\nu_l + N \rightarrow l + X \quad (CC)$$
$$\nu_l + N \rightarrow \nu_l + X \quad (NC) \qquad (2.4)$$

The differential cross section for CC interaction [34], at the first order, is:

$$\frac{d^2\sigma_{\nu N}}{dxdy} = \frac{2G_F^2 m_N E_\nu}{\pi} \frac{M_W^4}{(Q^2 + M_W^2)^2} \left[xq\left(x, Q^2\right) + x\left(1-y\right)^2 \overline{q}\left(x, Q^2\right) \right] \qquad (2.5)$$

where G_F is the Fermi coupling constant, m_N is the nucleon mass, M_W is the mass of the W boson, Q is the momentum transferred between the neutrino and the correspondent lepton, $q\left(x, Q^2\right)$ and $\overline{q}\left(x, Q^2\right)$ are the parton function distributions for quarks and antiquarks and x and y the so-called scale variables or Feynman-Bjorken variables given by:

$$x = Q^2 / \left[2m_N \left(E_\nu - E_l\right)\right] \qquad (2.6)$$
$$y = \left(E_\nu - E_l\right) / E_\nu \qquad (2.7)$$

The cross section in Fig. 2.1 exhibits a linear dependence on neutrino energy up to some tens of TeV, then it is slightly attenuated since Q^2 becomes larger of M_W^2. Since few measurements are available for parton distribution functions at small x and high energies, large theoretical uncertainties are present on cross sections.

2.2.2 Cherenkov radiation

Neutrino interactions produce charged particles that are mainly relativistic since they are produced in high energy interactions. A charged particle that travels

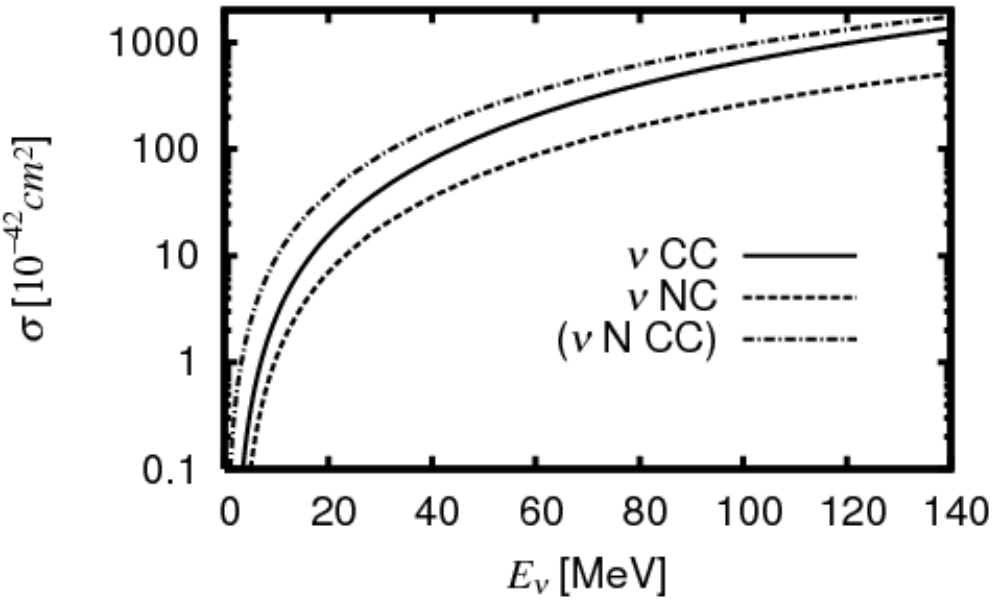

Fig. 2.1: Cross section for charged current (lower solid line), and neutral current (dashed line) neutrino interactions. The dashed-dotted line shows the total neutrino cross section [35].

with a speed greater rather than the speed of light in the medium can produce photons via Cherenkov emission [21]. The charged particle polarizes the molecules along its trajectory, producing an overall dipole moment. When the electrons of the insulator restore themselves to equilibrium after the disruption has passed, a coherent radiation is emitted in a cone with a characteristic angle θ_C given by:

$$\cos\theta_C = \frac{1}{\beta n} \tag{2.8}$$

where n is the refractive index of the medium and β is the particle velocity in c units. θ_C is about 43° for relativistic particles (β=1) in water n=1.364. A charged particles of charge *e* emits dN_γ^2 Cherenkov photons per unit wavelength interval dλ and unit distance traveled dx, by a charged particle of charge e is given by:

$$\frac{dN_\gamma^2}{dx d\lambda} = \frac{2\pi}{\alpha\lambda^2}\left(1 - \frac{1}{(n\beta)^2}\right) \tag{2.9}$$

where λ is the wavelength of the radiation. In the wavelength range between 300 and 600 nm the number of Cherenkov photons emitted is about 3.5×10^4 per meter.

2.2.3 Muon and showers detection

A muon neutrino produces a high energy muon in a CC interaction which direction is highly correlated with the neutrino arrival direction. The angle between the interacting neutrino and the produced muon is [36]

$$\theta_{\nu\mu} \simeq \frac{0.6^\circ}{\sqrt{E_\nu(TeV)}} \tag{2.10}$$

High energy muons travel straight through the detector, producing a clear track signature so they can be well reconstructed. If we assume that the muon is above the Cherenkov emission threshold, the detection of this muon and the reconstruction of its direction can give information on the neutrino. The processes by which a muon can lose energy are:

- Ionisation;
- Pair production;
- Bremsstrahlung;
- Photo-nuclear interactions.

We can parameterize the energy loss per unit path length as:

$$dE_\mu/dx = \alpha\left(E_\mu\right) + \beta\left(E_\mu\right) \cdot E_\mu \tag{2.11}$$

where $\alpha(E_\mu)$ represents the ionization loss and depends on the muon energy and $\beta(E_\mu)$ describes radiation losses (pair production, brehmsstrahlung and photo-nuclear interactions).
At a certain critical energy (E_C) the radiative losses become larger than ionisation losses. This energy depends on the traversed material and is $\simeq$500 GeV in water.
The distance after which a muon, with a given initial energy E_μ, has still an energy greater than the energy that can be detected by the apparatus (E_μ^{thr}) is the effective range R_{eff}. The Fig. 2.2 shows that a muon with an initial energy $E_\mu \simeq$10 TeV can travel $\sim$ 4 km and reach the possible detector with an energy of about 1 TeV.
When a high-energy particle interacts with matter it can produce a shower that is a cascade of secondary particles. The incoming particle in fact interacts and produces multiple new particles with lesser energy; each of these produced particles interacts creating other low-energy particles. There are two basic types of showers. Electromagnetic showers are produced by a particle that interacts primarily or exclusively via the electromagnetic force, usually a photon or electron. Hadronic showers are produced by hadrons (i. e. nucleons and other particles made of quarks),

and proceed mostly via the strong nuclear force. For the neutrino interaction case, a hadronic or electromagnetic shower can be produced respectively when a NC interaction takes place, for any neutrino or antineutrino flavor, or when electron (anti)neutrino CC interaction occurs. Hadronic showers are present in both CC and

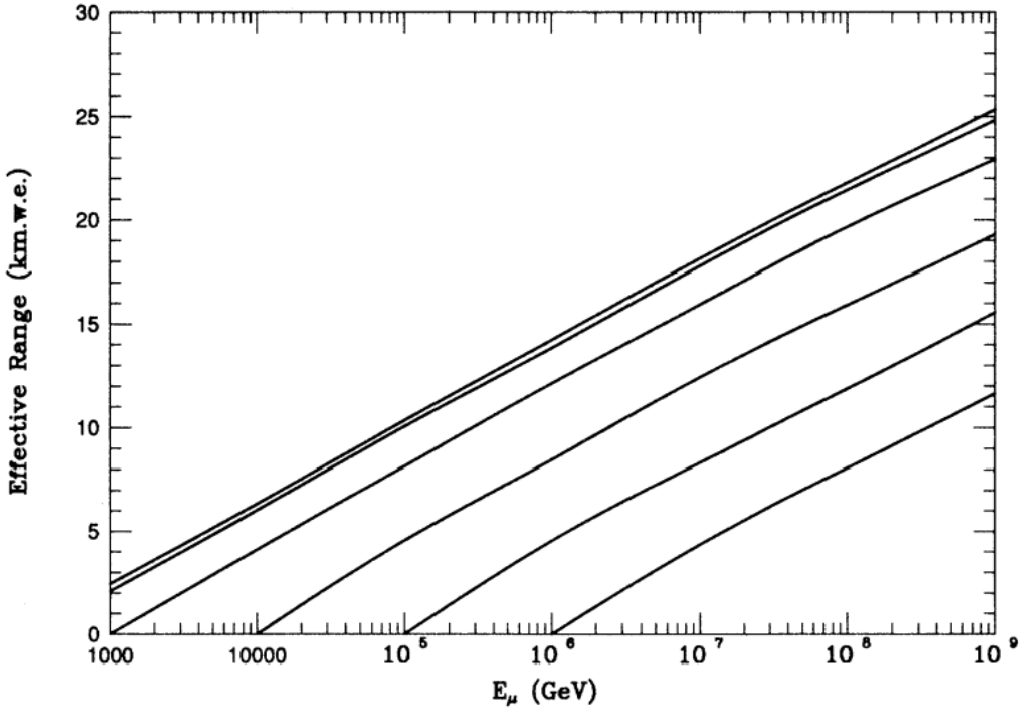

Fig. 2.2: Effective range of muons in unit of water equivalent (w.e.) as a function of their energy. The different lines represent different energy thresholds (from 1 to 10^6 GeV) [37].

NC interactions and represented by the term X in eq. 2.4. When a high energy ν_e interacts via charged current weak interaction, a high energy electron is induced. This electron can create γs through bremsstrahlung and it can produce e^+e^- pairs and generate a further cascade of Electromagnetic (EM) particles. The charged particles in the EM showers can emit Cherenkov light if they are above the threshold. The most important contribution to hadronic showers consists in pions, but also other mesons and baryons are present. Also an electromagnetic component is present in the hadronic shower since the π^0 produced immediately decay into $\gamma\gamma$ starting the process previously described.
While a muon neutrino interaction via CC produces a muon, the shower events are usually characterized by spherical shell of light, centered around the shower maximum. However the shower direction can be reconstructed and in this way go back to the direction of the arrival interacting neutrino.

2.2.4 Tau detection

Tauons have a very short lifetime ($\simeq 2.9 \times 10^{-13}$) and decay producing leptons (electron and electron antineutrino or muon and muon antineutrino) or hadrons. Except for the leptonic decay in muon (BR$\simeq$17.39%), a τ^- decay generates a shower of particles.
If the neutrino interacting energy is high, the tau can produce a visible track before decaying. In this case besides the shower-like events, present both at the interaction vertex (as shown in eq. 2.4) and at the decay point, a track-like event would also be visible since the tau lepton produces Cherenkov light.
If the neutrino energy is less than 1 PeV the two showers are too close to be distinguished while at higher energies and for large detectors the two showers can be separated and the corresponding detected event is called "*double bang event*" (each "bang" correspond to a detected shower). If one of the two showers is outside the detection volume, the event is called "*lollipop event*" since only one shower and a track are visible.

2.2.5 Neutrino telescopes

Neutrino detectors can be aimed at astrophysics observations, operating as a telescope, since they can reconstruct with good angular precision ($< 1°$) the neutrino arrival direction. The intrinsic angle between the direction of the incoming neutrino and the interaction charged products (see eq. 2.10) places an intrinsic limit on the angular resolution.
Since the neutrino interaction cross section is very low as well as the neutrino expected fluxes, very large detectors are needed. The use of large instrumented volumes of natural water was proposed by M. A. Markov in 1960 [38]. The medium chosen, that can be water but also ice, allows the production and the transmission of Cherenkov light produced by relativistic charged particles produced in the interaction but became also itself the target for interaction and a shields from CR air shower background.
The instrumented volume required for the detection of the currently expected neutrino fluxes is of the order of cubic km and in this case a few of these neutrinos will interact within the sensitive volume of the detector in a year of operation. Since the Cherenkov photons produced in the neutrino interactions should be detected, the target has to be instrumented with a large number of highly sensitive light detectors, typically PMT. The density of light detecting devices has to be large enough to have enough signals to reconstruct events. So the number of required PMTs depends on their diameter.

2.2.6 Light propagation in water and ice

The performance of a neutrino telescope, in terms of reconstruction quality depends on the propagation properties of the medium.
The absorption process for example reduces the amplitude of the Cherenkov wavefront and so the light hitting on PMTs. The propagation direction of the Cherenkov photons changes in the scattering processes. Therefore the distribution of the arrival time on PMTs can be modified affecting the reconstruction of the incoming neutrino direction.
The study of the light propagation in a medium must take into account the optical properties of the medium such as the absorption $a(\lambda)$, scattering $b(\lambda)$ and attenuation $c(\lambda)$ coefficients that depends on the light wavelength λ. These quantities are correlated:

$$c(\lambda) = a(\lambda) + b(\lambda) \tag{2.12}$$

The optical proprieties of a medium can also be defined introducing the corresponding absorption, scattering and attenuation length that represents the path after which a beam of initial intensity I_0 is reduced by a factor 1/e because of the corresponding process:

$$L_i(\lambda) = (i(\lambda))^{-1} \quad i = a, b, c \tag{2.13}$$

To describe the scattering process it is necessary that in addition to $L_b(\lambda)$ the angular scattering distribution is known.
Gustav Mie[39] developed an analytical solution of the Maxwell equations for the scattering of electromagnetic radiation by spherical particles which solution is appropriate for modeling light scattering in transparent media. Light traveling in water or ice can encounter the scattering centers (sub-millimeter sized air bubbles and micron sized dust particles) several times before it reaches an optical sensor. The relation between the average cosine of the light field of photons undergoing one or multiple (n) scattering is:

$$\langle cos\theta \rangle_n = \langle cos\theta \rangle^n \tag{2.14}$$

A scattered photon travels on average a distance $L_b(\lambda)$ at an angle defined by $\langle cos\theta \rangle$ before encounter another scattering center. The distance crossed by the photon after n scatters in the incident direction is:

$$L_b^n(\lambda) = L_b(\lambda) \sum_{i=0}^{n} \langle cos\theta \rangle^i \simeq \frac{L_b(\lambda)}{1 - \langle cos\theta \rangle} \tag{2.15}$$

This quantity is largely used in experimental measurements than the quantities $L_b(\lambda)$ and $\langle cos\theta \rangle$ to which it derives.

2.2.7 Under-water telescopes

The project that gave the starts of the construction of underwater telescopes is DUMAND [40] which started in 1976 and lasted until it was canceled by U.S. Department of Energy in 1995. Even if the project did not reach the construction phase all the future experiments took advantage of this experience. Especially from the preliminary studies carried in order to deploy a detection unit in the Pacific Ocean, off the shore of the island of Hawaii, about five kilometers beneath the water surface.
The Baikal Deep Underwater Telescope (BDUNT)[41] is a neutrino telescope posed in the the deep waters ($\sim$ 1300 m) of Lake Baikal in Siberia. Some test detection units have been deployed in the march 1995 and preliminary measurements for high energy neutrinos detection have been completed [42]. A km3 detector is planned to be built in Lake Baikal in the next years [43].
In itâĂŹs 2018 design the telescope, that is the larger underwater neutrino telescope in the World, consists of three clusters of vertical strings with 288 optical modules. A cluster comprises eight vertical strings attached to the lake floor: seven side strings on a radius of 60 m around a central one. Each string carries 36 optical modules, arranged at depths between 735 and 1260 meters (525 m instrumented length). Advantages of building a detector in Lake Baikal are the fact that the thick ice shell present on the lake during the winter time allows easy deployment of instruments in the water and the low optical background expected in fresh water with respect to sea water. On the other hand the water of Lake Baikal is less transparent than sea water or ice, limiting the reconstruction performance.
The Mediterranean Sea provides a favorable environment for building a neutrino telescope since large abyssal planes are present, with depths from 2500 to 4500 m and the measured deep sea current are usually very low.
Three different sites have been proposed for the construction of a large neutrino telescope off shore France, Greece and Italy (Fig. 2.3).
The ANTARES detector [45] will be described in details in the next section. It takes data since 2006 also if it was completed in 2008. It resides at a depth of about 2500m, anchored at the sea bed, 40 km off the coast of Toulon. The ANTARES telescope will be taking data at least up to 2020. The Greek site, off-shore Pylos, Peloponnese, comprises one of the deepest planes in the Mediterranean Sea, with a depth of $\sim$ 4500 m. Some test units have been deployed by the NESTOR Collaboration [46] allowing measurement of the muon flux at a depth greater than 3000 m.
The NEMO telescope was proposed to be deployed in front of the Sicilian coasts, about 100 km off-shore Capo Passero. An intensive R&D activity has been conducted to study the site of Capo Passero and to develop a technology useful for the construction of a new km3 detector.
The KM3NeT [47] detector will be described in details in the next section. It is a

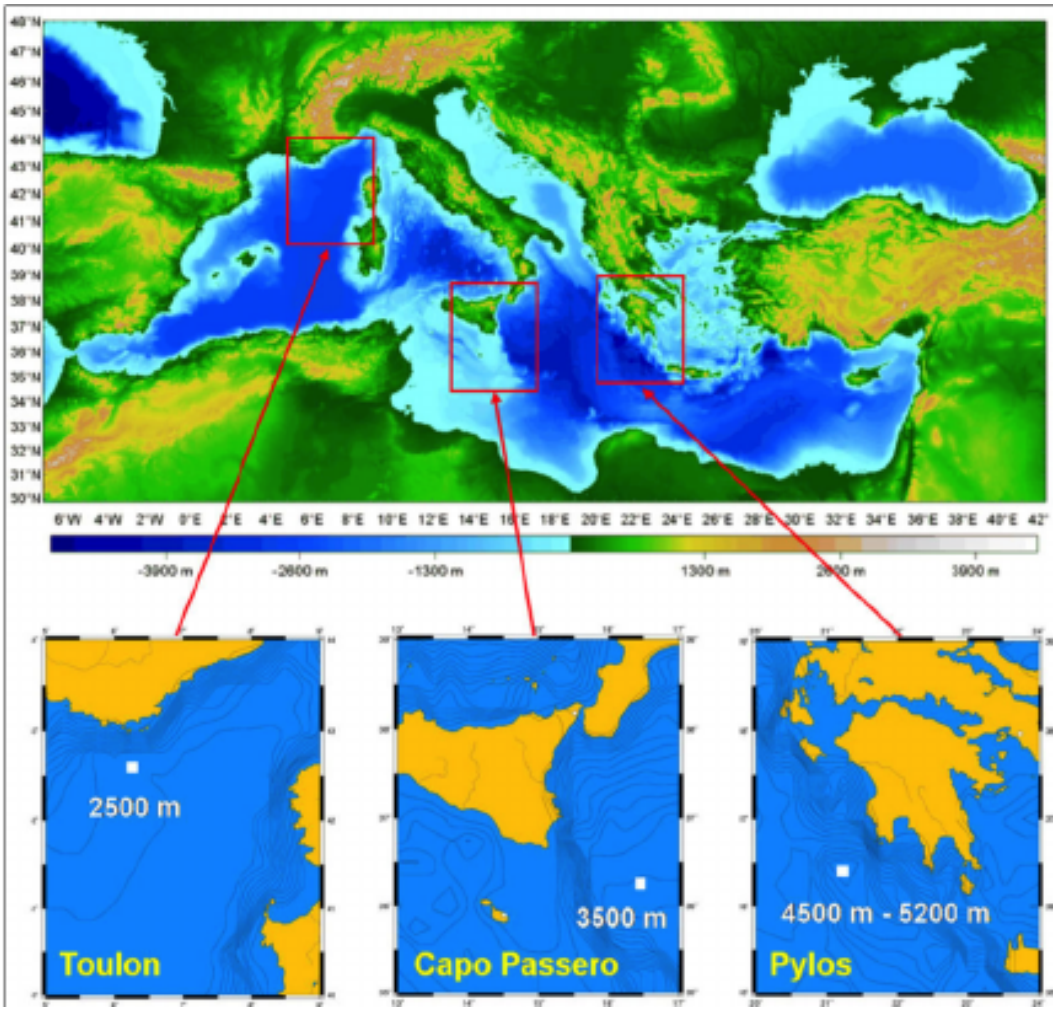

Fig. 2.3: The three Mediterranean sites proposed for the building of neutrino detectors: ANTARES in the France site, NEMO at the Capo Passero site and NESTOR in Pylos [44].

multi-site deep sea infrastructure that will host neutrino telescopes and Earth and sea science experiments.

2.2.8 Under-ice detectors

The first neutrino detector operating in the Antartic ice shell was AMANDA[48]. The Antarctic Muon And Neutrino Detector Array (AMANDA) is a neutrino telescope located beneath the Amundsen-Scott South Pole Station. It started the data taking in 1996 and after nine years of operation became part of the IceCube Neutrino Observatory[49].

IceCube is the largest neutrino detector in the southern hemisphere and comprises 86 strings, each holding 60 DOM made up of 10-inch PMTs in a glass sphere. The distance between DOMs on a string is 17 m and strings are distributed on a hexagonal footprint at an average distance of 125 m. The total instrumented volume is about

one cubic kilometer. The strings deployment is done drilling the ice shell with hot water to put the string in the hole and then letting the ice to freeze again in order to fix the position of DOMs. To simplify the rejection of the background coming from downward-going atmospheric events, ice Cherenkov tanks are placed on top of the detector. The light absorption length in ice is up to three times larger than in water since ice is more transparent so the light can travel a longer distance without being absorbed, enlarging the effective volume of the detector. On the other hand the scattering process is stronger in ice since dust particles and air bubbles are trapped into the ice structure. This makes reconstruction more difficult since most of the detected photons are indirect [50]. In addition the Antarctic ice shell was formed by the superposition of snow layers deposited over an extremely long period of time. The layers present differences in the concentration of dust over time and so the optical properties of ice can have large variation over the almost 3 km of depth. This fact is proved by measurement of light propagation properties with LED flasher in the deep ice (Fig. 2.4). At a depth of about 2000 m there is a rather thick "dust layer" that reduces the light detection efficiency in that region.
Details on the Icecube results will be presented in chapter 6.

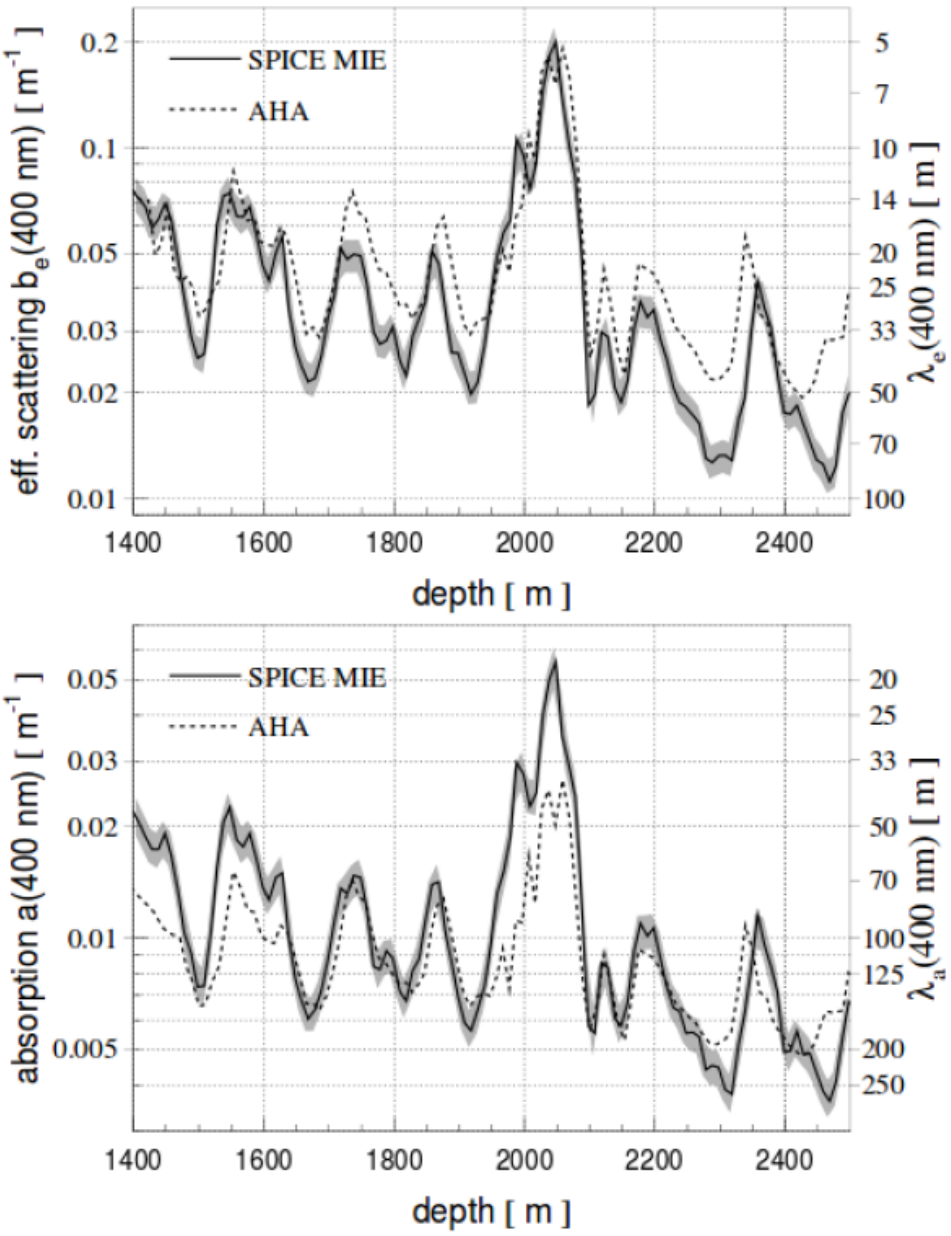

Fig. 2.4: Effective scattering (top) and absorption (bottom) coefficients asa function of the depth in the South Pole ice measured with LED flashers [50]. The results depends on the chosen models for scattering and absorption.

3 The ANTARES and KM3NeT telescopes

3.1 The ANTARES Telescope

ANTARES (Astronomy with a Neutrino Telescope and Abyss environmental RESearch) is actually the largest under-sea neutrino telescope in the Northern hemisphere and the largest under-water neutrino detector [45].
The position in the Mediterranean Sea allows good visibility of the Southern sky and in particular of the Galactic Centre and Galactic Plane, where many neutrino emitting candidates are expected. The ANTARES project started in 1996 with a 4 year R&D phase. Extensive campaigns of measurements of environmental parameters lead to the selection of the detector site located 40 km off the Toulon coast (South France) at a depth of 2400 m[51]. The first detection unit was connected in March 2006 [52] and the detector was completed in May 2008. It is actually the longest operating under-water neutrino telescope.

3.1.1 Detector layout

The ANTARES detector consists of 12 detection lines each one with 25 storeys that include three Optical Modules (OMs) [53]. An optical module is a glass sphere housing 10-inch PMTs [54] and a Local Control Module (LCM) containing the off-shore electronics [55, 56]. The distance between storeys on each line is 14.5 m, and the first storey has a distance of$\sim$100m from the sea-bed and the distance between stroreys in the same line is 14.5 m. The OMs in the storey, mounted on the Optical Module Frame (OMF), are orientated 45 downwards in order to optimize their acceptance to the light from upward-going tracks and to reduce the effect of sedimentation and biofouling.
The length of a line is 450 m and the horizontal distance between neighbouring lines is 60-75 m. The total number of active OMs is 885. The 12 lines are connected to a Junction Box (JB) on the sea-bed, which is then connected to the shore station in La Seyne-sur-Mer with a 42 km long electro-optical cable (Main Electro-Optical Cable (MEOC)). The detector is powered through the MEOC which allows the data collection and the synchronization of the different detector elements through the

distribution of a clock signal.
A schematic view of the detector is reported in Fig. 3.1. The data filtering and triggering operations take place at the shore station and the data are stored at a computer center in Lyon. The 12 ANTARES lines are also provided of instruments for

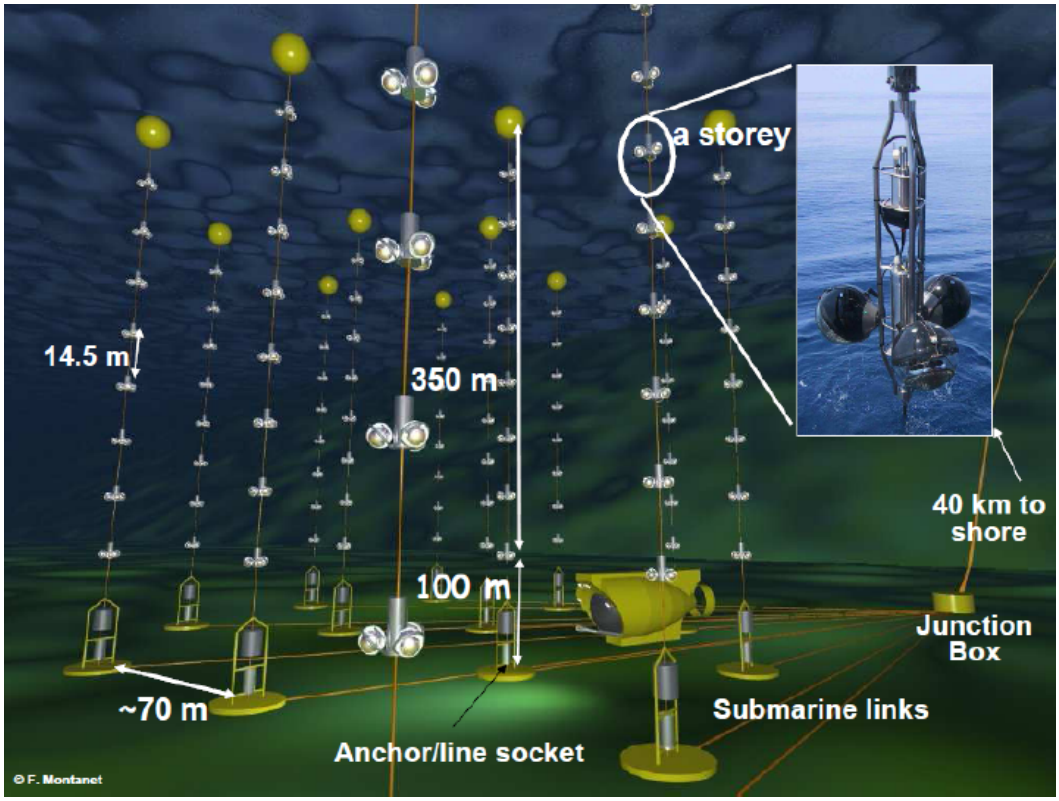

Fig. 3.1: Schematic view of the detector layout.

marine and Earth science researches and some instruments are also located on an additional line devoted to the monitoring of the sea environment. Since ANTARES is taking data continuously since 10 years, it actually provides the longest set of environmental data at such a depth in the Mediterranean Sea.
The lines are anchored to the sea-bed and pulled taught by the buoyancy of the individual OMs and a top buoy. Due to the flexible nature of these lines, they can be a displaced by several meters from the vertical due to relatively small water current velocity of 5 cm/s. For this reason a real time positioning of each OM is needed. This is achieved through two independent systems: an acoustic positioning system and tiltmeters-compasses on each storey. A global fit performed using information from both of these systems allows the reconstruction of the shape of each line and the calculation of the relative positions of each individual OM using the known geometry of each storey.
To achieve the required angular resolution, the recorded PMTs signal must have timing resolution of the order of 1 ns and for this aim the master clock system is used. It is based on-shore and delivers a common reference time to all the off-shore electronics in the LCMs . The master clock system delivers a timestamp, derived from

GPS time, via an optical fiber network from the shore station to the junction box and then to each line base and to each LCM. This system is self calibrating and measures continuously the time path from shore to the LCM by echoing signals received in the LCM back to the shore station.

3.1.2 Site characteristics

The measurement of the environmental parameters and the optical water properties at the detector site has been performed in details during the R&D phase of the experiment showing the results explained in the following.

Water properties

Water properties in the ANTARES site have been studied analyzing light distributions of photons emitted from a pulsed isotropic light source and detected by a PMT at different distances from the source and for two wavelengths [55]. This approach is not sufficient to fully determine the differential cross section of the photon scattering process, the absorption length can be measured and a parametrization which reproduces the main features of the scattering process can be obtained. The system for this measurement was mounted on an autonomous [57] mooring line anchored by a sinker. The line remained vertical because of the rotation provided by syntactic buoys. The measuring system consisted of 17-inch pressure resistant glass spheres mounted on two triangular aluminum frames. A set of three mechanical cables attached to the vertices of the two frames defined their separation distance. The bottom frame supported a light source sphere which contained a set of LEDs with their pulsers. The top frame supported a detector sphere facing the light source sphere and a service sphere. The detector sphere housed a 1-inch photomultiplier tube and the front-end electronics. Such a small PMT is ideal for this measurement since its acquisition is only slightly influenced by the optical background in water and the transit time spread is extremely limited, providing a proper measurement of the pulse time. Except for the PMT window, the internal surface of the detector sphere was blackened to absorb photons outside the PMT detection solid angle.
In order to obtain an isotropic light source for two wavelengths, 6 pairs of LEDs were mounted on the centers of the faces of a cubic frame 3 cm on a side which also supported the LED pulser boards. The cube was installed at the center of a 17-inch glass sphere whose external surface had been sand blasted to provide extra diffusion and to remove surface ripples or roughness which can destroy the homogeneity of the emitted light flux. The measured values for the effective attenuation length and

the absorption length at the ANTARES site are reported in Fig. 3.2. The measured value of the effective attenuation length for a wavelength $\lambda = 466$ nm is

$$Lc(\lambda = 466nm) = 41 \pm 1(stat) \pm 1(syst)m \tag{3.1}$$

The measurement had been repeated during the course of one year to understand

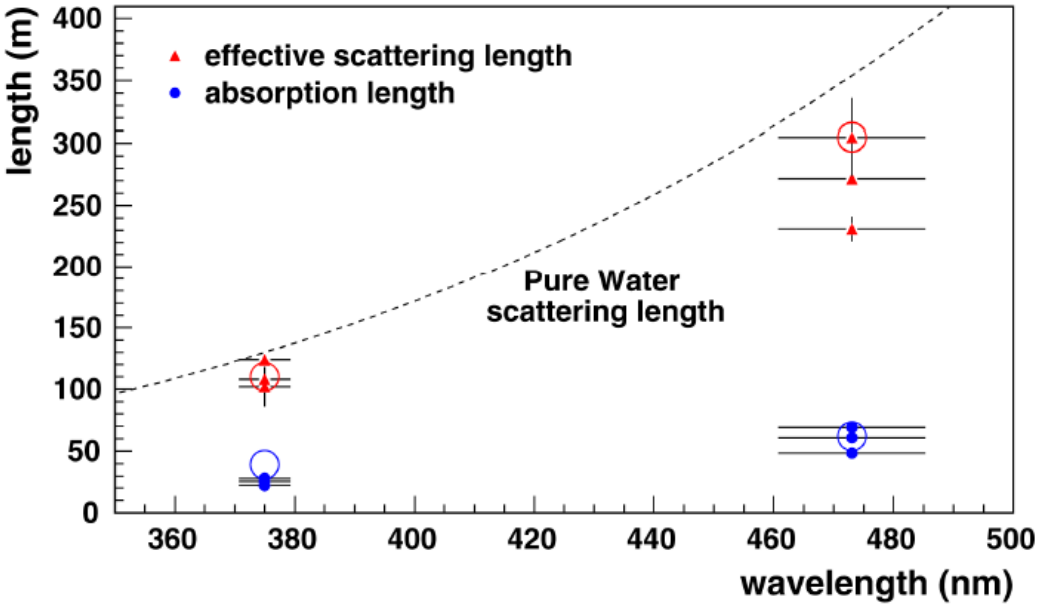

Fig. 3.2: Water properties at the ANTARES site [55]. The red and blue dots represent the measured effective scattering and absorption length of light in water respectively at two different wavelengths over different periods of time. The black dashed line shows, for comparison, the effective scattering length of light in pure water.

the time variability of water properties at the experimental site. Small differences were found at different times, compatible with the accuracy of the measurement.

Biofouling and sedimentation

The detector elements are exposed to sedimentation of particles and adherence of bacteria (biofouling) which can reduce the light transmission through the glass sphere of the OMs. These effects on the ANTARES optical modules have been studied in details in [58] using an experimental setup consisting of two resistant glass spheres similar to those used for the OMs. One of them was equipped with five photo-detectors glued to the inner surface of the sphere at different inclinations illuminated by two blue light LEDs contained in the second sphere. The measurements have been performed during immersions of several months and an extrapolation has been used to predict the results for longer periods of time. The trend of light transmission as a function of immersion is shown in Fig. 3.3. As expected the fouling is lower for larger zenith angles and the loss of transparency in the equatorial region of the

OM is only of about 2.7% in eight months of operation of the test system and then seems to saturate. Since the ANTARES PMTs have a zenith angle of 135° pointing

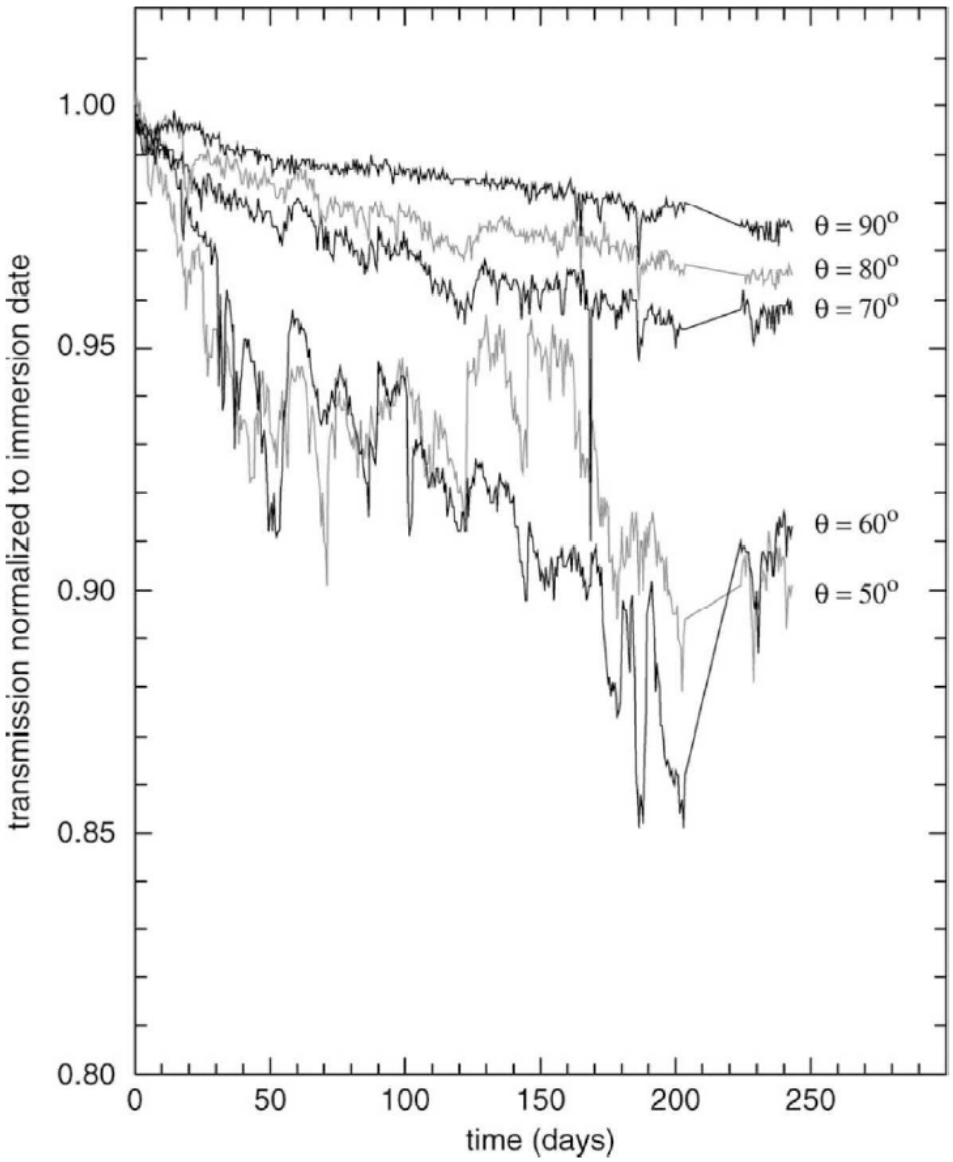

Fig. 3.3: PMT light transmission as a function of time spent under-water and of the inclination with respect to the horizontal [58].

45° downward, the biofouling and the sedimentation should not represent a major problem for the experiment.

3.1.3 Optical background

The optical background on PMTs in sea water has two main contributions:

- bioluminescence;

- decays of radioactive elements naturally present water.

Among the radioactive decays, the dominant process is the decay of ^{40}K decay through the channels:

- $^{40}K \longrightarrow {}^{40}Ca + e^- + \overline{\nu}_e$;
- $^{40}K + e^- \longrightarrow {}^{40}Ar + \nu_e + \gamma$.

Electrons produced in the first of channel have often an energy above the threshold for Cherenkov light production and the γ-rays from the second channel, having an energy of 1.46 MeV, through Compton scattering can induce electrons above the Cherenkov threshold. The intensity of ^{40}K optical background is related to its concentration and thus to salinity of sea water that is almost constant all over the Mediterranean Sea. The mean single rates from ^{40}K decays are of ~ 50 kHz on a 10-inch PMT [59].
The bioluminescence is due, in deep sea, to glowing bacteria and light flashes produced by marine animals and can create an optical background of several orders of magnitude more intense than the ^{40}K decay light. While the optical noise due to radioactive decays of salts in water produce a more or less constant baseline, the passage of light emitting organisms can induce bursts in the counting rates of PMTs. The bioluminescence emission have a seasonal trend and reaches its maximum during spring when MHz single rates on PMTs can be detected. During these period the detector is switched-off to avoid data acquisition problems and excessive ageing of PMTs.

3.1.4 Data acquisition

The Data Acquisition (DAQ) system of ANTARES is extensively described in [55]. A full-custom Analogue Ring Sampler (ARS) has been developed to perform the complex front-end operations [55]. This chip samples the PMT signal continuously at a tunable frequency up to 1GHz and holds the analogue information on 128 switched capacitors when a threshold level is crossed. The information is then digitized, in response to a trigger signal, by means of two integrated dual 8-bit Analog-to-Digital Converter (ADC). Optionally the dynamic range may be increased by sampling the signal from the last dynode. A 20MHz reference clock is used for time stamping the signals. A Time-to-Voltage Converter (TVC) device is used for high-resolution time measurements between clock pulses. The ARS chip can also discriminate between simple pulses due to conversion of Single PhotoElectron (SPE) from more complex waveforms. The two classes can indeed be identified on the basis of the amplitude of the signal, the time above threshold and the occurrence of multiple peaks within

a time gate. Only the charge and time information is recorded for SPE events, while a full waveform analysis is performed in all other cases. The ARS chips are arranged on a motherboard to serve the optical modules. Two ARS chips, in a "$token\ ring$" configuration, perform the digitization of the charge and time information of a single PMT. A third chip on each board is used for triggering purposes. The settings of each individual chip can be remotely configured from the shore.

The counting rates on each OM exhibit, as described in the previous section, a baseline,normally between 50 to 80 kHz, dominated by optical background due to sea water ^{40}K decay and bioluminescence coming from bacteria and bursts of a few seconds duration probably produced by bioluminescent emission of macro-organisms close to the OM itself. A high rate veto, often set to 250 kHz single rate on each PMT, is used as an online safeguard against bioluminescence bursts. The OMs deliver their data in real time and can be remotely controlled through a Gb Ethernet network. Every storey is equipped with a LCM hosting the electronic boards for the OM signal processing, the instrument readout, the acoustic positioning, the power system and the data transmission. Every five storeys the Master Local Control Module contains an Ethernet switch board for the multiplexing of the DAQ channels from the other storeys. At the bottom of each line, the Bottom String Socket is equipped with a String Control Module which contains local readout and DAQ electronics, as well as the power system for the whole line. Both the Master Local Control Modules (MLCMs)s and the String Control Modules include a Dense Wavelength Division Multiplexing (DWDM) system. The DWDM is used in data transmission to merge several 1Gb/s Ethernet channels on the same pair of optical fibers, using different laser wavelengths. The lines are linked to the junction box by electro-optical cables which were connected using an unmanned submarine vehicle. A standard deep-sea telecommunication cable links the junction box with a shore station where the data are filtered and recorded. All OMs are continuously read out and digitized information (hits) is sent to shore. A hit is a digitized PMT signal above the ARS threshold, set at about 1/3 of the single photoelectron level (Level 0 hits, L0). On-shore, a dedicated computer farm performs a global selection of hits looking for interesting physics events (DataFilter). The on-shore handling of all raw data is the main challenge of the ANTARES DAQ system, because of the high background rates. The data output rate can be between 0.3 GB/s to 1 GB/s, depending on the background level and on the number of active strings. For triggering purpose, L1 hits, a subset of L0 hits that have to fulfill some conditions, are used. These hits corresponds either to coincidences of L0 on the same OM triplet of a storey within 20 ns or to a single high amplitude L0 (typically >3 p.e.).

The DataFilter processes all data online and looks for physics events by searching for a set of correlated L1 hits on the full detector in a $\sim 4\ \mu$s window. In case an event is found, all L0 hits of the full detector during the time window are written on disk, otherwise hits are thrown away. The trigger rate is between 1 to 10 Hz, depending on the number of strings in data acquisition, on the environmental conditions and

on the active trigger algorithms. Most of the triggered events are due to atmospheric muons, successively reconstructed by track-finding algorithms.
If ANTARES receives external alerts, such as from GRB observatories [55], all the activity of the detector is recorded for a few minutes. Some untriggered data runs are also collected to monitor the relative PMT efficiencies and check the timing within a storey, using the ^{40}K activity.

3.2 The KM3NeT Telescope

KM3NeT [47] is the next generation km^3 neutrino telescope to be installed in the Mediterranean Sea, a convenient location to look for high-energy neutrino sources in the central part of the Galaxy. In the early 2013 the KM3NeT collaboration has started to engineer and implement the KM3NeT technology in KM3NeT-phase1. The design and construction of KM3NeT is pursued by an international collaboration that comprises the institutes already involved in the ANTARES , NESTOR and NEMO pilot projects. The detector will consist of a three-dimensional array of pressure-resistant spheres, called DOMs, each equipped with 31 photomultipliers with 3-inch photocatode diameter. The DOMs will be arranged in detection units, vertical strings anchored on the sea floor, each equipped with 18 DOMs. In each detection unit, the data and power is connected via the anchor to a deep-sea cable network containing some junction boxes and electro-optical cables through which the OM data are transferred to shore. It also provides power and slow-control communication to the detector.
A shore station hosts both the power feeding system and the computing farm required for collecting the data, applying online filter algorithms and transmitting the data to mass storage devices. A complete description of the detector can be found in [47].

3.2.1 Optical Modules and photomultipliers

The active part of a neutrino telescope is the optical module. KM3NeT has chosen a multi-PMT optical modules, built by means of a 31 photomultipliers of small-size PMTs housed in a pressure-resistant glass sphere [60, 61]. This approach offers some advantages compared to more traditional designs based on large-area PMTs, such as:

- maximization of the total photocathode area in a single sphere
- less sensitivity to the Earths magnetic field of small photomultipliers

- simpler distinction of single-photon to multi-photon hits since two-photon hits can be unambiguously recognized if the two photons hit separate tubes

- small integrated anode charge and are therefore less ageing effect.

The DOM of KM3NeT is made of 31 3-inch PMTs housed in a sphere of 17-inch diameter (see Fig. 3.4). The PMTs are arranged in 5 rings of tubes with zenith angles

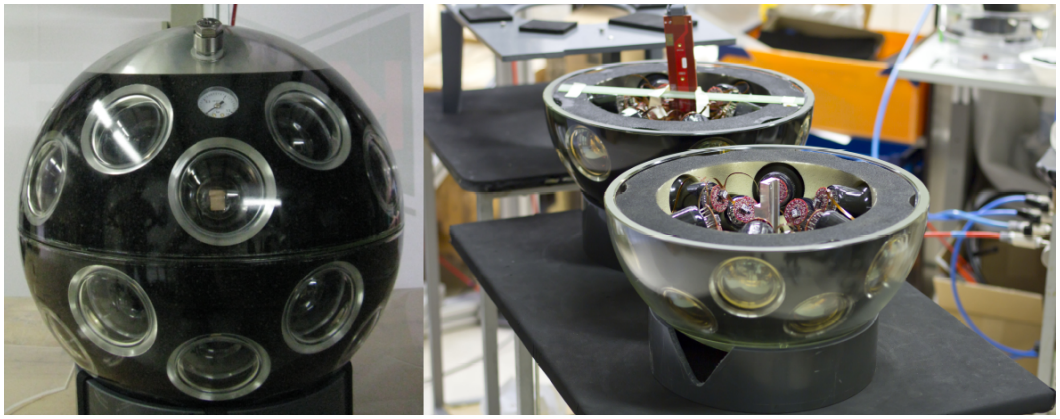

Fig. 3.4: The DOM of KM3NeT. In the right picture the assembly of a prototype is shown.

of $50°$, $65°$,$115°$,$130°$, and $147°$. In each ring the PMTs are spaced at $60°$ in azimuth and the rings are staggered by $30°$.
The PMTs have a standard bialkali photo-cathode with a maximal quantum efficiency of about 30% and a FWHM of transition time spread less than 5 ns. Each PMT is surrounded by an expansion cone that is designed to enlarge its sensitive photocathode area collecting photons that would otherwise miss the photocathode (see Fig. 3.5). The collecting efficiency increase by 30% on average for angles of incidence from $-50°$ to $+45°$, with a maximum of 35% for perpendicular incidence [62].
Inside the sphere an active base, is attached to each PMT allowing to control from the shore the HV and threshold settings for each tube. The concept of "All-data-to-shore" is adopted. In particular, for each digitized hit, the threshold crossing time and the time-over-threshold are sent to shore. Each optical module requires about 10 W of electrical power and has 1 Gb/s readout bandwidth.
All DOMs are synchronized to the sub-nanosecond level by means of a clock signal broadcast from shore. The time offsets of the individual PMTs is calibrated onshore before deployment, and is continuously monitored in situ by means of a system of light beacons meant to illuminate groups of DOMs at known times; this system comprises laser beacons located on the sea bottom and LED pulsers located inside the DOMs.
In each DOM some instruments are mounted comprising a piezo-sensor for acoustic positioning purposes, a tiltmeter and a compass, as well as sensors of the temperature and humidity inside the DOM for monitoring purposes. The internal structure of the DOM has been carefully designed to efficiently avoid heat from the electronics

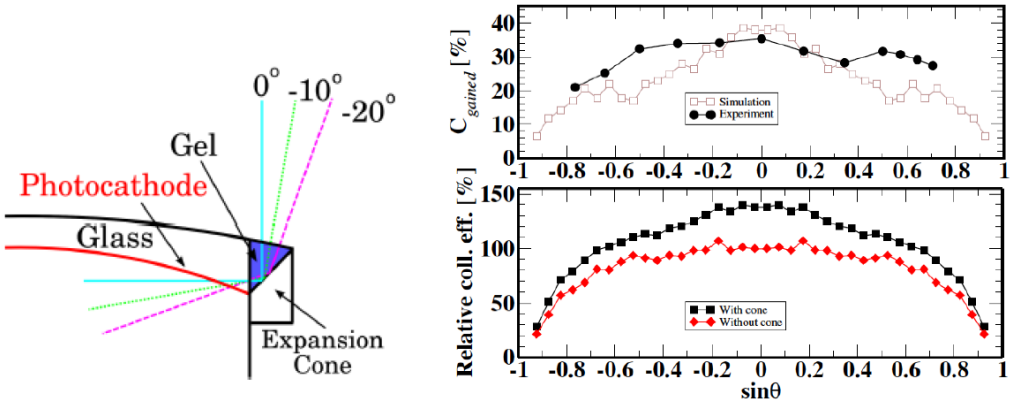

Fig. 3.5: Left: Depiction of the light collection by an expansion cone. Right upper: gained collection efficiency as a function of the $sin\theta$, being θ the angle of incidence. Right lower: collection efficiency as a a function of $sin\theta$ with and without expansion cone. [62]

using a mushroom-shaped aluminum structure that transfer it to the sea via the glass sphere.

A breakdown structure of the DOM is shown in Fig 3.6.

A prototype DOM has been mounted on the instrumentation line of ANTARES and has been installed in the ANTARES detector site on April 2013 (see Fig. 3.7).

Since the DOM contains many PMTs it is possible to look for coincidences of hits within the single optical module. The sum of hit rates of all PMTs in the DOM in 100 ms timeframe bins are shown in the right panel of Fig. 3.7 together with the rate for twofold and threefold coincidences as a function of time. The occurrence of a hit in two (or three) PMT within a time window of 20 ns is referred as two (three)-fold coincidence but to provide adequate statistics the rate of three-fold coincidences is averaged over 300 ms. DOM is also capable of detecting multiple photons from a single ^{40}K decay as shown in Fig. 3.8 where the time difference ΔT between hits in separate PMTs for increasing angular separation of the phototubes. The clear Gaussian peak centered at $\Delta T = 0$ indicates the detection of two photons from the same ^{40}K decay.

The analysis of the PMT coincidence rates also shows that a single DOM can, by itself, unambiguously identify atmospheric muons as demonstrated in Fig. 3.9 where the event rate is shown as a function of the coincidence level. The data are compared with a simulation including both the ^{40}K background and the contribution from flux of downgoing atmospheric muons at the depth of the detector. The rates decrease rapidly as a function of the coincidence level as every level increase leads to an extra factor of $Area_{PMT}/(4\pi r^2)$ in acceptance and so to a rapidly decreasing volume of water in which the DOM is sensitive to the ^{40}K decays. For coincidence level lower than 6, the measured event rate is in good agreement with the event rate given by the optical background, except for the single rate, which is very sensitive to the attenuation and scattering length in the water and also has a contribution from

bioluminescence is underestimated by the simulation. For a coincidence level higher than 6 the signals from atmospheric muons dominate with an excellent agreement between data and the simulation.

3.2.2 Detection Units

The optical modules are kept suspended in the sea by vertical structures, which are anchored to the seafloor and kept taught by buoyancy at their top. These structures together with their optical modules are referred as DU or strings. The DU is kept together by two dyneema ropes, while an electro-optical backbone provides connections for each DOM on two conductors for power and two optical fibers for communications with shore. A new technique has been developed to deploy strings. Each string is first wound on a launcher vehicle, which has the shape of a sphere with 2 m diameter as shown in Fig. 3.10. The launcher vehicle is lowered to the seabed from a surface vessel. Once the launcher vehicle has reached the seabed, the buoy is released, the string unfurls and rises to its full height, as sketched in Fig. 3.10. The launcher vehicle is then recovered for subsequent deployments. On May 2014, a prototype string comprising three active DOMs was successfully deployed and connected to the KM3NeT-Italy site and operated for more than one year [64].

3.2.3 The building block

The infrastructure will consist of three so-called building blocks. A building block comprises 115 detector units (strings). Each building block thus constitutes a 3-dimensional array of photo-sensors that can be used to detect the Cherenkov light produced by relativistic particles emerging from neutrino interactions. Two building blocks will be sufficient to fully explore the IceCube signal with comparable instrumented volume but using different methodology, improved resolution and complementary field of view, including the Galactic plane [47]. The KM3NeT project will include the building of these two building blocks are referred to as ARCA and another building block, densely configured to precisely measure atmospheric neutrino oscillations and referred to as Oscillation Research with Cosmics in the Abyss (ORCA). For KM3NeT/ARCA, each string is about 700 m in height, with DOMs spaced 36 m apart in the vertical direction, starting about 80 m from the sea floor. For KM3NeT/ORCA, each string is 200 m in height with DOMs spaced 9 m apart in the vertical direction, starting about 40 m from the sea floor. ARCA will be realized at the Capo Passero site and ORCA at the Toulon site. Due to KM3NeT's flexible design, the technical implementation of ARCA and ORCA is almost identical. The deep-sea sites are linked to shore with a network of cables for electrical power and high-bandwidth data communication. On site, shore stations are equipped to provide

power, computing and a high-bandwidth internet connection to the data repositories. The readout of the detectors is based on the "All-data-to-shore" concept, pioneered in ANTARES.

3.2.4 Fibre-optic data transmission system

The KM3NeT fibre-optic data transmission system [47] performs the following functions:

- Transfers all the data to shore: The bandwidth per DOM is 1 Gb/s. The observed singles rate is dominated by ^{40}K and is typically 6-8 kHz per PMT [47] or 190-250 kHz per DOM, which amounts to 9-12 Mb/s per DOM. Additional contributions from bioluminescence can be accommodated up to levels of a factor of 10 compared to^{40}K;

- Provide timing synchronization: Relative time offsets between any pair of DOMs are stable within 1 ns;

- Provide individual control for each DOM: Setting the HV of a PMT, turn off/on a single PMT, turn on/off nano-beacon, update soft- and firmware;

- Provide individual control for each base of a string: Turn string power on/off, control optical amplifiers, monitor AC/DC converter;

- Provide slow control for the junction boxes.

The slow-control system is implemented via a broadcast mechanism (same as that of the clock), in which control information for all strings is sent on a single common wavelength. If it is a message for just a single string or DOM it is ignored by all the others. The communication from offshore exploit a DWDM technique. The return signals for the slow control are transmitted on 34 wavelengths via the slow-control fiber(s). The data return path is based on a 50 GHz spacing system with a 72 wavelengths uplink. Each DOMs of 4 strings produces a unique wavelength that is combined on one fiber. Erbium-Doped Fiber Amplifier (EDFA) optical amplifiers are introduced onshore and at the base of a string to maintain the optical margins above 10 dB.

3.2.5 Data acquisition

The readout [64] of the KM3NeT detector is based on the "All-data-to-shore" concept in which all analogue signals from the PMTs that pass a preset threshold (typically 0.3 photo-electrons) are digitized and all digital data are sent to shore where they are processed in real time. The physics events are filtered from the background using designated software. To maintain all available information for the offline analyses, each event will contain a snapshot of all the data in the detector during the event. Different filters can be applied to the data simultaneously.
The optical data contain the time of the leading edge and the time over threshold of every analogue pulse, commonly referred to as a hit. Each hit corresponds to 6 Bytes of data (1 B for PMT address, 4 B for time and 1 B for time over threshold). The least significant bit of the time information corresponds to 1 ns. The total data rate for a single building block amounts to about 25 Gb/s. In addition to physics data, summary data containing the singles rates of all PMTs in the detector are stored with a sampling frequency of 10 Hz. This information is used in the simulations and the reconstruction to take into account the actual status and optical background conditions of the detector.
In parallel to the optical data, the data from the acoustics positioning system are processed and represents a data volume of about one third of that of the optical data.

Event trigger

For the detection of muons and showers, the time-position correlations that are used to filter the data follow from causality. The scattering of light in deep-sea water is such that the time window can be very small, a typical value is $\Delta T = 10$ ns. The estimated L1 rate per optical module is then about 1000 Hz, of which about 600 Hz is due to genuine coincidences from ^{40}K. The remaining part arises from random coincidences which can be reduced by a factor of two by making use of the known orientations of the PMTs. This is referred to as the level-two filter (L2). Separate trigger algorithms operate in parallel on this data, each optimized for a different event topology. A general solution to trigger on a muon track event consists of a scan of the sky combined with a directional filter [66]. In the directional filter, the direction of the muon is assumed. For each direction, an intersection of a cylinder with the 3D array of optical modules can be considered. The diameter of this cylinder (i.e. road width) corresponds to the maximal distance traveled by the light. It can safely be set to a few times the absorption length without a significant loss of the signal. The number of PMTs to be considered is then reduced by a factor of 100 or more, depending on the assumed direction. Furthermore, the time window that

follows from causality is reduced by a similar factor 2. This improves the Signal-to-Noise ratio (S/N) of an L1 hit by a factor of (at least) 10^4 compared to the general causality relation. With a requirement of five (or more) L1 hits, this filter shows a very small contribution of random coincidences. The field of view of the directional filter is about 10 degrees. So, a set of 200 directions is sufficient to cover the full sky. By design, this trigger can be applied to any detector configuration. Furthermore, the minimum number of L1 hits to trigger an event can be lowered for a limited number of directions. A set of astrophysical sources can thus be tracked continuously with higher detection efficiency for each source. For shower events, triggering is simpler, since the maximal 3D-distance between PMTs can be applied without consideration of the direction of the shower.

A maximum distance traveled by the light can be assumed, limiting the maximum distance between hit PMTs. This reduces the number of PMTs to be considered and the time window that follows from causality.

Hence, an improvement of the S/N ratio compared to the general causality relation can be obtained.

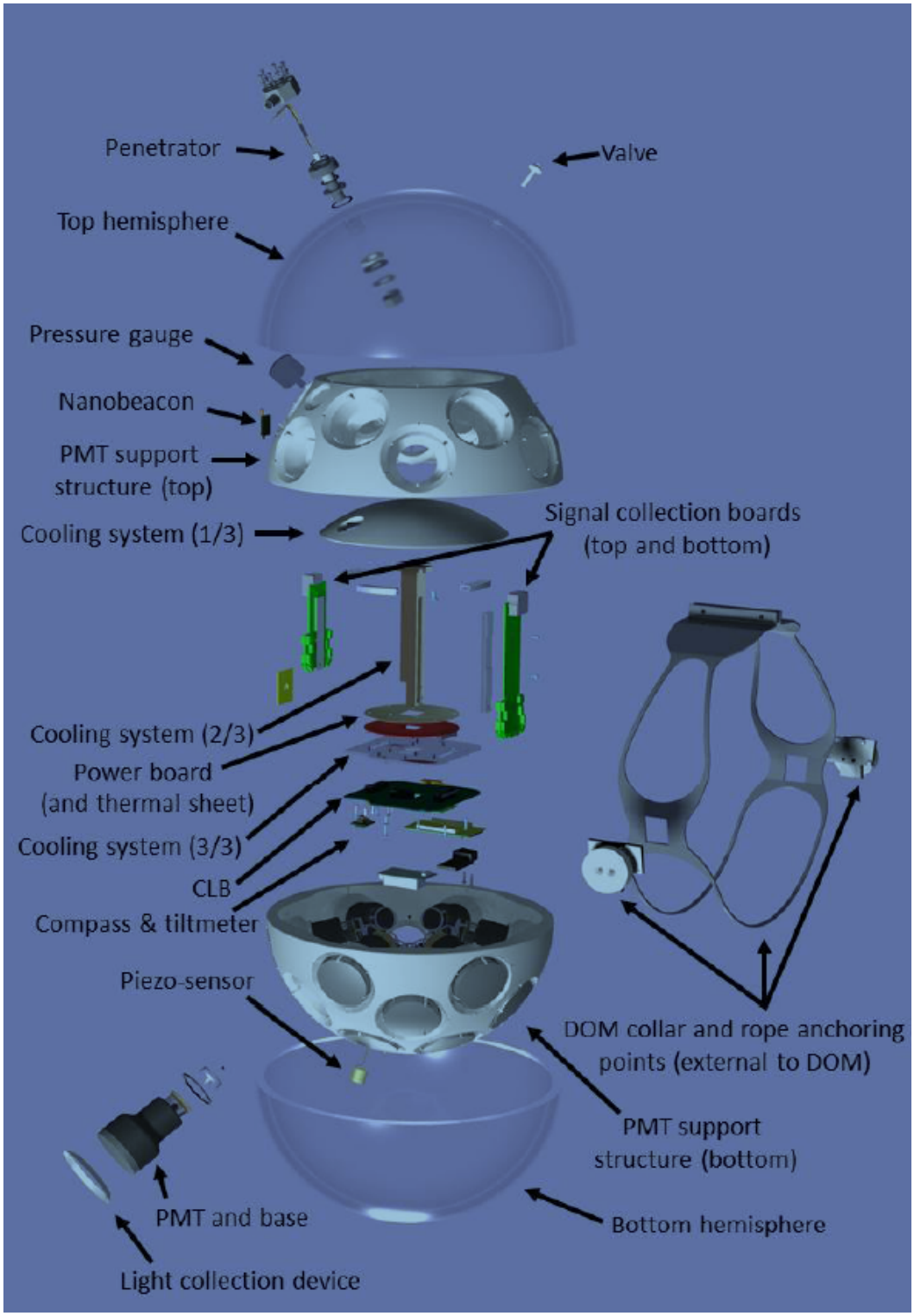

Fig. 3.6: Internal structure of the KM3NeT DOM [63].

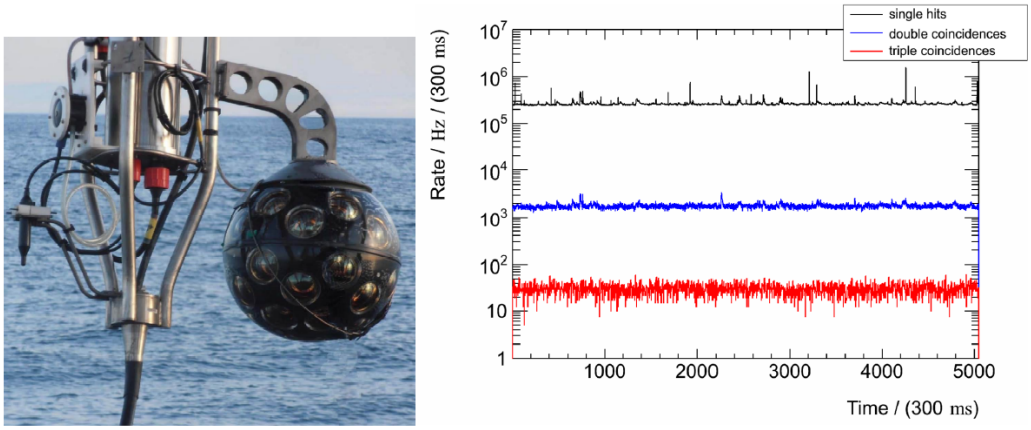

Fig. 3.7: Left: Prototype DOM installed on the instrumentation line of ANTARES during deployment. Right: Rates of events as a function of the time measured in 100 ms bins. The top trace is for single hits while the lower traces are for two- and threefold coincidences within a 20 ns window [64].

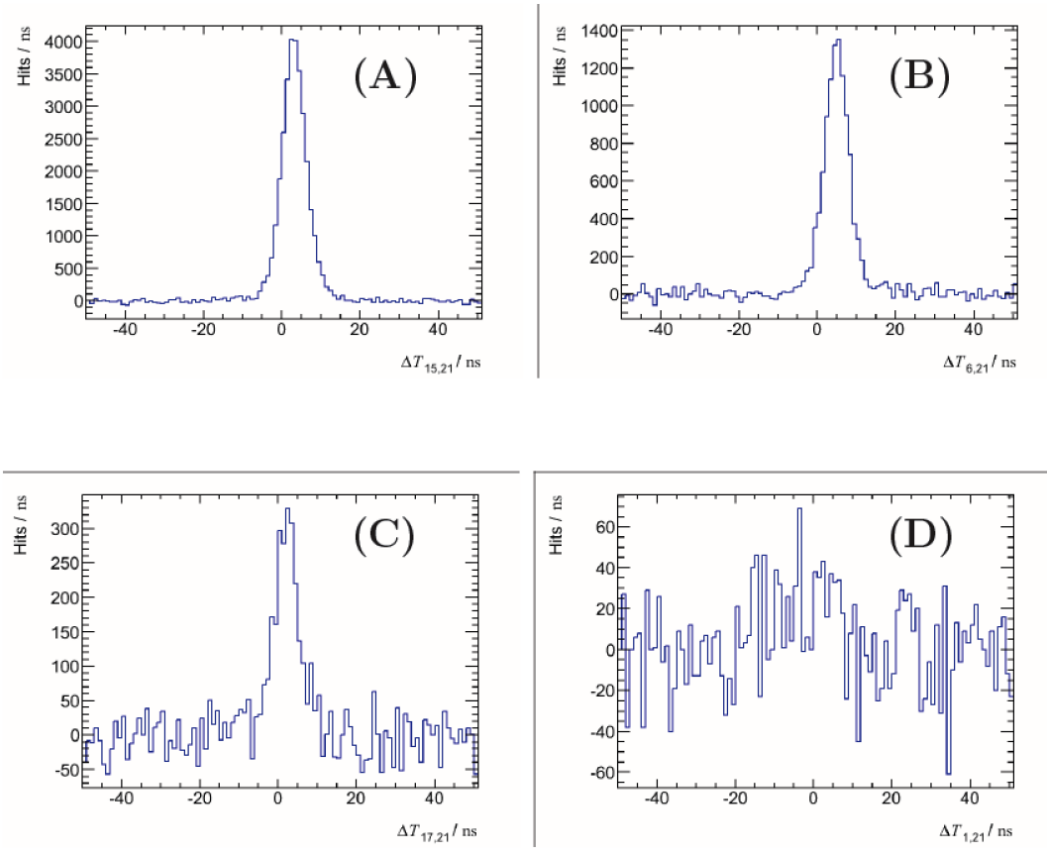

Fig. 3.8: Time difference distribution between two PMTs of the DOM, with an angular separation of 33° (A), 65° (B), 120° (C) and 165° (D) [65].

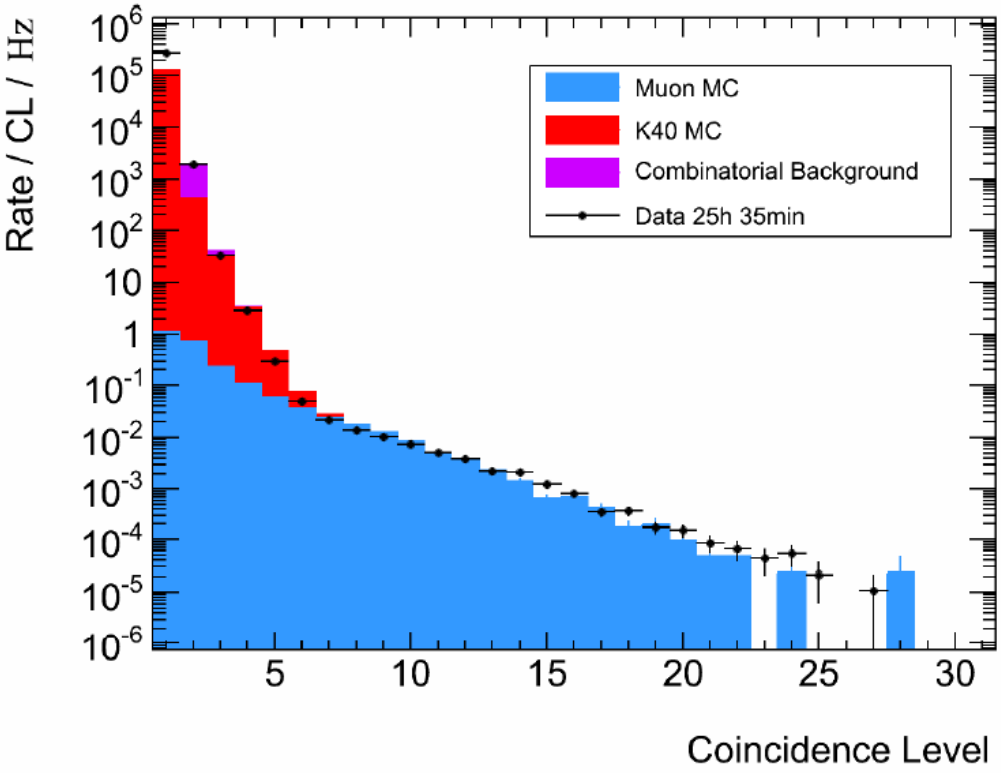

Fig. 3.9: The rate of events as a function of the coincidence level (number of PMT with signal in a 20 ns time window). Black dots correspond to data while colored histograms represent simulations (muons in blue, ^{40}K in red and accidental coincidences in purple) [65].

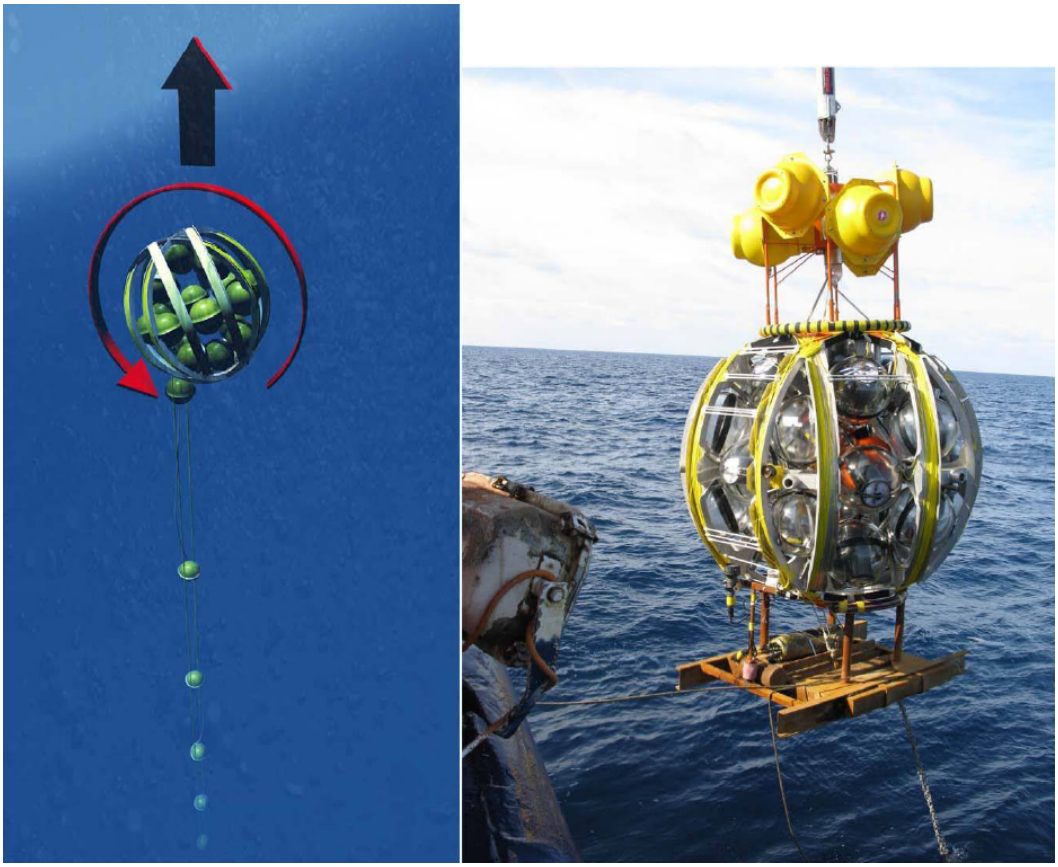

Fig. 3.10: Left: unfurling of a KM3NeT DU. Right: Mechanical model of a DU, arranged on the launcher vehicle, being deployed during a test campaign [47].

4 Software Simulation Tools

In this chapter we will describe the Montecarlo simulation used by the and KM3NeT Collaboration underlining our contribution in adding in the generation code the "propagation of secondary neutrinos". Monte Carlo simulation tools are useful for the interpretation of the data recorded by a detector and for understanding the effect of detector systematic. Montecarlo simulations have an important role during the design phase of the experiments since are the only way to properly evaluate their physics potential.

The software used in this thesis has been developed by the ANTARES Collaboration [67] for the ANTARES telescope and adapted to KM3NeT. The code provides a simulation of the incident neutrinos, including their interaction in the medium and the propagation of the resulting secondary particles, the light generation and propagation in water and the detector response. Since this tool is used in this work for ARCA (Astroparticle Research with Cosmics in the Abyss) simulations, the depth and the optical water properties measured at the Sicilian Capo Passero site have been used [68].

Background light due to the presence of ^{40}K in salt water and bioluminescence has been simulated adding an uncorrelated hit rate of 5 kHz per PMT and a time-correlated hit rate of 500 Hz per DOM (two coincident hits in different PMTs inside the same DOM) due to the genuine coincidences from Potassium decays.

The codes are written in fortran and C++ languages and the output of each code is an based text file. The output file can be the input of the next step in the chain or can be converted in a ROOT-file for the analysis. A scheme of the simulation chain is shown in Fig. 4.1. The code GENDET is used for the generation of the detector geometry. GENHEN generates atmospheric or signal neutrinos while atmospheric muons are generated with MUPAGE. The KM3 and KM3SIM codes simulate the secondary particles generated at the interaction vertex and the consequent generation of hits due to Cherenkov photons The noise hits due to ^{40}K uncorrelated and bioluminescent background are added using JTE that also simulates the combined response of PMTs to photon hits, and apply a trigger. JGandalf and JEnergy are then used to perform the muon track reconstruction. In the following we will describe in details GENHEN and the results that were obtained during this thesis adding the complete "ν_τ regeneration" effect.

4.1 Neutrino event generation: GENHEN

The GENHEN code is used to generateneutrino-induced secondary particles at the detector. This code includes the simulation of incident neutrinos, their interactions in the medium and of the resulting secondary particles for neutrinos with energies beyond ∼100 GeV.
Produced muons are propagated to the detector and their energy loss is calculated. Since the cross section of the CC interaction is very small, simulating and followingk all the neutrino events would be disadvantageous in terms in cpu-time. Therefore, the code generates only neutrinos that interact inside or near the detector and are able to produce detectable muons. For this reason the so-called can (see Fig. 4.2), a cylindrical volume containing the instrumented volume of the detector, extended by three times the light absorption length in water measured at the Capo Passero site (λ_{abs} = 70 m). The can represents the Cherenkov sensitive volume. This means that photons produced beyond it have negligible probability to reach a PMT and produce signals. The generation volume (V_{gen}) is defined as the volume beyond which a muon has negligible probability to reach the can and its size depends on the maximum energy of the generated spectrum (E_{max}), on the corresponding maximum muon range in water R_w and in rock R_r and on the angular range of the simulation.
For a complete simulation, the generation volume will be a cylinder with an height surpassing the can dimension by R_r for up-going events or by $R_w \cos\theta_{max}$ for down-going events, and having R_w as radius. Neutrinos with energies according to a defined power-law spectrum are generated within this volume and their interactions are simulated, taking into account the different media, rock and water, around the detector. The neutrino direction is sampled isotropically in a pre-defined zenith angle range, or can be produced according to a point source with a given declination. The neutrino interactions are then simulated using LEPTO [69] (for deep inelastic scattering) and RSQ [70] (for resonant and quasi-elastic events). If the interaction vertex is outside the can, the shortest distance from the neutrino vertex position to the can is calculated. If this distance is greater than the maximum muon range at that neutrino energy, no muon produced by this neutrino will ever reach the can and the event is rejected with no further processing. For the remaining events with the interaction vertex inside the can, all the particles produced in the interaction are recorded (position, direction, energy, etc.) for further processing. On the other hand, if the vertex is outside the can, only the muon is kept and it is transported to the can using one of the muon propagation codes MUSIC [71], MUM [72] or PropMu [37].

4.1.1 Neutrino fluxes and event weights

The procedure described can generate events starting from a specific energy spectrum E^{γ}. It is possible to re-weight the flux with another spectrum to obtain the rate of event corresponding to a differential flux of a specific model:

$$\Phi^{mod}(E_\nu, \theta_\nu) = \frac{d\phi^{mod}}{dE_\nu d\Omega dS dt} \tag{4.1}$$

For this purpose the events generated with in a given interval $dE_\nu d\theta_\nu$ have to be multiplied by the ratio between the model flux and the generated flux given by:

$$\frac{\Phi^{mod}(E_\nu, \theta_\nu)}{\Phi^{gen}(E_\nu, \theta_\nu)} \tag{4.2}$$

where the flux of simulated interacting neutrinos arriving at the Earth is:

$$\Phi^{gen}(E_\nu, \theta_\nu) = \frac{d\phi^{gen}}{dE_\nu d\Omega dS dt} = \frac{N_{tot}}{V_{gen} I_\theta I_E E^{\gamma} \sigma(E_\nu) \rho N_A t_{gen} P_{Earth}(E_\nu, \theta_\nu)} \tag{4.3}$$

where:

- V_{gen}[m^3]: is the total generation volume;
- I_θ[sr] the angular phase space factor ($2\pi[\cos(\theta_{max}) - \cos(\theta_{min})]$) where θ_{max} and θ_{min} are the maximum and minimum angles of generation;
- E_{max} and E_{min} are the maximum and minimum energies of generation;
- I_E is the energy space factor, equal to $\frac{E_{max}^{1-\gamma} - E_{min}^{1-\gamma}}{1-\gamma}$ and to $\ln\left(\frac{E_{max}}{E_{min}}\right)$ for $\gamma = 1$;
- $\sigma(E)$ [m^2] is the total neutrino cross section for energy E;
- $\rho \cdot N_A$ is the number of target nucleon per m^3 (where N_A is the Avogadro's constant);
- P_{Earth} is the probability for the neutrino to penetrate the Earth. It is defined as $P_{Earth}(E_\nu, \theta_\nu) = e^{-N_A \sigma(E_\nu) \rho_\theta}$;
- ρ_θ is the amount of matter that the neutrino encounters;
- t_{gen} is the generation time;
- N_{tot} is the total number of generated events.

From eq. 4.2 and 4.3 it follows that:

$$w_{event} = \frac{\Phi^{mod}(E_\nu, \theta_\nu)}{\Phi^{gen}(E_\nu, \theta_\nu)} = \frac{V_{gen} I_\theta I_E E^\gamma \sigma(E_\nu) \rho N_A t_{gen} P_{Earth}(E_\nu, \theta_\nu)}{N_{tot}} \times \Phi^{mod}(E_\nu, \theta_\nu) \tag{4.4}$$

and so

$$w_{event} = w_{gen} \times \Phi^{mod}(E_\nu, \theta_\nu) \tag{4.5}$$

where

$$w_{gen} = \frac{V_{gen} I_\theta I_E E^\gamma \sigma(E_\nu) \rho N_A t_{gen} P_{Earth}(E_\nu, \theta_\nu)}{N_{tot}} [GeV \cdot m^2 \cdot sr \cdot s] \tag{4.6}$$

is independent from the particular flux choice and can be calculated in the generation phase.

4.2 Propagation of τ Neutrinos and τ Leptons through the Earth

At energies $E_\nu \sim 1$ PeV a general approach to discriminate rare neutrino events from the atmospheric muons and neutrinos is to select events from the lower hemisphere. These events can be produced by neutrinos, that can pass through the Earth with negligible absorption below these energies. Neutrino cross sections increase with energy and for muon neutrinos, absorption is considerable above 1 PeV, depending on the zenith angle, hence on the path-length transversed in the Earth [73] . Since we expect ν_τ neutrinos in the cosmic neutrino flux, it is important to include in the Montecarlo simulator, the propagation effect for these particles and for the secondary neutrinos produced. For this purpose a τ-neutrino generator, that should account for the ν_τ chain processes that occur in Earth, it is necessary. In the previous GENHEN version, the propagation is taken into account only in weights including the transmission probability calculated for each event according to [37]. The transmission probability that is the probability for neutrino to penetrate the Earth surviving CC interaction is given by:

$$p_{trans}(E_\nu) = e^{-N_A \sigma_\nu(E_\nu)} \int \rho_\theta(l) dl \tag{4.7}$$

where $\rho_\theta(l)$ is the Earth column depth in the neutrino direction θ. Another important quantity to take into account is the absorption probability, i.e. the probability for a neutrino to undergo a CC interaction and disappear, is given by:

$$p_{abs}(E_\nu) = 1 - p_{trans}(E_\nu) \tag{4.8}$$

This method neglect the effect on NC interactions that produce another neutrino with an energy lower than the parent one. This omission can be accepted since $\sigma_{NC} \sim 0.4\sigma_{CC}$ but only for ν_μ and ν_e. τ neutrinos generate τ-leptons via charged current (CC) interactions in the Earth.

$$\nu_\tau N \rightarrow \tau N \quad (CC) \tag{4.9}$$

Since τ is a short-lived particle, it decays in flight producing another ν_τ and, in $\approx 35\%$ of the cases secondary muon and electron neutrinos which are generated in decay modes:

- $\tau \rightarrow e\nu_e\nu_\tau \quad (B_e = 17.84\%)$
- $\tau \rightarrow \mu\nu_\mu\nu_\tau \quad (B_\mu = 17.36\%)$ [74]

The generated ν_τ can interact again giving the so called "regeneration-chain" that leads to the "transparency" of Earth for ν_τ, though it causes energy losses and hence a "pile-up" of ν_τ's at lower energy [75]. Processes undergone by τ-neutrinos during propagation through the Earth are shown schematically in Fig. 4.3. A first successfull attempt to introduce the regeneration- effect in GENHEN is described in details in [75]. This version of the code however does not include the treatment of the secondary neutrinos produced in τ decay.

4.2.1 A new GENHEN version

A new version of GENHEN has been introduced to take into account the propagation of secondary neutrinos generated in ν_τ interactions.
For this purpose a new parameter (SIMNUX) has been introduced to allows the user to decide whether or not to process secondary neutrinos referred as ν_x. The method consists in storing the secondary neutrinos in a separate file during the standard simulation of the primary ν_τ and process them at the end of the standard event loop. Since GENHEN simulates separately different neutrino events, as well as the CC and NC interactions a first step in the reprocessing of the secondary neutrinos is the re-initialization of quantities related to flavor (like the generation volume) and the interaction selected for primaries. Another important issue is the is the recalculation of the particles weights since is the only way to estimate the real importance of introducing secondary neutrinos . From eq. 4.6 and 4.5 we can deduce that the event weight strongly depends on the energy in the spectral factor E^γ, in the cross section and the generation volume. To correctly evaluate the weight related to a secondary neutrino events, we have to force to use the secondary neutrino's energy.

4.2.2 Secondary neutrinos introduction: results

In this section we will show the results obtained introducing in the generation process the secondary neutrinos generated by ν_τ interactions in Earth. The picture on the left in Fig. 4.4 shows the can events of ν_μ (solid blue line) and ν_e (solid red line) for energies from 10 GeV to 10^9 GeV underlining the important contribution of the secondary neutrinos represented by the dotted line. The gain for energy bin is represented on the top left in figure 4.4 showing that it is around 10% for energies from 1^6 to 1^8 GeV. The gain becomes very important for particles with a zenith angle from 0 to 10° reaching the 30% for ν_μs and the 100% for ν_es [76].

4.2.3 Generation of atmospheric muons

The generation of atmospheric muons can be performed using programs like CORSIKA [78] that allows a detailed simulation of extensive air showers initiated by high energy cosmic ray particles. Since this method is very expensive in terms of computing time, a fast MC generator is essential especially when the simulation is for a very large detector. The software used for KM3NeT and ANTARES simulations is the MUPAGE [79] package that reduces at minimum the time of calculations. The program is developed from parametric formulas derived in [79] that describe the flux, the angular distribution and the energy spectrum of underwater muon bundles with depth from 1.5 to 5 km w.e. and with zenith angles less than 85°. The parametrization of the interaction of cosmic rays and the propagation in the atmosphere up to the sea level is based on HEMAS [80] code, while the propagation of muons until 5 km under the level of the sea was performed by MUSIC [81]. MUPAGE generates muons directly on a cylindrical can surface assuming that all the muon bundles are parallel to the axis of the shower and that they arrive at the same time into a plane perpendicular at the axis. The livetime, i. e. the interval of time in which the flux corresponding to N muons is produced in nature is estimated for every N simulated events.

4.3 Propagation of particles and light production

Once that particles are generated they must be propagated through the volume. We have to consider the light produced in water for three types of particles inside the can:

- Muons, characterized by long and approximately straight tracks, that continuously lose energy and emit Cherenkov photons. They also suffer stochastic losses which produce independent EM showers.

- EM showers, produced by bremsstrahlung photons from muons or by electrons at the neutrino interaction vertex for which all the energy is deposited in a short distance . They contain a large number of electrons and hence, statistically, showers of a similar energy all have similar properties.

- Hadrons produced at the neutrino interaction vertex that have complex decay chains and the amount of light they produce depends on the primary particle and its particular set of decays. In addition, they may produce muons in the final state which may travel a significant distance. For this reason the parametrization is more difficult that the previous cases.

The codes that propagate and simulate light are KM3 and GEASIM.

4.3.1 KM3

KM3 [82] is used to generate the light produced by the muon taking into account all the muon interaction mechanisms with matter (multiple scattering, ionization, bremsstrahlung, couple production, anelastic scattering etc.), its energy loss and Cherenkov photons emission, with all the related absorption and diffusion processes in the sea water. The produced photons are then propagated to the Optical Modules (OMs).
The simulation of each single photon would take huge CPU time but this can be avoided by generating absorption and diffusion photon tables with different photon energies and then using interpolations on these tables. These tables also contain the OM properties and have to be re-calculated for each type of OM that is considered.
The KM3 package is divided into three sub-packages:

- GEN that generates "photon fields" at various radii from a muon track segment or an electromagnetic shower;

- HIT that transform the photon fields from GEN into "hit probability distributions" in a photomultiplier tube;

- KM3MC which uses the hit probability distributions generated in HIT along with a geometrical description of the detector to simulate events in it.

GEN

GEN simulates the generation of Cherenkov light by a particle in a given medium (in this case water), including light from any secondary particles. using a complete GEANT3.21. The code tracks the Cherenkov photons through space with wavelength-dependent absorption and scattering taken into account, recording the position, direction and arrival time of photons at spherical shells of various radii. GEN's output consist of a table containing all the photons recorded in each spherical shell and an file containing the information relevant to the simulation (particle type, energy, number of processed events, track length, medium type, number of events stored in each shell, water model used, etc.).

HIT

HIT creates the Optical Module hit distributions for muon track segments and EM showers, using the photon fields created by GEN. The hit position, direction, energy and time are read shell by shell and stored. Since a large number of hits is recorded for each shell, these shells are divided in bin of $\cos\theta$ and or each bin the flux of photons is weighted by the PMT effective area and orientation.

KM3MC

KM3MC first reads the users inputs and the output of HIT. Muons are than propagated through the can volume with the MUSIC package, generating segment of track (of the same dimension of those used by GEN) until the muon stops or leave the detector. If the energy loss is greater than a threshold value, an EM shower is generated in a random position of the segment track. From tracks parameter and showers (initial and final position, direction, time of occurrence) and from photon tables are obtained the signal "hits". Every hit is characterized by the identification of PMT involved, by the number of deposited photoelectrons (p.e.) and by the photon arrival time.

4.4 Generation of optical background: MODK40

Once the muon-induced photon hits are stored, MODK40 is used to add spurious hits due to the submarine optical background. MODK40 permits to generate random hit with a frequency defined by users in an interval of time $\Delta t = (t_f - t_l) + 2t_O$, where

t_f and t_l are the arrival times of the first and the last hit of the event respectively and t_O the delay to add before and after the simulated event (in the simulations presented in this thesis t_O = 1000 ns). MODK40 can also simulate the digitalization of the detector. It can transform the light simulated Cherenkov photons with optical background into a electronic signal with the appropriate gain factors and electronic noise.

A random background rate of 5 kHz is assumed for each PMT, including dark current, ^{40}K decays, and bioluminescence. In addition to random coincidences, an L1 (two coincident hits in different PMTs inside the same DOM) rate of 500 Hz is assumed, due to genuine coincidences from potassium decays.

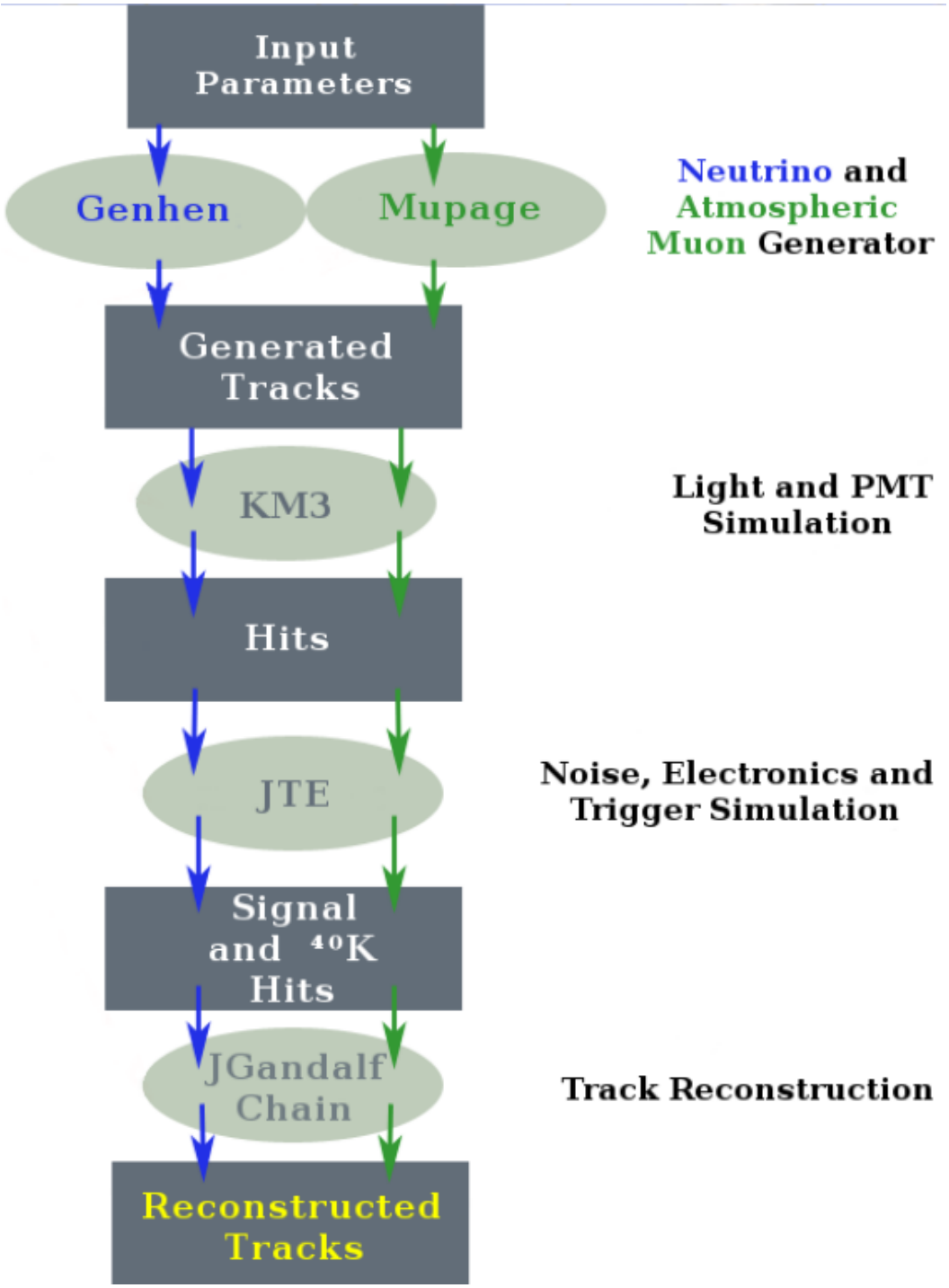

Fig. 4.1: Scheme of the codes used to simulate the events in ANTARES and KM3NeT.

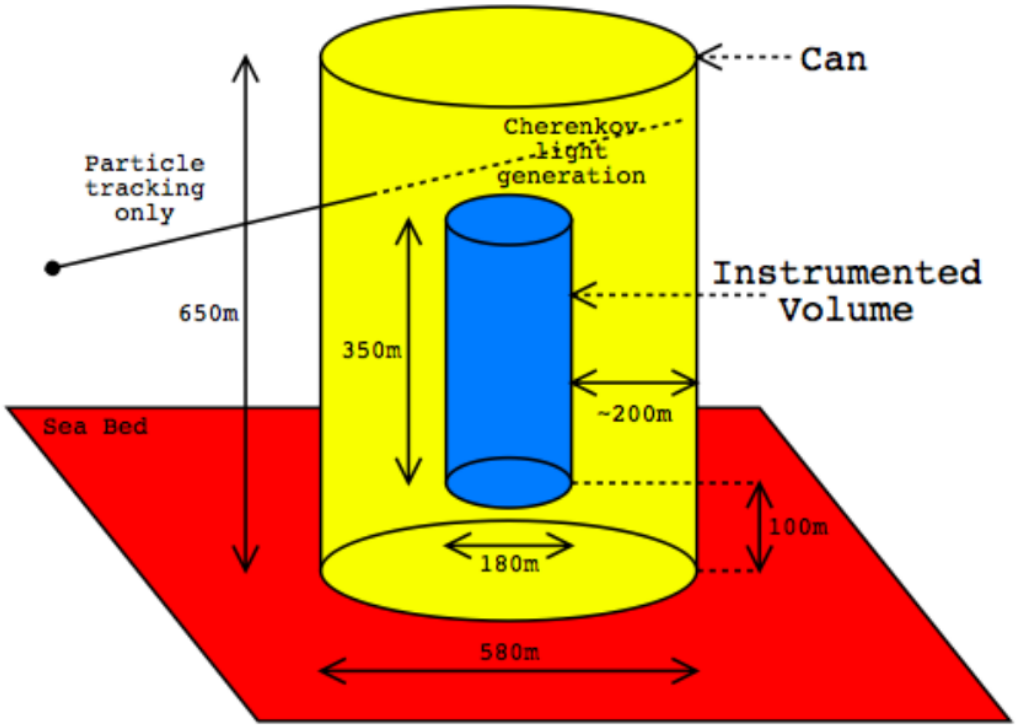

Fig. 4.2: Overview of the detector geometry for the event simulation used in GENHEN. Neutrino interactions are generated in a large volume (tens of kilometres). The generated muons are propagated to the can (yellow) where the Cherenkov light and the detector response are simulated [68].

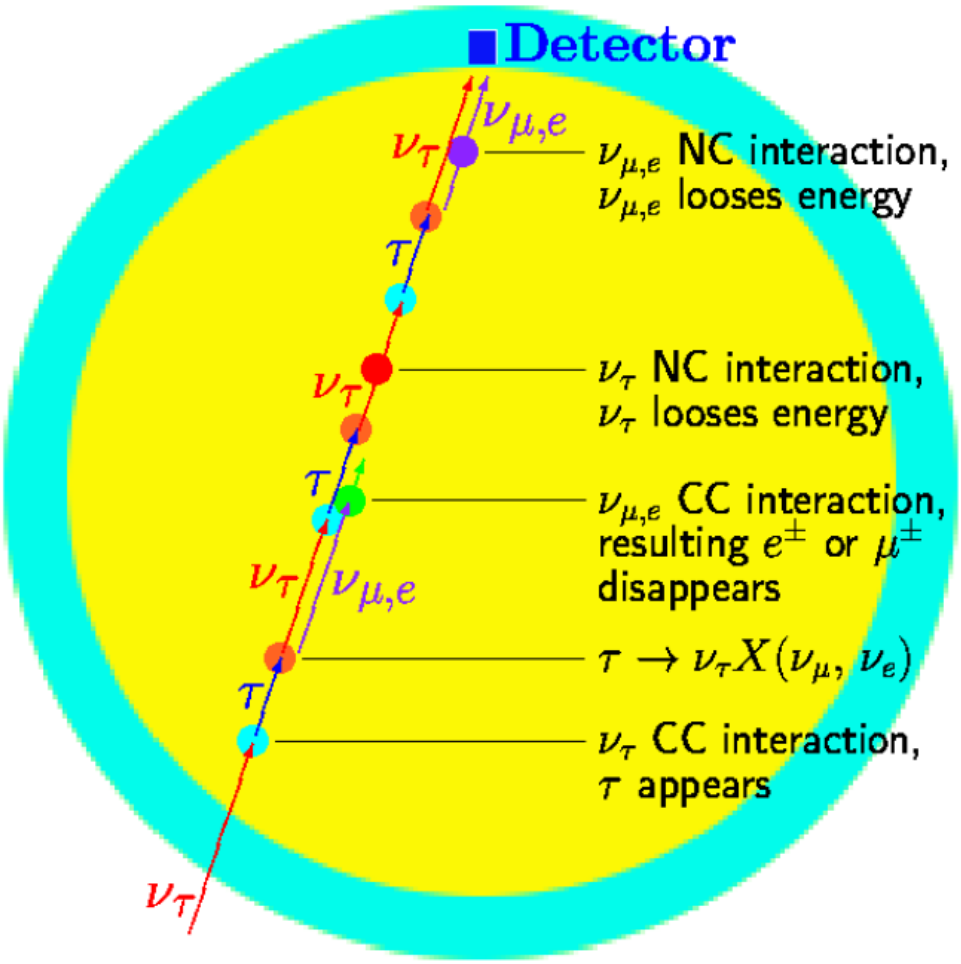

Fig. 4.3: Schematic view of the pile-up process induced by high energy ν_τs propagating through the Earth [75].

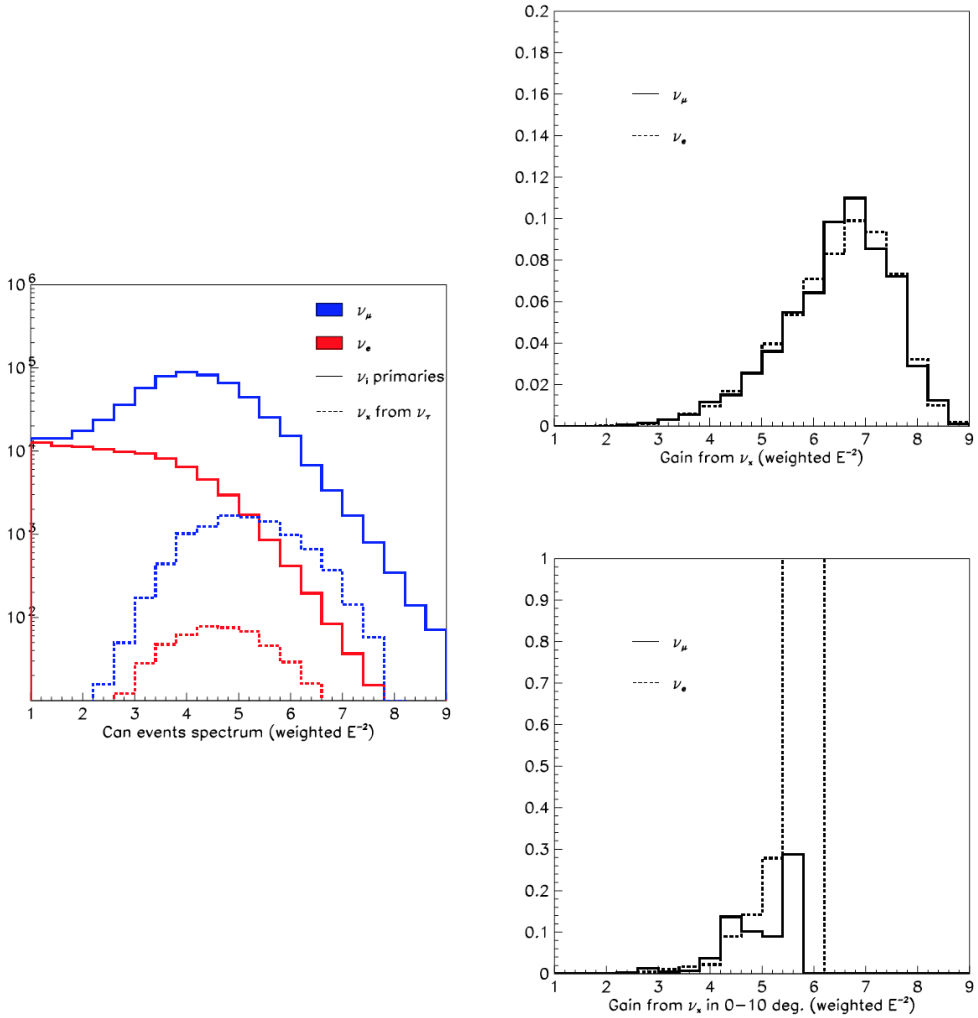

Fig. 4.4: Left: Can events of primary ν_μ (solid blue line) and ν_e (solid red line) for energies from 10 GeV to 10^9 GeV and secondary ν_μ (dotted blue line) and ν (dotted red line).
Top right: Gain for ν_μ (solid) and ν_e (dotted line) for energies from 10 GeV to 10^9 GeV.
Bottom right: Gain for ν_μ (solid) and ν_e (dotted line) with a zenith angle from 0 to 10° for energies from 10 GeV to 10^9 GeV. In all the plots the energies are in logarithmic scale. [77]

5

Characterization of the photomultipliers for the KM3NeT Neutrino Telescope

The search for high-energy neutrinos involves the construction of very large experimental apparatuses and consequently leads the use of thousands of particle detectors. Photomultipliers (PMTs) are considered optimal detectors for photon detection thanks to their excellent timing and single photon counting capability and are the solution chosen for the KM3NeT telescope.
The characteristics of the PMTs affect the detector event reconstruction accuracy. Therefore the Collaboration studied the desirable parameters for the PMTs to be installed (see Table 5.1) and finds in the Hamamatsu R12199-02 PMT the optimal candidate for the first phase of the KM3NeT detector.
The Hamamatsu R12199-02 is a 80 mm diameter hemispherical PMT with 10 dynode stages and standard bi-alkali photocathode. Since the PMT performance has an important role in the neutrino event detection and reconstruction, the KM3NeT Collaboration has decided to perform dedicated studies on critical parameters, including a measurement of Quantum Efficiency (QE) and calibration of time over threshold, and to fully characterize a large sample of devices. In the following we present the results of this characterization that will be used as input of the numerical simulations of the detector response.

Photocathode diameter	>72mm
Nominal Voltage for gain 3×10^6	900 ÷ 1300 V
Quantum Efficiency at 470 nm	>18%
Quantum Efficiency at 404 nm	>25%
Peak-to-Valley ratio	>2.0
Transit Time Spread (FWHM)	<5 ns
Dark count rate (0.3 SPE threshold, at 20°C)	2000 cps max
Prepulses between -60 ns and -10 ns	1.5 % max
Delayed pulses between 15 ns and 60 ns	5.5 % max
Late afterpulses between 100 ns and 10 μs	15 % max

Tab. 5.1: Requirements for main characteristics of PMTs to be used in the KM3NeT detectors (is for single photoelectrons; cps is for counts per second)[83].

5.1 The DarkBox

In order to significantly speed up the massive test and calibration of a huge number of PMTs, the KM3NeT collaboration developed an instrument, called DarkBox[83], optimized to tune the high voltage (HV), have equalized gain, and measure timing resolution, charge resolution, dark counts and spurious pulse rates.

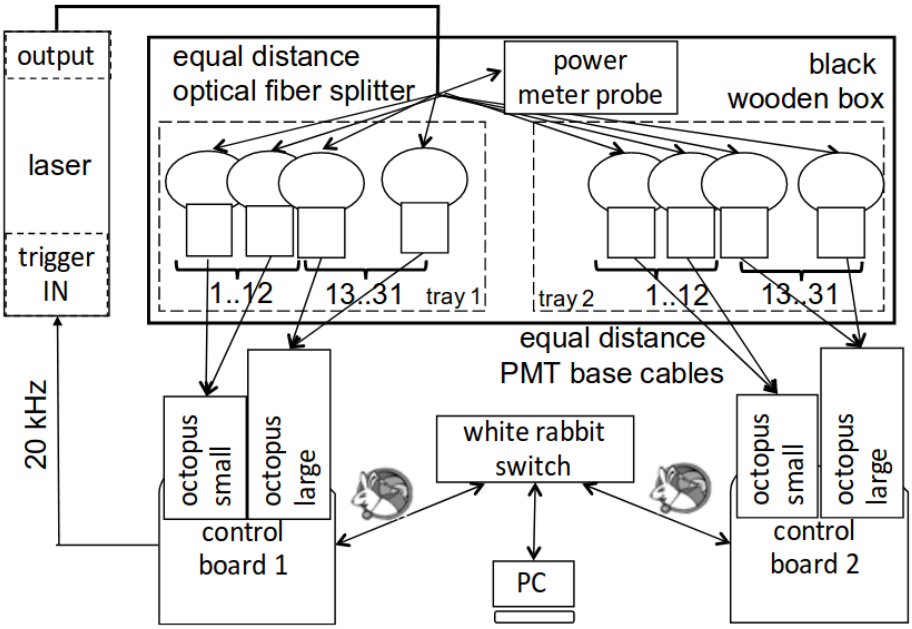

Fig. 5.1: DarkBox experimental setup scheme

It consists of a wooden box (120 cm × 88 cm × 58 cm (height)) that allows simultaneous characterization of sixty-two 3-inch PMTs. The box walls are black painted externally and internally. As can be seen in Fig. 5.1 particular attention has been devoted to the edges and the corners, usually the most critical regions, to guarantee light tightness. A vertically opening front door (not shown in the picture) is locked tightly by two lever-operated latches on each side (left and right). The DarkBox comprises also two removable trays loadable with 31 PMTs each before the insertion into the DarkBox. They allow easy and fast PMTs re-installation, thus optimizing the operation time. Metal arms are attached to each tray on both sides for the grip during the trays exchange operation. The photomultipliers are maintained in a vertical position with photocathode area looking down. Polyvinyl chloride collars and elastic bands fix PMTs in the area around the dynode chain (see Fig. 5.3) so the photocathode is not in contact with the structure. This is mandatory for PMTs fed with negative voltage at the cathode. The holders have tiny teeth on the lower openings (see Fig. 5.3 left) to prevent the PMTs from falling down during loading and unloading operations. A time-calibrated electrical cabling system was realised to connect PMTs to the data acquisition system placed outside the box, maintaining

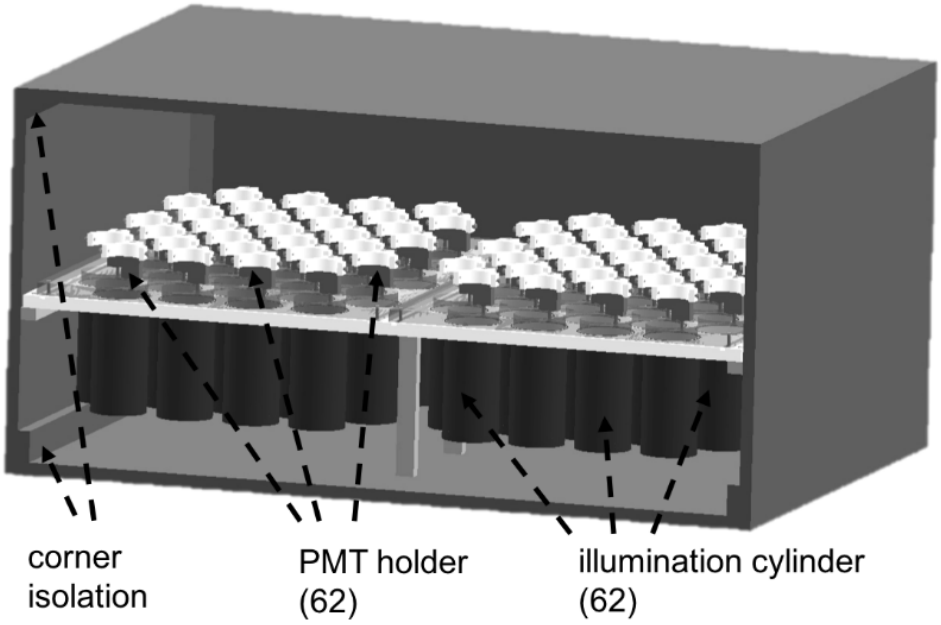

Fig. 5.2: Wooden dark box with two removable PMT holder trays placed above the support structure. The latter has plastic cylinders to provide uniform PMT illumination and optically isolate each test socket. Wooden bars on the inner corners and edges are added to ensure the light-tightness[83].

for all PMTs the same time signal delay. The distribution of single photon signal to all PMTs is made using a picosecond accuracy laser and a calibrated optical splitting. The front-end electronics, data management and analysis software are based on the technologies developed by the KM3NeT Collaboration [83].

5.1.1 Laser calibration system

The measurement of the PMT gain, transit time and spurious signals requires homogeneous PMT photocathode illumination with single photons. The arrival time of the photons to the PMT surface should be known with sub-nanosecond precision for the timing characteristics measurements. A single short-pulse laser with a fiber optic system to deliver the photons to each PMT was chosen for the operation simplicity and the cost. For this reason a laser controller equipped with a 470 nm laser head is used in external trigger input mode and the trigger is generated by the data acquisition system to provide common time reference for the emitted photons and the detected PMT signal. In order to guarantee that photons arrive with the same delay and quantity at each PMT, an optical splitter with good uniformity in power distribution and equal light paths for each channel has been used. It is made of an input fibre having 600 μm core diameter and 70 output channels, coupled with the main fiber, having 25 μm diameter fiber core each. All outputs have a fraction of the input power in the range 0.5% - 1.5%. The lengths of the output fibers are made

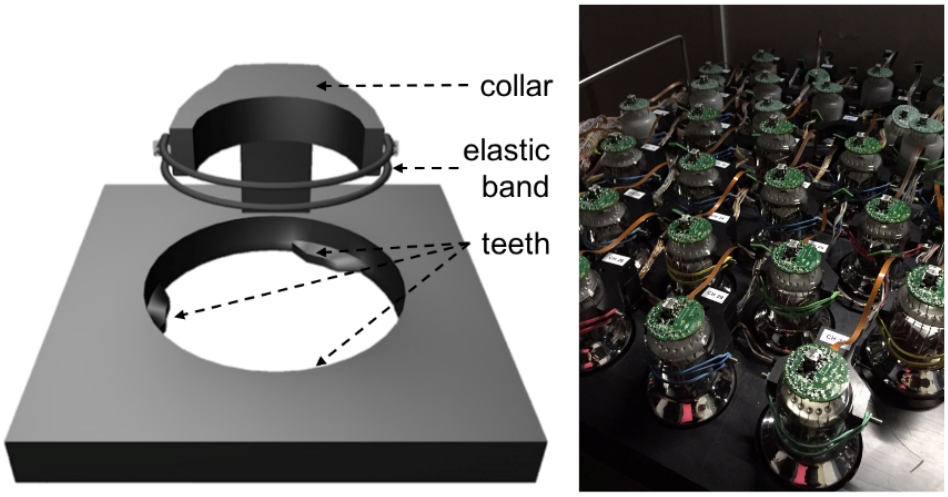

Fig. 5.3: The DarkBox tray holder unit (left) and the tray loaded with 31 PMTs (right)[83].

equal with millimeter precision to equalize the time delays which are at least below the required precision.
The qualification tests should reproduce the uniform PMT illumination in working environment. This condition is obtained by placing PMT upside-down on top of a black cylinder (see 5.4) which has a small central hole in the bottom for the entrance of the optical fiber. An opalescent diffusing glass disk is coupled with the optical fiber and placed in the hole. It helps in reaching better illumination uniformity. The single

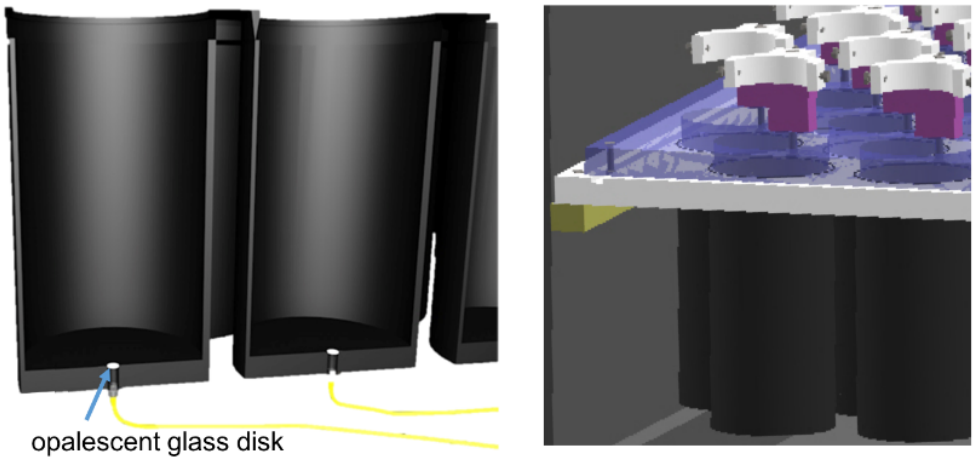

Fig. 5.4: The inner structure of the dark cylinders (left) and the external view of the cylinder with a PMT holder (right).

photon operation mode is reached by using a tunable (passive) optical attenuator placed in the optical fiber distribution system. It has a dynamic range of about 20 dB. In case more optical power is needed, the attenuator can be adjusted without changing the laser setting. A spare fiber of the splitting system is used as a reference and monitored to check the single photoelectron operation mode by connecting it to

a power meter, whose sensitivity is 0.4 pW.
The delay between the electric trigger signal and the optical pulse signal arriving to the end of the splitter fibers was measured using an oscilloscope coupled with optical to electrical converter. The propagation time of the light in the cylinder is calculated including the time spread due to cylinder height and PMT radius. The full time delay between the trigger generation and photons arrival to the PMT surface is evaluated with an accuracy of about 100 ps.

5.2 Front-end electronics and data acquisition system

The KM3NeT PMT assembly is composed by a 3-inch PMT coupledwith a custom active base, that provides the needed HV by means of a Cockcroft-Walton[1] generator [84]. The base has a control chip with a serial communication interface to set up the high voltage and to provide a unique identifier. The base electronics shapes the anode signal and converts it into a low voltage differential signal whose time duration is proportional to the signal charge[**pmt**]. The discriminator threshold is adjustable through the PMT base control chip; the default value used corresponds to 0.3 photoelectrons (p. e.). For each group of 31 PMTs the control and data acquisition is performed by using a custom FPGA-based control board, that is designed and used in the KM3NeT optical modules. The interface between each PMT base and the control board is obtained through two so-called octopus boards of different sizes: a small octopus board (12 channels) and a large one (19 channels). Time-delay equalized cables are used to connect the PMT assemblies and the control boards. A time-to-digital converter in the control boards digitizes the PMT differential signals, recording the start pulse ToT that is proportional to the PMT charge. Each control board packs the incoming data from the 31 PMTs into Ethernet data packets and sends them through a local Ethernet network. The management of the control boards is performed using a data acquisition PC through the same Ethernet connection.
The data acquisition setup consists of a Personal Computer (PC) connected through copper Ethernet cable to a White Rabbit Switch. the two control boards are kept at the same clock frequency and synchronized (same phase delay) with sub-nanosecond accuracy through the White Rabbit gear installed on the FPGA of the switch (White Rabbit Master) and on the two control boards (White Rabbit Slaves). The connection between the switch and the control boards is performed via single optical fiber lines following the White Rabbit standards. The PMT data and management commands are transmitted between the control boards and the PC through the switch following

[1] The Cockcroft-Walton generator is an electric circuit that generates a high DC voltage from a low-voltage AC or pulsing DC electrical power. It is made up of a voltage multiplier ladder network of capacitors and diodes to generate high voltages.

the same connection lines. The trigger input signal for the laser controller is generated by one of the control boards. Therefore, it is perfectly synchronized with the data acquisition electronics. The trigger frequency can be remotely adjusted in the range 0.1 âĂŞ 100 kHz. For this application a custom manager tool, based on Java and interfaced with the KM3NeT software tools, has been developed to read-out PMT data from the control boards and upload/download recorded parameters into a relational database. This tool performs the following operations:

- Defines a unique identification tag for each test; create a directory where data and information for each test are stored;
- Interfaces with the database by retrieving the default PMT settings using the identifiers of the connected PMT provided by the PMT base control chips;
- Interfaces with KM3NeT detector control and data acquisition software setting proper threshold and HV for each PMT and test run numbers (to identify different measurement phases);
- Starts and stops run;
- Records raw PMT data;
- Creates ROOT files for data analysis;
- Produce XML and files with the results to be uploaded into the database.

5.3 Quantum efficiency measurements

The photocathode QE is measured in DC-mode, without any amplification and with 100% collection efficiency. The PMT is illuminated with a xenon lamp whose light, after passing through a mono-chromator, produces a 1 cm spot on the photocathode. The light intensity is determined using a reference photodiode, calibrated by Hamamatsu in the wavelength range of 200 ÷ 800 nm, in steps of 10 nm with a precision of 0.1%. Reference measurements are repeated hourly. The scheme of the test setup used for QE measurements is shown in Fig. 5.5. The quantum efficiency is defined as the ratio between PMT and photodiode photocurrents weighted with the known QE of the photodiode and is measured in the wavelength range of interest, 280 Ãů 700 nm, in steps of 5 nm. More details on the method and on the possible systematics associated with the measurement can be found in [86]. The photocathode QE has been measured for 56 PMTs chosen randomly in order to cross-check the measurements

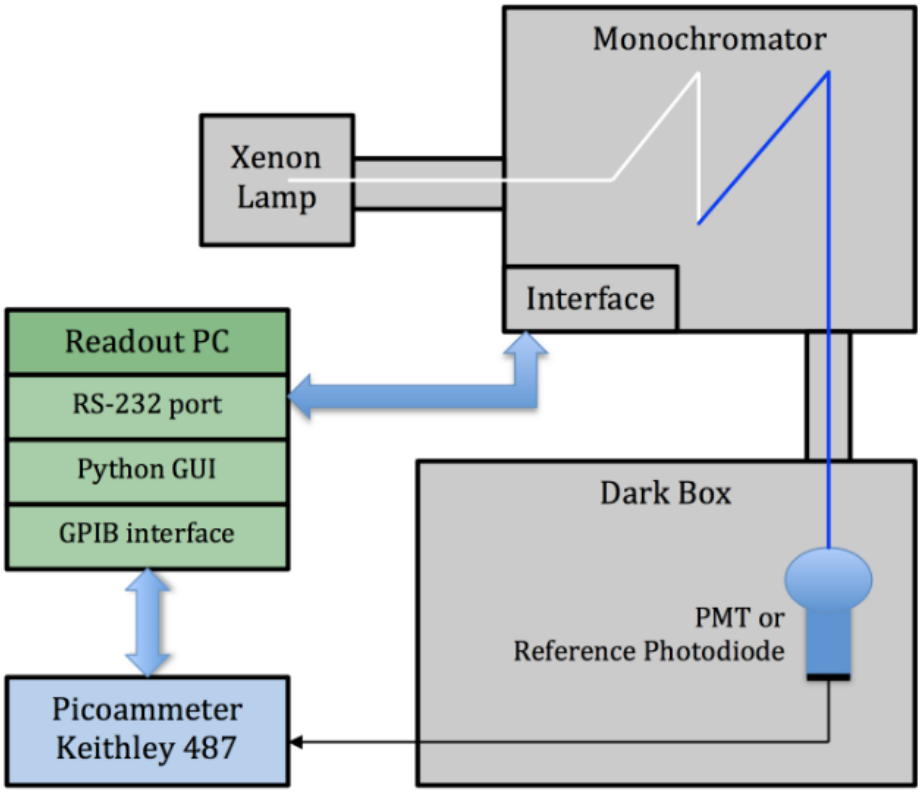

Fig. 5.5: Scheme of the test setup for photocathode quantum efficiency measurements [85].

performed by the manufacturer on the full production. The results are presented in Fig. 5.6 in which the green lines represent QE curves for individual PMTs and continuous black curve is the mean value with one standard deviation at each measured wavelength. For the wavelengths indicated in the KM3NeT specifications [47], the mean QE values with one standard deviation are:

- $(26.9 \pm 1.2)\%$ at 404 nm
- $(21.6 \pm 1.5)\%$ at 470 nm

The results are in agreement with the requirements.

5.4 Gain and high voltage calibration

The manufacturer provides for each PMT the nominal HV needed to achieve the gain, defined as the ratio between anode and photocathode currents, of 3×10^6. In KM3NeT application, PMTs are not used in current, but in pulse mode. So differences

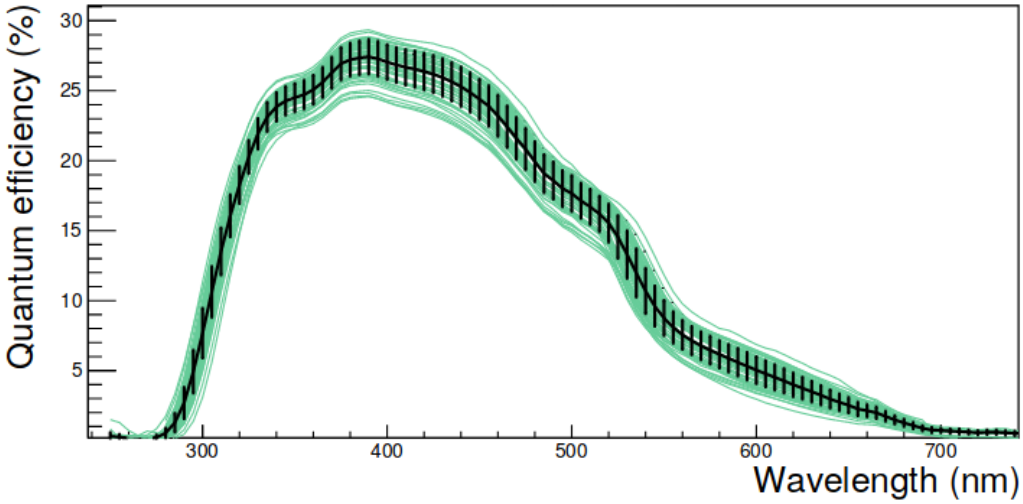

Fig. 5.6: Photocathode quantum efficiency measurements as a function of the wavelength for 56 PMTs. The green lines show the results for individual PMTs. The continuous black curve is the mean value with one standard deviation at each measured wavelength [85].

in nominal voltages are expected. Therefore, a method of HV tuning in order to get the above indicated gain in pulse mode has been developed. The nominal HV has been determined for a sub-set of 66 PMTs with resistive bases having a high voltage division ratio of 3 between the photocathode and the first dynode, and of 1 between all other dynodes, as specified by the manufacturer. In a DarkBox the whole PMT surface is uniformly illuminated by fast LED pulses (460 nm central value with a 800 ns FWHM) at 1 kHz frequency. Light from the pulser is delivered to the dark box via an optical fiber. A diffusor is installed at the fiber output at a distance of $\sim$1 m from the PMT. The pulser amplitude is tuned to obtain a mean number of $\sim$ 0.1 photons per pulse detected by the PMT. The signal is amplified ten times and sent to a LeCroy Waverunner 6100 oscilloscope. The latter is triggered with the sync signal from the pulser and the waveforms of PMT signals are saved with a sampling rate of 10^9 samples per second. The gain is calculated integrating the signal within a gate of 20 ns and fitting the distribution with a Gaussian function. Measurements of the gain are performed at seven different voltages in steps of 25 V around the nominal HV value provided by the manufacturer. These results are used to fit the gain-HV linear dependence in a double logarithmic scale (gain slope). The HV value corresponding to the desired gain is calculated from the fit with 1 V precision. In Fig. 5.7-left the histogram with the gain slopes is shown. The difference between the calculated HV and the ones given by the manufacture is presented in figure 5.7-right. The systematic difference can be explained with the different methods used for gain measurement.

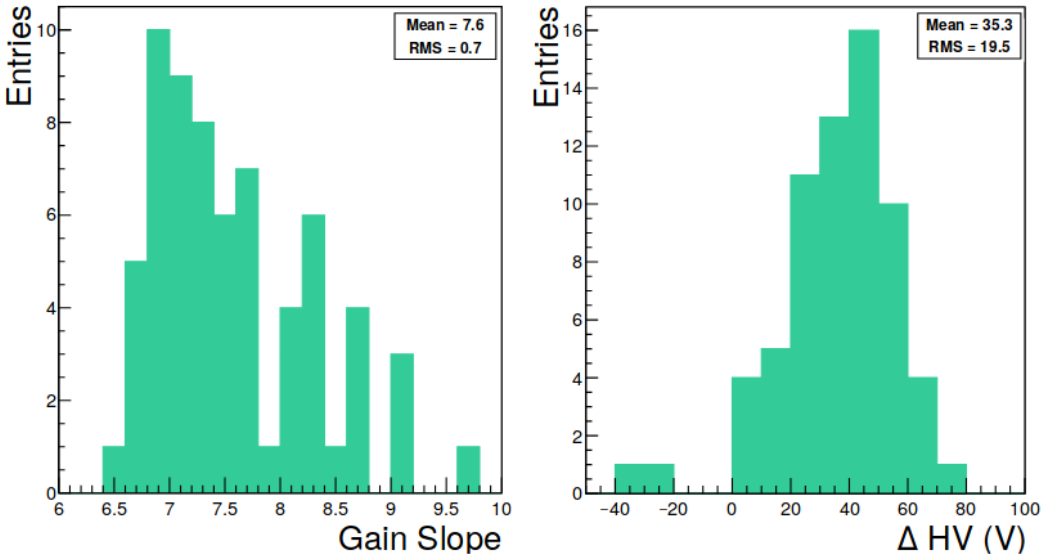

Fig. 5.7: Left: distribution of the HV gain slope (see text for the definition). Right: difference between the determined high voltage values and those provided by the manufacturer to achieve a 3×10^6 gain [85].

5.5 Timing properties and noise pulses

In this section we will present the results obtained by testing 6960 PMTs. The accurate, but time consuming, HV tuning procedure described in the previous section is not possible for the PMTs installed in the apparatus and is disadvantageous when testing a large number of PMTs. For this case, the PMT gains are equalised based on the indirect observable of the ToT value. For each PMT the HV value is set in order to have the peak value of the time over threshold distribution at 26.4 ns, for a single photoelectrons () signal at 0.3 threshold [47]. These values are referred to as the "tuned HV" [87]. During a run with laser, the ToT distribution of the first hit is collected. This distribution has a peak in the range 26-27 ns confirming the reliability of the automatic HV calibration tuning. The results discussed in the following sections have been obtained with the tuned HV.

5.5.1 Dark count rates

The dark counts are random noise pulses that can be measured at the anode of a PMT even in total darkness. The most significant source of random noise for a PMT is the spontaneous thermionic emission of electrons by the photocathode. Pulses that result from this process correspond mainly to a single photoelectron. The rate at which these pulses are observed is proportional to the photocathode area and varies considerably depending on the photocathode material. Bialkali photocathodes (as those used in KM3NeT PMTs) have the lowest ratio per unit area. Another

source of dark pulses is the natural radioactivity in the structure of the PMT itself. The most important components are usually ^{40}K and Th contained in the glass envelope. These elements, in their radioactive decay, emit β particles that will give a flash of Cherenkov radiation that can produce photoelectron emission from the photocathode[88]. Once the PMTs are fed with the tuned HV, dark count rates are monitored for 9 hours. During this time, the PMT is initially affected by the initial exposure to the light but steadily the dark count rate becomes stable. The measured rate is the average over the last 100 s of the run for each PMT. The results are shown in Fig. 5.8. The average dark count rate is about 1300 cps, while the fraction of

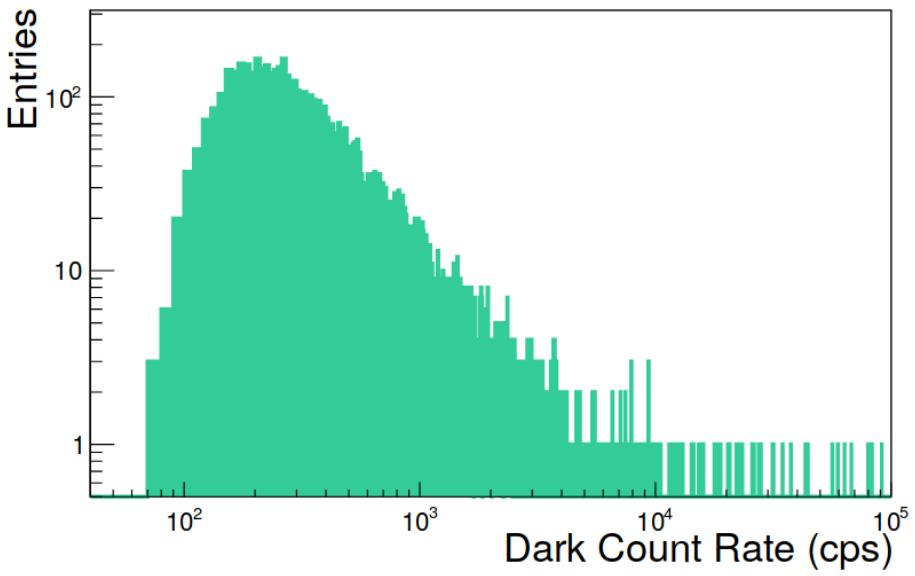

Fig. 5.8: Dark Count rate for the full PMT sample tested [85]. The average dark count rate is about 1300 cps, while the fraction of PMTs above 2000 cps is 7.1%.

PMTs above 2000 cps, so not suitable to be integrated in the KM3NeT DOMs, is 7.1%. These PMTs were tested again after a longer darkening (48 hours) reducing this fraction of PMTs to 3.5%. The average dark count rate of good PMTs is about 700 cps.

5.5.2 Measurement of PMT time characteristics and of spurious pulses

Spurious pulses are time-correlated with the expected PMT response to light and they can come early or can be delayed by a characteristic time with respect to the electron transit time through the PMT. They are usually classified as prepulses, delayed pulses and afterpulses. The tests illustrated in this section have been made by collecting 10-minutes runs while illuminating the PMTs with a 470 nm laser, after

the needed darkening time. The laser trigger frequency was set to 20 kHz and its light output tuned so as to operate the PMTs in the regime (0.1 photoelectron per pulse). These data have been analyzed to estimate PMT timing performances and measure the fraction of spurious pulses. Time characteristics of PMTs have been measured by detecting and analyzing the so-called first photon hits, i. e. pulses detected in a window of 200 ns around the expected arrival time of the PMT signal. The distribution of arrival time of the first hits for a typical PMT is shown in Fig. 5.9a. The main peak of this distribution corresponds to the PMT TT and the Transit Time Spread (TTS) is defined as the FWHM of this peak. The Fig. 5.9b is obtained shifting the arrival time distributions of all PMTs by subtracting the transit time, normalizing, then summing all the so obtained distributions and normalizing again the resulting distribution. The resultant distribution expresses the average probability for spurious pulses and is used as input in the KM3NeT simulation tools. The distribution of the

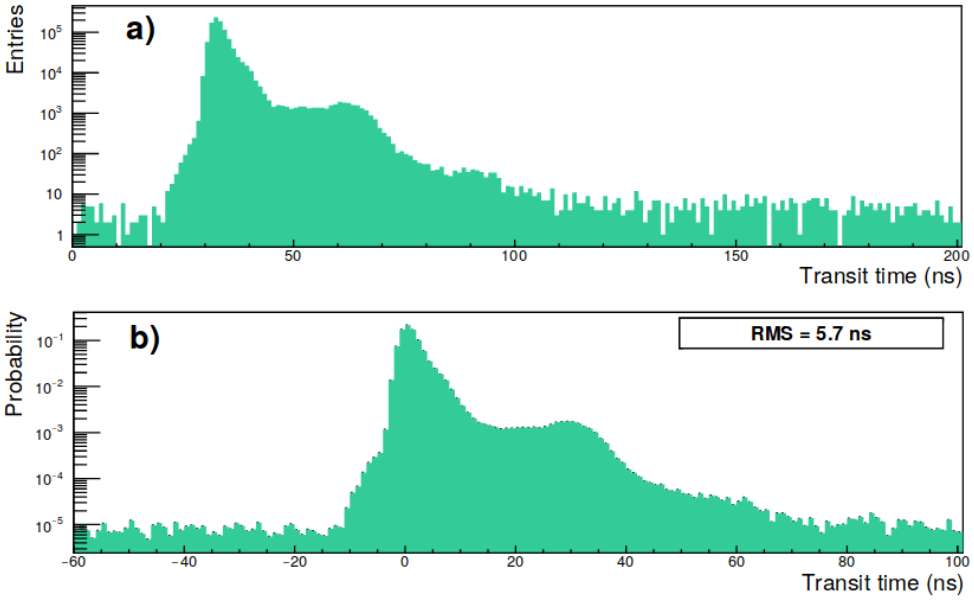

Fig. 5.9: Distribution in a) of arrival time of the first hits for a typical PMT and in b) of arrival time of the first hits normalized as to obtain the average probability for spurious pulses [85].

TTS is shown in Fig. 5.10 and presents all the values below 5ns.

Determination of prepulses and delayed pulses

Prepulses, that derives from a direct photo-effect on the first dynode due to photons that pass through the photocathode without interacting [89], appear as a non Gaussian tail on the left side of the main peak. For a 3-inch PMT the prepulse arrival time is in the range 10 ÷ 60 ns before the main pulse. The percentage of prepulses

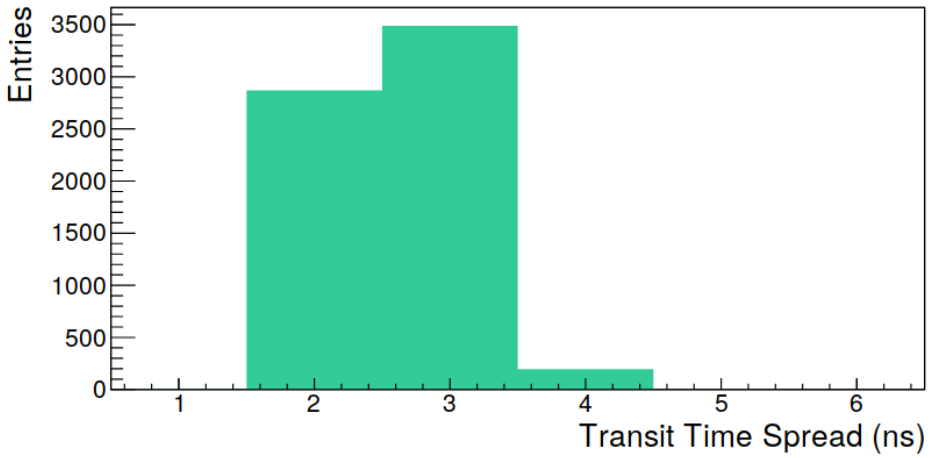

Fig. 5.10: Transit Time Spread for the full PMT sample characterized [85].

is defined as the ratio of the hits in the window [T_{peak} - 60.5 ns, T_{peak} - 10.5 ns over the number of the first hits where T_{peak} corresponds to the centre of the maximum bin. The distribution of the prepulses measured for the tested PMTs is shown in Fig. 5.11 where the 98.8% of the total sample has a prepulse fraction below 1.5%. The average prepulse fraction is 0.2%. The distribution of the delayed pulses measured for the tested PMTs is shown in Fig. 5.12. The delayed fraction is below 5.5% for the 98.5% of the total sample and the average delayed pulse fraction is 3.2%.

Determination of afterpulses

Afterpulses are noise pulses following the main PMT response to a detected light event and can be divided in early (Type I) and late (Type II) afterpulses. The early afterpulses are due to the emission of light from the stages of the multiplier structure, which can reach the photocatode producing further photoelectrons. PMTs usually exhibit Type I afterpulses in the time window 10÷80 ns after the primary pulse. The late afterpulses are caused by residual gases that can be ionized by the passage of electrons in the space between the photocathode and the first dynode and also through the multiplier structure. The positive ions that are formed will drift backward and some can find a path back to the photocathode. Since the drift velocity of the positive ions is low, the time taken to return to the photocathode can range from hundreds of nanoseconds to tens of microseconds. It also depends on the type of ions, on the position where they are generated and on the supply voltage. In a 3-inch PMT, Type II afterpulses arrive within ∼20 ns after the first hits. Afterpulses were studied by analyzing the ToT versus transit time correlation (see Fig. 5.13) in which four regions with long transit time and ToT exceeding the signal can be identified. These occurrences are due to the residual gases inside the PMT.

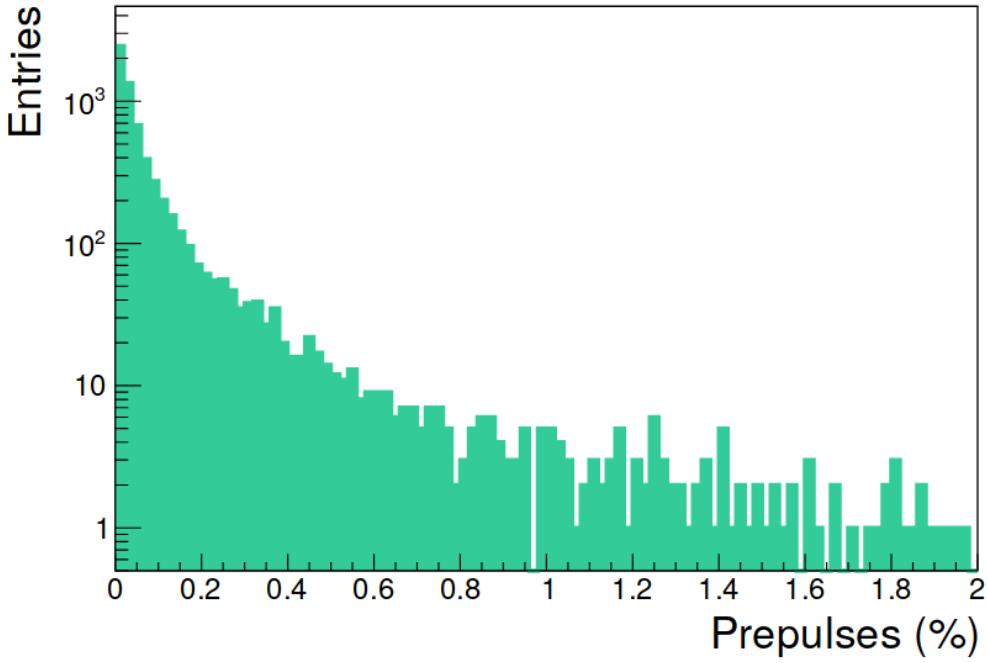

Fig. 5.11: Distribution of the prepulse fraction for the full PMT sample tested. The average prepulse fraction is 0.2% and the 98.8%of the total sample has a prepulse fraction below 1.5. [85].

- CH_4^+ ions: transit time of $\sim 1 \div 1.5$ μs
- CS^+ ions: transit time of $\sim 3 \div 4$ μs;
- H_2^+ and He^+: transit time $< 1 \mu$s.

The percentage of late afterpulses is determined as the ratio of afterpulses in the time window $[T_{peak} + 100.5\, ns,\ T_{peak} - 10\,]$ over the total number of hits. The percentages of spurious pulses of all types are corrected taking into account the dark noise hits that contaminate both first hits and spurious pulse distributions. The histogram of the afterpulse fraction measured for the whole PMT sample is shown in Fig. 5.13 where the 92.4% of the total sample has an afterpulse fraction below 15% with an average afterpulse fraction of 7.1%

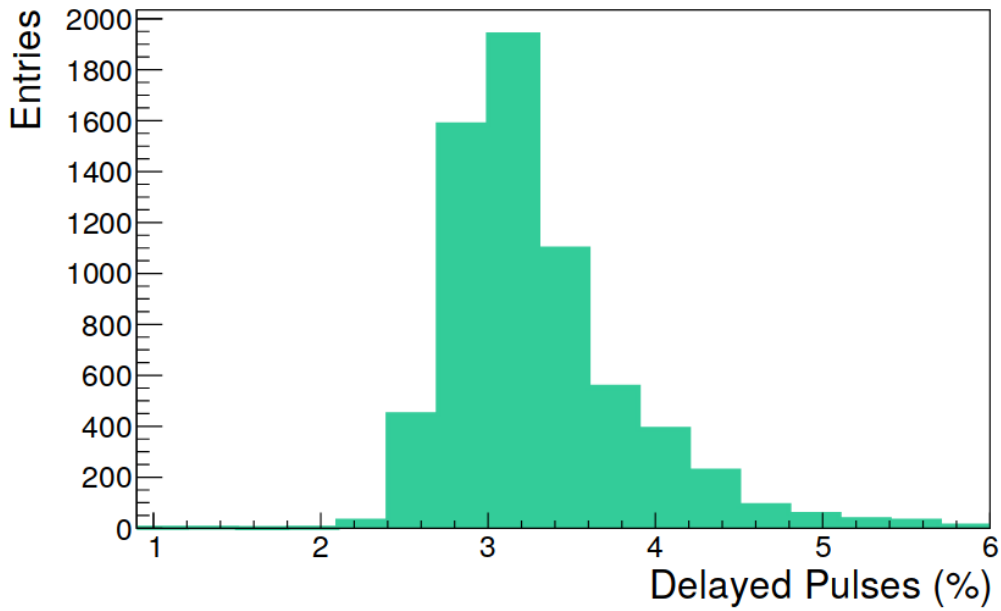

Fig. 5.12: Distribution of the delayed fraction for the full PMT sample tested. The average delayed pulse fraction is 3.2% and the delayed fraction is below 5.5% for the 98.5% of the total sample. [85].

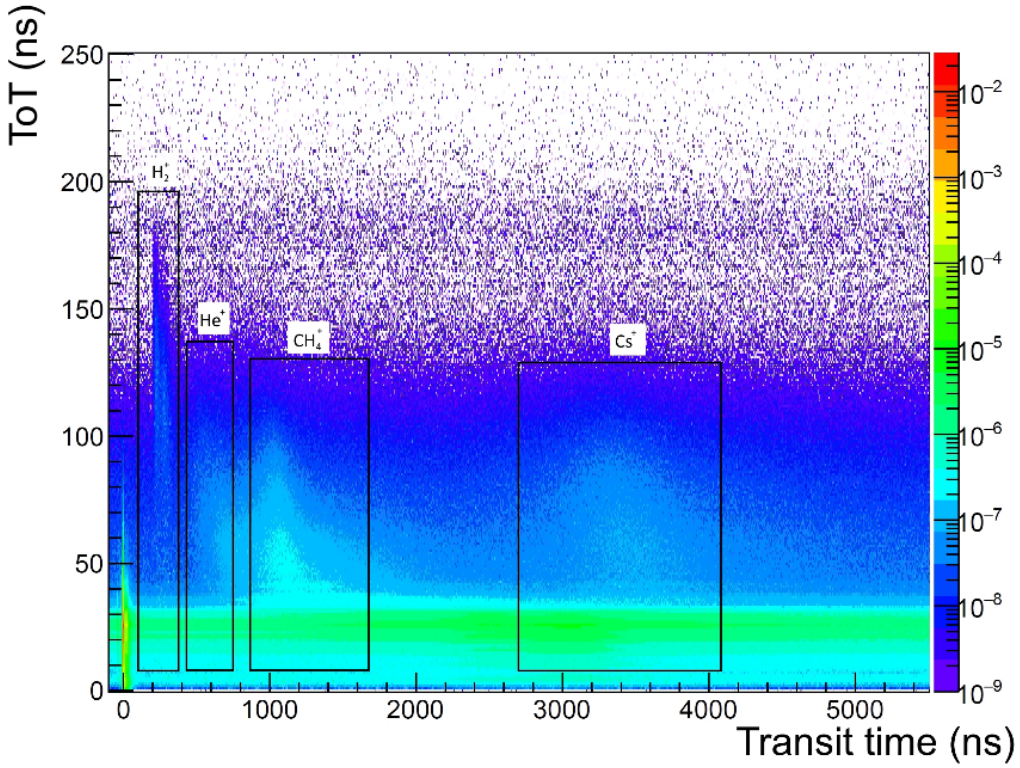

Fig. 5.13: ToT as a function of the first hit time. The regions corresponding to signals induced by different ions are also indicated. Note that the scale on the right shows the probability for a given couple (ToT;TT) to occur. The distribution is normalized over the whole plane [85].

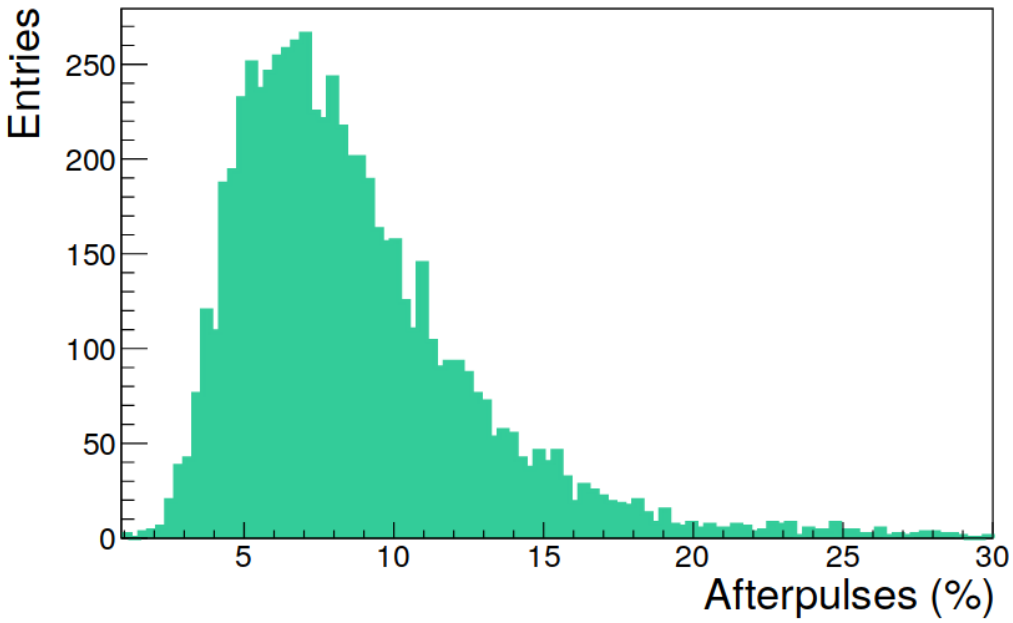

Fig. 5.14: Afterpulse distribution for the full PMT sample characterized [85].

6 Beyond the single power law neutrino flux scenario

Neutrino telescopes will play a crucial role in unveiling the physical properties of astrophysical sources such as supernovae, active galactic nuclei, gamma-ray bursts, etc., and in the possible discovery of new astrophysical sources. After the first IceCube observation of astrophysical high energy neutrinos, the feasibility of the indirect detection of heavy dark matter through its emission in neutrinos has been extensively discussed in literature [90]. In this chapter, we give an interpretation of the recent preliminary data presented by ANTARES [25] and IceCube Collaborations [91] at the 35th International Cosmic Ray Conference performing a combined analysis of both observations[92]. In the last part of this chapter is presented a first feasibility study for the indirect search of heavy dark matter through its neutrino emission with the KM3NeT Neutrino Telescope.

6.1 Use of ANTARES and IceCube Data to Constrain a Single Power-law Neutrino Flux

6.1.1 Analysis with a Single Power-law

The ANTARES Collaboration has reported in the nine year data sample [25] the observation of an excess of neutrinos over the atmospheric background . This excess for energies above 20 TeV is due to the detection, from 2007 to 2015, of 14 shower events, more than the 10.5 $\pm$4.0 expected for the atmospheric background that is dominated by penetrating muons. Considering also the track events, the ANTARES excess has a p-value of 0.15 with a significance beneath 2σ [25].
After six years of data-taking, the IceCube Collaboration has collected a total of 82 events (track + shower) with a neutrino interaction vertex that is located inside the detector [91]. This data sample is called HESE. The Icecube Collaboration has performed an analysis supposing the incident neutrinos having an energy above 60 TeV. The result of this analysis provides a best-fit power-law with spectral index equal to:

$$\gamma_{IC_{6years}} = 2.92^{+0.29}_{-0.33} \tag{6.1}$$

This spectral index is larger than the one obtained by the four year HESE data [91]:

$$\gamma_{IC_{4years}} = 2.58 \pm 0.25 \tag{6.2}$$

The difference between the results of the two best-fit in eq. 6.1 and eq. 6.2 is due to the absence of neutrinos with reconstructed energy larger than 200 TeV in the last two years of observations.
According to the Fermi acceleration mechanism at shock fronts [10] Waxman & Bahcall [93] predicted a cosmic neutrino flux proportional to $E^{-2.0}$. The larger values for the spectral index found for $\gamma_{IC_{6years}}$ and $\gamma_{IC_{4years}}$ have suggested the hypothesis of the presence of an additional component dominating for lower energies ($E_\nu \leq 200$ TeV) in addition to a single unbroken power-law flux ([94, 95, 96]. The two-component scenario is also strongly motivated by the analyses on cosmic neutrino flux from the northern performed using six years of IceCube data described in [97]. In this study, we perform a combined analysis of the diffuse neutrino flux observed by ANTARES [25] and by IceCube[91], assuming for the neutrino flux a single astrophysical unbroken power-law:

$$\frac{d\Phi_{astro}}{dE_\nu d\Omega} = \Phi^0_{astro} \left(\frac{E_\nu}{100\ TeV} \right)^{-\gamma_{astro}} \tag{6.3}$$

We suppose an equal flavor composition at the Earth, as expected for standard astrophysical sources thanks to neutrino oscillations, and an isotropic flux in angular coordinates. In addition to the astrophysical flux described by eq. 6.3, we consider the conventional atmospheric background that consists of penetrating muons and neutrinos produced by the π and K decays in the atmosphere [98]. On the other hand, we do not take into account the prompt atmospheric background composed by neutrinos produced by the decays of charmed mesons [99], according to the IceCube conclusions contained in [100, 101, 97] The combined fit is performed maximizing the binned multi-Poisson likelihoods $\mathcal{L}^{\mathrm{A,IC}}$, using the expression suggested by Baker Cousins in [102]

$$\mathcal{L}^{\mathrm{A,IC}} = \sum_i \left[n_i^{\mathrm{A,IC}} - N_i^{\mathrm{A,IC}} + n_i^{\mathrm{A,IC}} \ln \left(\frac{N_i^{\mathrm{A,IC}}}{n_i^{\mathrm{A,IC}}} \right) \right] \tag{6.4}$$

where the N_i is the expected number of events and n_i the observed number of neutrinos after the subtraction of the atmospheric background events in each energy bin i. According to the cuts considered by the two Collaborations, we consider only

neutrino events with $E_\nu \geq 20$ TeV for ANTARES and $E_\nu \geq 60$ TeV for IceCube. The expected number of events in the i-th energy bin $[E_i, E_{i+1}]$ is then given by

$$N_i^{\mathrm{A,IC}} = 4\pi \Delta t^{\mathrm{A,IC}} \int_{4\pi} d\Omega \int_{E_i}^{E_{i+1}} dE_\nu \frac{d\Phi}{dE_\nu d\Omega} A_{\mathrm{eff}}^{\mathrm{A,IC}}(E_\nu) \tag{6.5}$$

where $\Delta t^{\mathrm{A,IC}}$ is the exposure time ($\Delta t^{\mathrm{A}} = 2450$ days and $\Delta t^{\mathrm{IC}} = 2078$ days) and $A_{\mathrm{eff}}^{\mathrm{A,IC}}(E_\nu)$ is the effective area summed over the three neutrino flavors.
The ANTARES effective area for the nine year data sample [25], has been obtained by using the two cosmic neutrino spectra reported in fig. 6.1 and assuming a constant effective area in each energy bin. The IceCube effective area, instead, has been taken from [103]. The combined fit is obtained by considering the product of the two likelihoods:

$$\ln\left(\mathcal{L}(n_i^{\mathrm{IC}}, n_i^{\mathrm{A}} | \Phi^0_{astro}, \gamma_{astro})\right) = \ln\left(\mathcal{L}^{\mathrm{A}} \cdot \mathcal{L}^{\mathrm{IC}}\right) \tag{6.6}$$

where $\mathcal{L}$ is a function of the astrophysical flux normalization Φ^0_{astro} and of the spectral index γ_{astro}. The likelihood $\mathcal{L}$ is maximized giving the best values for the two free parameters. The best-fit values and the 1-2σ ranges of the flux normalization and the spectral index are obtained by maximizing the two dimensional likelihood and are reported in Tab. 6.1 . In case of the fit performed with IceCube data only, the best-fit values for the spectral index and the flux normalization differ from the ones reported by the IceCube Collaboration [91] only by 1% and 0.8%, respectively. It should be noted that the combined analysis provides slightly smaller values for the flux normalization Φ^0_{astro} and spectral index γ_{astro}. Fig. 6.2 shows the number of neutrino events in function of the energy for ANTARES and IceCube (upper and lower panel). In both the two panels the conventional atmospheric background is represented by the blue area and sum of the background and the combined best-fit power law is represented by the gray line. The shaded regions represent the lower cuts in energy considered in the fit. For ANTARES we consider an upper cut in energy ($E_\nu \leq 300$ TeV) according to [25], since the deduced ANTARES effective area is calculated only up to this energy.
Fig. 6.3 shows the contour plots for the fit of IceCube six-year HESE (black) and for the combined fit IceCube+ANTARES (orange). The solid lines correspond to the 68% confidence interval contours and the dotted ones show the 95% confidence interval contours.

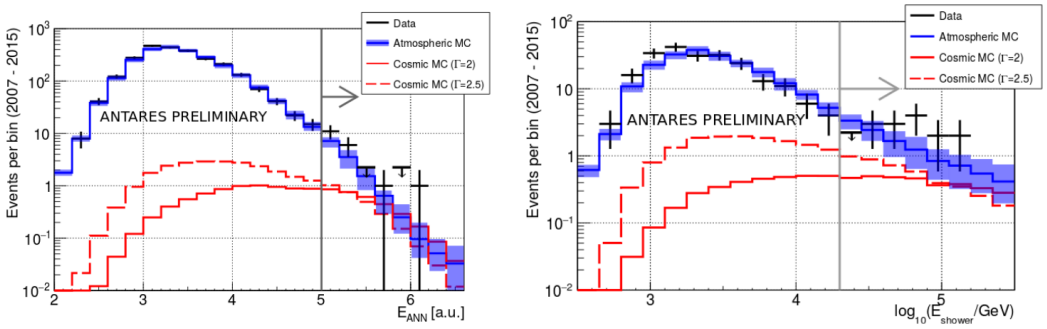

Fig. 6.1: ANTARES distribution of the energy estimator for data (black crosses) and Monte Carlo after the event selection cut, before applying the energy-related selection shown as an arrow. Left panel for tracks, right for showers. The blue histograms show atmospheric events, with uncertainties reported by the shaded band (see text for details). Red distributions are for cosmic fluxes with spectral index $\Gamma = 2\ 0$ (solid) or 2.5 (dashed). The normalization of the cosmic signal is assumed equal to the best fit from IceCube measurements [25].

Fit	Parameter	Best-fit	68% C.I.	95 % C.I.
IC	$\Phi^0_{\rm astro}$	2.44	2.00-2.94	1.62-3.48
	γ_{astro}	2.95	2.76-3.21	2.56- 3.46
IC+A	$\Phi^0_{\rm astro}$	2.30	1.90-2.71	1.56 3.16
	γ_{astro}	2.85	2.68-3.04	2.52-3.23

Tab. 6.1: Best-fit values and 1-2σ intervals of $\Phi^0_{\rm astro}$ (in units of 10^{-18} $(\mathrm{GeV cm^2 ssr})^{-1}$) and γ_{astro} for the analysis on IceCube six-year HESE data (IC) and the combined analysis IceCube+ANTARES (IC+A).

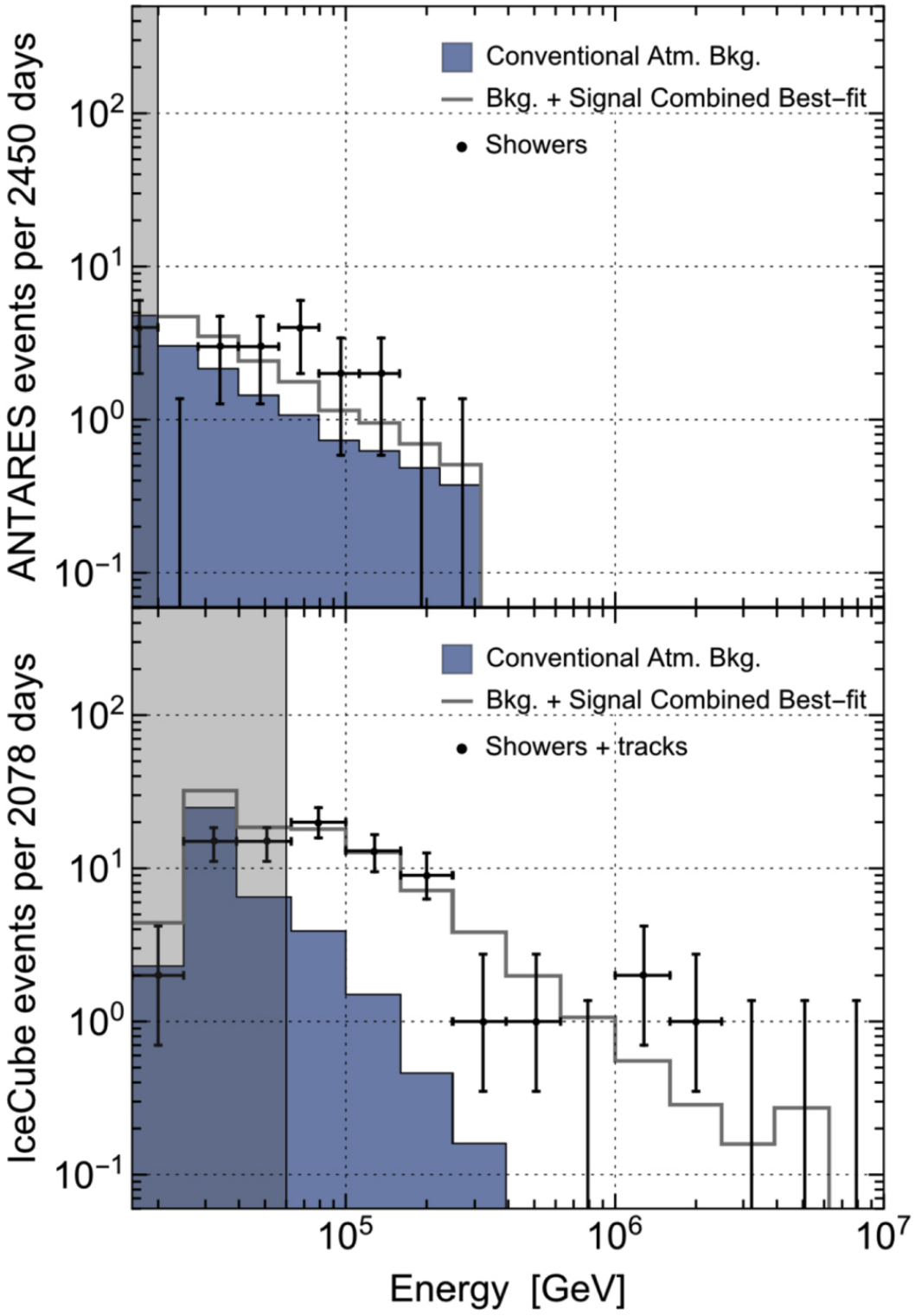

Fig. 6.2: Number of neutrino events as a function of the energy for ANTARES (upper panel) and IceCube (lower panel). In both plots, the blue area represents the conventional atmospheric background (neutrinos and penetrating muons), and the gray line corresponds to the sum of the background and the combined (IC+A) best-fit power-law with $\Phi^0_{\rm astro} = 2.30 \times 10^{-18}\ (\mathrm{GeV cm^2 s\ sr})^{-1}$ and $\gamma_{astro} = 2.85$ [92].

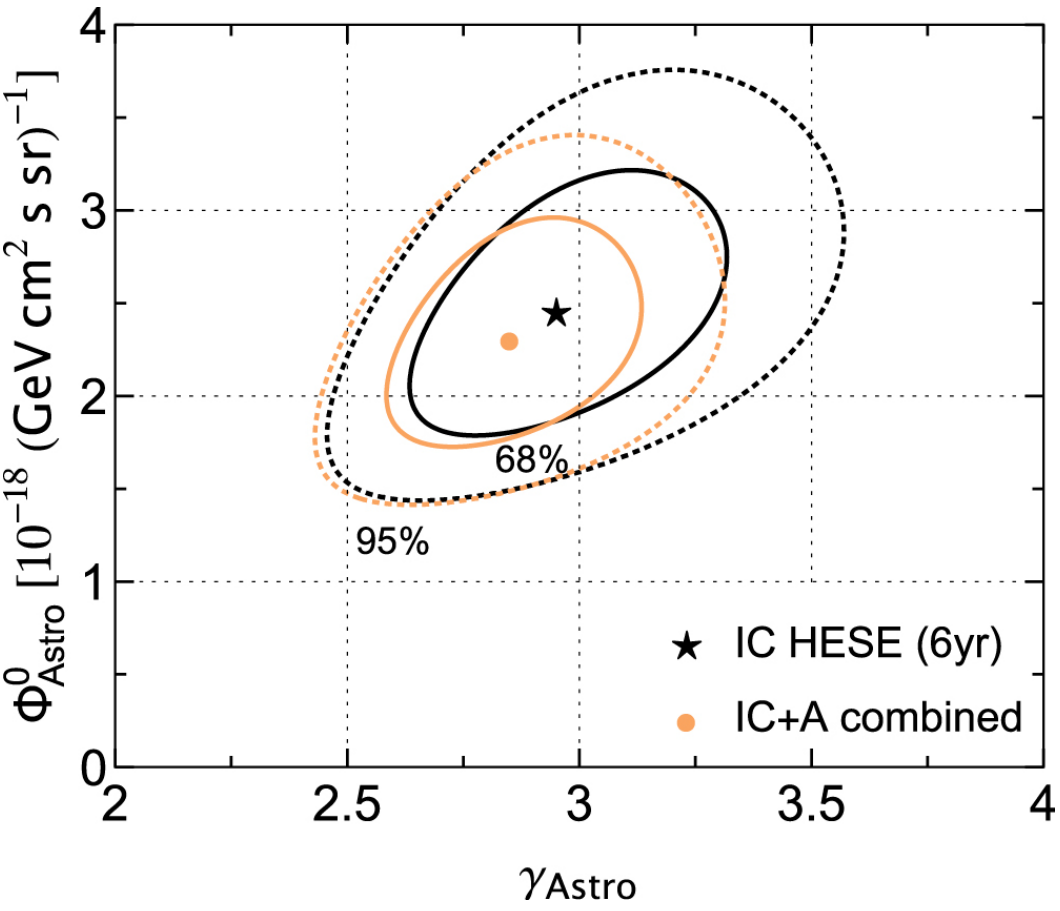

Fig. 6.3: Contour plot of the likelihood $\mathcal{L}(\Phi^0_{\rm astro}, \gamma_{\rm astro})$ in the case of the IceCube fit (black) and the combined IceCube+ANTARES one (orange). [92].

6.1.2 The Low-energy Excess

The second part of this analysis consist in fixing the spectral index is fixed to some specific values to underline the presence of possible excesses. Fig. 6.4 shows the residuals in the number of neutrino events for both experiments are after the subtraction of the sum of the conventional atmospheric background and of an astrophysical power-law $E_\nu^{-2.0}$. The flux normalization is fitted by considering both IceCube and ANTARES data. Both ANTARES and IceCube experiments seem to exhibit a slight excess in the same energy range (40-200 TeV) and the local significance of the low-energy excess in IceCube increases considering the six-year HESE data instead of four-year data reported in gray in Fig. 6.4 [104]. We have statistically tested the presence of an excess in both ANTARES and IceCube experiments choosing for the null hypothesis the one that in both samples the diffuse neutrino flux is just produced by an astrophysical power-law component superimposed to the conventional atmospheric background. In order to quantify the p-value for the null hypothesis, we

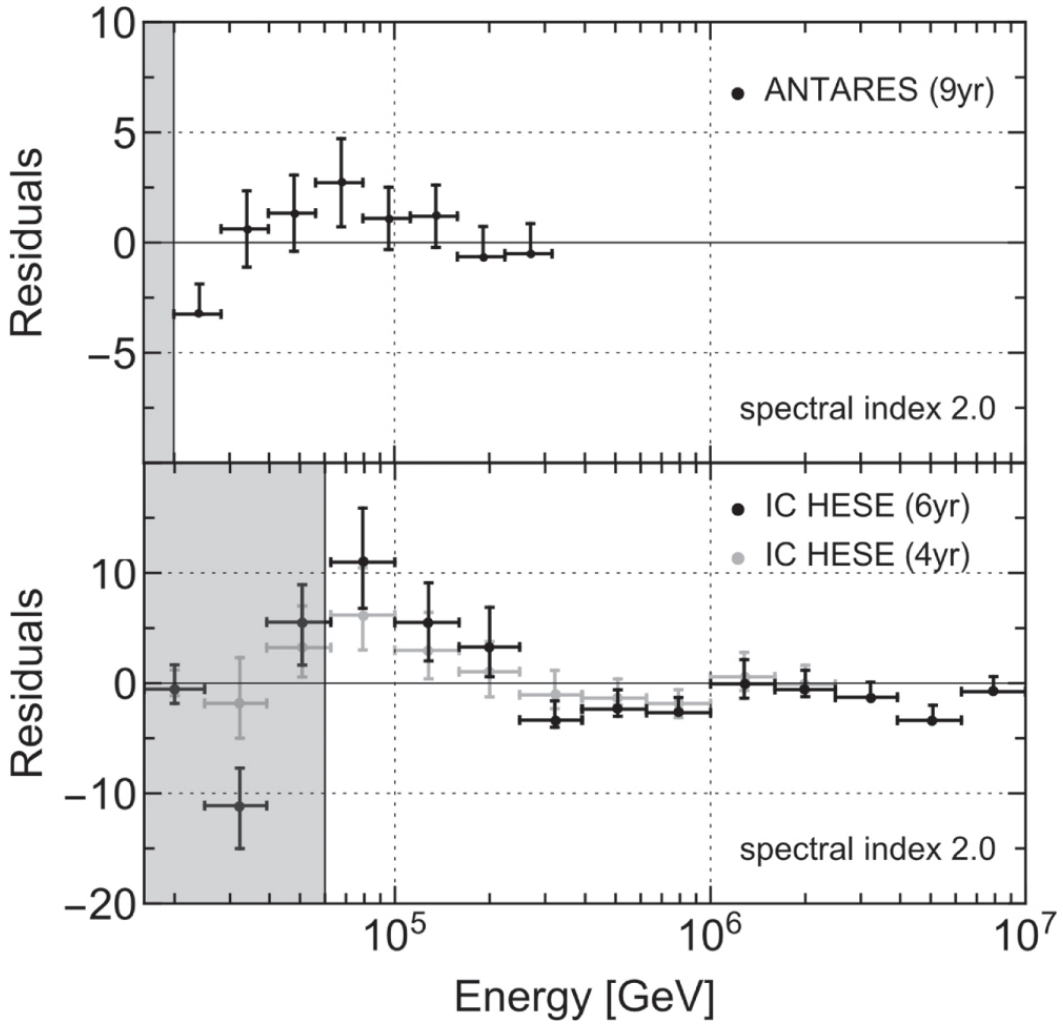

Fig. 6.4: Residuals in the number of neutrino events as a function of the neutrino energy with respect to the sum of the conventional atmospheric background and a single astrophysical power-law with spectral index 2.0 for ANTARES (upper panel) and IceCube (lower panel) [92].

perform a χ^2 test. The test statistics behaving as a χ^2 with N - m Degree Of Freedom (DOF), for Poisson-distributed data, is :

$$\chi^2 = -2 \ln \left(\mathcal{L}(n^{\mathrm{IC}}, n^{\mathrm{A}} | \Phi^0_{\mathrm{astro}}, \gamma_{\mathrm{astro}}) \right)$$

(6.7)

where $\mathcal{L}(n^{\mathrm{IC}}, n^{\mathrm{A}} | \Phi^0_{\mathrm{astro}}, \gamma_{\mathrm{astro}})$ is defined in eq. 6.4. The total number of energy bins in 18 and the number of free parameters in the fit is 1.
The test has been performed for different values of the spectral index γ_{astro}, while the flux normalization Φ^0_{astro} is obtained by maximizing the likelihood. Since the previous χ^2 analysis should be performed when the events of each bin are Gaussian distributed and this condition in principle could not be satisfied for small number of events, we additionally perform a more general non-parametric test, namely the one-dimensional Kolmogorov-Smirnov (KS) statistical test[105]. For each experiment, the KS test compares the empirical cumulative distribution function deduced by data with the one obtained under the null hypothesis of power-law behavior. For a given spectral index, the p-value is evaluated by a bootstrap method [106] for IceCube and ANTARES experiments, respectively. The two p-values are then combined by means of Fisher's method[107].
Fig. 6.5 shows the p-value for the χ^2 and KS hypothesis tests as a function of the spectral index adopted in the analysis. The bands in 6.5 are obtained by considering an uncertainty of $\pm 20\%$ on the conventional background estimation in both experiments. The plot clearly shows that the addition of the ANTARES data set to the IceCube one has the effect of reducing the p-value (by about a factor $2 \div 3$) independently of the assumed spectral index. This means that fixing a certain threshold in p-value for rejecting the null hypothesis, the addition of the ANTARES data set enlarges the range of spectral indices for which the null hypothesis is disfavored. The interpretation of the six-year up-going muon neutrinos as a single power-law with $\gamma = 2.13 \pm 0.13$ presented in [97] results statistically incompatible (p-value smaller than 10^{-2}) for the whole data sample. We underline that the benchmark prediction of Fermi acceleration mechanism $\gamma = 2.0$ has a p-value equal to $2.6^{+3.6}_{-1.8} \times 10^{-5}$ for χ^2 test and $1.6^{+2.1}_{-1.0} \times 10^{-6}$ for KS statistical test, where the errors correspond to a $\pm 20\%$ uncertainty on the conventional atmospheric background. This means that the theoretical prior of a single astrophysical power-law component with a spectral index that is dictated by Fermi acceleration mechanisms is more disfavored by the combined data sets with respect to the stand-alone IceCube sample. The results obtained show how the synergy among different Neutrino Telescopes

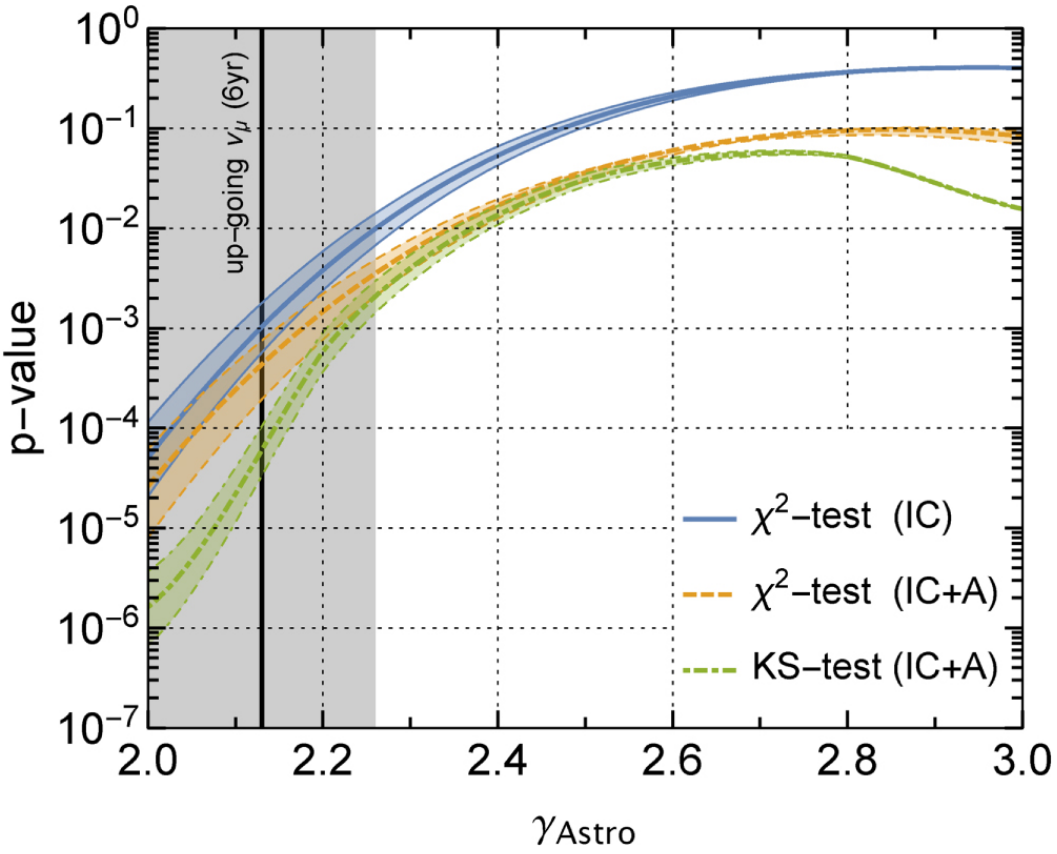

Fig. 6.5: The solid (dashed) line represents the p-value as a function of the spectral index for the χ^2-test for the IC (IC+A) data sample. The dotted-dashed line refers to the KS test performed by combining the two data samples with Fisher's method. The bands correspond to an uncertainty of $\pm 20\%$ on the conventional background estimation [92]. The vertical band, instead, represents the best-fit for the spectral index as deduced by six-year up-going muon neutrinos ($\gamma = 2.13 \pm 0.13$ [97].

(NTs) can improve and reinforce the results of a single experiment, and this will be even more true for future large NT KM3NeT[47].

6.2 Feasibility study for the indirect search of DM Matter with the KM3NeT Neutrino Telescope

6.2.1 The DM Matter Model

The results obtained in the previous analysis suggest a different interpretation of the data. In this analysis we suppose the presence of a two component neutrino flux:

$$\frac{d\Phi_{astro}}{dE_\nu d\Omega} = \Phi^0_{astro}\left(\frac{E_\nu}{100\ TeV}\right)^{-\gamma_{astro}} + \frac{d\Phi_{DM}}{dE_\nu d\Omega} \tag{6.8}$$

in which the first term is the same in 6.3 and the second one represents the presence of a neutrino DM flux. Neutrinos can be in fact produced by the decays of an unstable DM particle or by the pair-annihilation of stable DM particles. The DM differential neutrino flux of a given flavor α at the Earth is composed by two contributions:

$$\frac{d\Phi_{DM}}{dE_\nu d\Omega} = \sum_\beta P_{\alpha\beta}\left[\frac{d\Phi^G_\beta}{dE_\nu d\Omega} + \frac{d\Phi^{EG}_\beta}{dE_\nu d\Omega}\right] \tag{6.9}$$

where the first term expresses the Galactic contribution of the Milky Way and the second one represents the Extra Galactic (EG) component. Since the flavor ratio at the source depends on the particular Dark Matter model considered as well as on the energy, we take into account the neutrino flavor oscillations during the propagation, represented by the mixing probabilities $P_{\alpha\beta}$. For long baseline oscillations, the mixing probabilities are equal to:

$$\begin{aligned} P_{ee} &= 0.573, \quad P e\mu = 0.348, \quad P e\tau = 0.150 \\ \mathrm{P}_{\mu\mu} &= 0.348, \quad P\mu\tau = 0.375, \quad P\tau\tau = 0.475 \end{aligned} \tag{6.10}$$

where the values have been taken from [108]. In the following we will consider the case of decaying dark matter particles. The Galactic and the Extragalactic fluxes in eq. 6.9 can be expressed as:

$$\frac{d\Phi_\beta^G}{dE_\nu d\Omega} = \frac{1}{4\pi m_{DM}\tau_{DM}} \frac{dN_\beta}{dE_\nu} \int_0^\infty ds \rho_h \left[r(l,s,b)\right] \tag{6.11}$$

$$\frac{d\Phi_\beta^{EG}}{dE_\nu d\Omega} = \frac{\Omega_{DM}\rho_C}{4\pi m_{DM}\tau_{DM}} \int_0^\infty dz \frac{1}{H(z)} \frac{dN_\beta}{dE_\nu}\Big|_{E'=E(1+z)} \tag{6.12}$$

where, the quantities m_{DM} and τ_{DM} are the mass and the lifetime of DM particles, respectively. The Galactic (G) term (eq. 6.11) is proportional to the integral over the line-of-sight s of the galactic DM halo density $\rho_h(r)$ where $r = \sqrt{s^2 + R^2 - 2sR\cos l \cos b}$ with R = 8. 5 kpc and (*l*,b) are the Galactic coordinates. In the following, we consider for the DM halo density profile the Navarro-Frenk-White (NFW) distribution[109]

$$\rho_h^{NFW}(r) = \frac{\rho_s}{\frac{r}{r_s}\left(1+\frac{r}{r_s}^2\right)} \tag{6.13}$$

where r_s= 24.42 kpc and ρ_s = 0.184 GeV· cm^{-3}. The Extra Galactic (EG) flux (eq. 6.12) depends on the the critical energy density ρ_c = 5.5·10^{-6} GeV·cm^{-3} and on the Hubble expansion rate H (z) = $H_0\sqrt{\Omega_\Lambda + \Omega_m(1+z)^3}$ with Ω_{DM} = 0.2685, Ω_Λ = 0.6825 and Ω_m = 0.3175 according to Planck analysis[110]. The quantity $\frac{dN_\beta}{dE_\nu}$ is the energy spectrum of β neutrinos produced by DM particles. In the following we consider the particular case of a a bosonic DM particle χ decaying into a couple of τs:

$$\chi \rightarrow \tau^-\tau^+ \tag{6.14}$$

6.2.2 KM3NeT feasibility Study

The data taken by an high energy astronomy experiment consist of a set of events distributed throughout a region of the sky, and can be interpreted using two hypotheses:

- The data consist solely of background events, i. e. the null hypothesis (H_0);
- The data contains a signal from an external source, in our case neutrinos from DM decay (H_1).

The signal and background event distributions are governed by Probability Density Functions (PDFs), describing the event characteristics as angular distribution, reconstruction accuracy, time distribution, etc. Any difference between the signal and

background PDFs provides an opportunity to discriminate events produced by an astrophysical source from the background.
We will try to underline these differences through some quality cuts chosen with an accurate process optimized to maximize the ratio between the number of signal and background events.
In our analysis we consider as background the atmospheric neutrino events, the penetrating muons and a diffuse neutrino flux[47]:

$$\Phi(E_\nu) = 1.2 \cdot 10^{-8} \left(\frac{E_\nu}{GeV}\right)^{-2} e^{\left(\frac{-E_\nu}{3\ PeV}\right)}\ GeV^{-1}s^{-1}cm^{-2}sr^{-1} \tag{6.15}$$

6.2.3 Discovery Potential

The discovery potential[111] is determined from the number of detected events, n_α, in a given detector live time Δt that has a probability α or less to originate purely from background in 1-β = 50% of all the hypothetical experiments. If α = 2.85·10^{-7} (1.35·10^{-3}) the observation of n_α would correspond to a significance of 5σ (3σ) with a confidence level (CL) of 50%. To calculate nα we have to extract from simulation the average number of background events $\langle n_b \rangle$ in Δt and determinate the minimum number of events, n_0, that satisfies:

$$\sum_{n_{obs} \equiv n_0}^{\infty} P(n_{obs} | \langle n_n \rangle) < \alpha \tag{6.16}$$

where $P(n_{obs} | \langle n_b \rangle)$ is the Poisson probability for observing n_{obs} events given an expected number of background events $\langle\ n_b \rangle$. The value n_0 is the minimum number of events we have to detect to claim a deviation from the background-only hypothesis with a statistical significance defined by α. If we indicate with $\langle\ n_s \rangle$ the average number of signal events, it follows that $n_0 = \langle n_b \rangle + \langle n_s \rangle$ and the n_α that leads to an observation with a p-value less than α in a fraction 1 -β of the experiments is the the one that fulfills:

$$P_{5\sigma} = \sum_{n_{obs} \equiv n_0}^{\infty} P(n_{obs} | \langle n_n \rangle + n_\alpha) = 1 - \beta \tag{6.17}$$

If the given source spectrum Φ_s predicts $\langle\ n_b \rangle$signal events in the time window Δt, the flux Φ_α needed for a discovery (discovery flux) is given by:

$$\Phi_\alpha = \Phi_s \cdot \frac{n_\alpha(\langle n_b \rangle)}{\langle n_s \rangle} \tag{6.18}$$

where the ratio $\frac{n_\alpha(\langle n_b \rangle)}{\langle n_s \rangle}$ is referred as Model Discovery Potential (MDP). In our Dark Matter Sensitivity study the MDP, and so the discovery flux, is minimized applying cuts on the number of hits used during the reconstruction N_{hit}, on the quality fit

parameter Lik_{red}, on the uncertainty on the direction of the reconstructed track β and on the reconstructed track angle.
The number of years required to claim the discovery of a given source can be calculated finding the observation time Δt necessary to reach the condition $\Phi_\alpha = \Phi_s$ or equivalently $n_\alpha(\langle n_b \rangle) = \langle n_s \rangle$.

6.2.4 Results

For this study we have to consider an accurate simulation of background and signal events. At this scope the background of atmospheric ν_μ and $\bar{\nu}_\mu$ is simulated in the energy range 10^2-10^8 GeV and over the full solid angle. The events are then weighted to reproduce the conventional atmospheric neutrino flux following the Bartol model [112] and a prompt contribution [113]. The atmospheric muons have been simulated only for the reference detector trough the MUPAGE code (see sec. 4.2.3). This production consists in a sample with 1 TeV $\leq$ E_b $<$ 10 TeV, where E_b is the sum of energies of all single muons in a bundle. To increase statistics in the high-energy region, an additional sample has been generated with $E_b \geq$ 10 TeV. The events have been reweighted to obtain the expected number of events in one year of data taking. The signal events are obtained generating all flavor ν and $\bar{\nu}$ in the energy range 10^2-10^8 GeV and over the full solid angle and then reweighted considering the dark matter flux in 6.9.
Fig. 6.6 shows the number of expected DM neutrino in function of the dark matter particle decaying mass m_{DM} and its lifetime τ_{DM}. In the following we present the results obtained for the particular case of m_{DM}= 130 TeV and τ_{DM}=10^{26}s for which a number $n_{no-cut} \approx 10^8$ is expected in one year of data taking of the KM3NeT telescope for only one ARCAblock of 115 strings. In tab. 6.2 are specified the cut obtained from the minimization of the MDP while tab. 6.3 reports the numbers of signal n_s and background (atmospheric neutrinos and astrophysics neutrinos and atmospheric muons) n_b obtained after the application of each cut. Finally Fig. 6.7 shows how many years are needed for one block of the KM3NeT neutrino telescope to reach the sensitivity of 5σ and 3σ. The results of our analysis are encouraging since they demonstrate that one block of the KM3NeT could claim the discover of a DM decay neutrino signal with the flux in eq. 6.9 in only 18 years and reaching the sensitivity of 3 σ in less than 7 years of data taking.

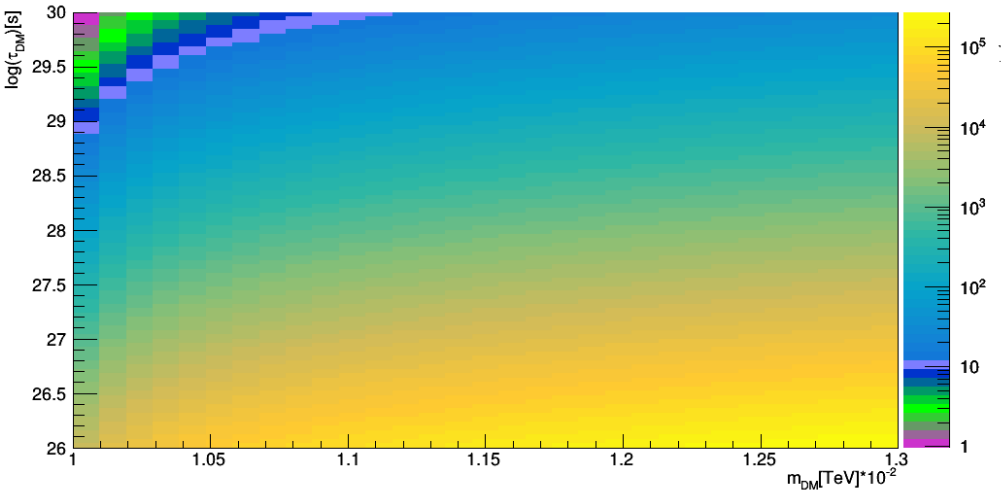

Fig. 6.6: Distribution of the number of expected neutrino dark matter events, re-scaled for 10^{-3} in function of the decaying DM particle mass and lifetime.

Parameter	Cut
Θ	$\leq 107°$
Lik_{red}	$\geq$-0.7
β	$\leq$0.05
N_{hit}	$\geq$250

Tab. 6.2: Values of the cuts obtained minimizing the Model Discovery Potential.

Parameter Cut	n_s	n_b
Θ	416	452689
Lik_{red}	410	371204
β	410	366755
N_{hit}	260	495

Tab. 6.3: Number of signal and background events obtained after the application of the optimized cuts.

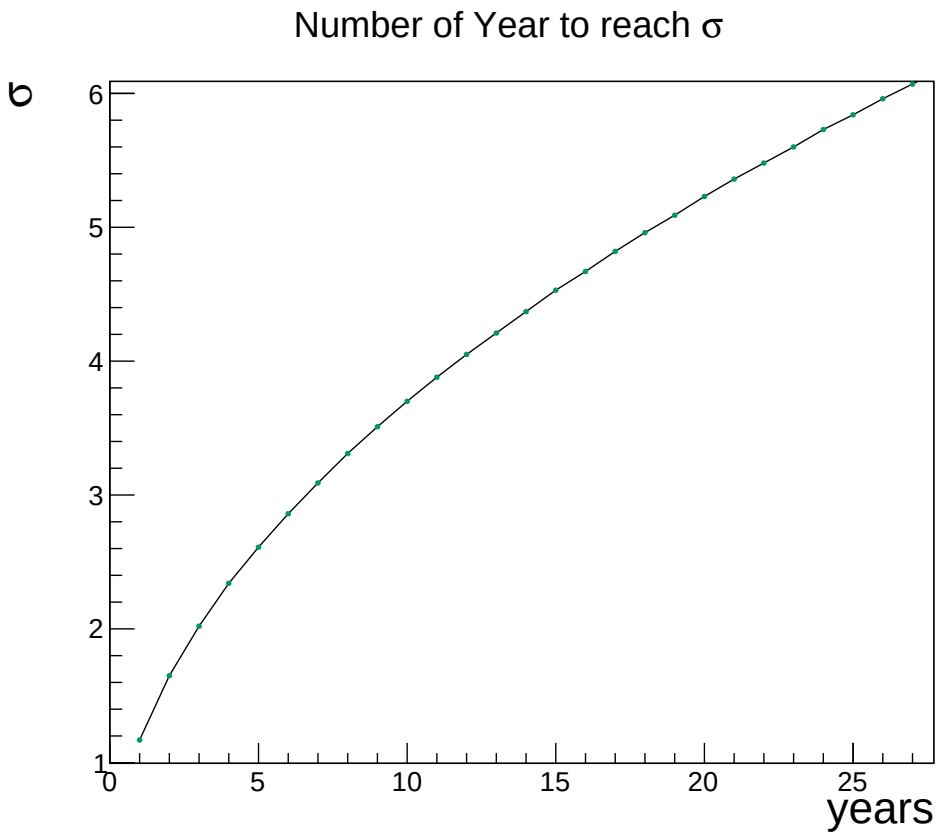

Fig. 6.7: Number of σ reached by with one block of KM3NeT ARCA in function of the number of years needed.

Conclusions

KM3NeT is the next-generation neutrino telescope whose installation, in the depths of the Mediterranean Sea, began three years ago exploiting the experience of the ANTARES submarine telescope. At present the larger neutrino telescope in the world is IceCube, installed in Antartica that has recently reported evidence of a flux of cosmic high energy neutrinos exceeding the expected flux of atmospheric neutrinos. This excess has ap-value of 0.15 with a significance beneath 2σ [25].
The analysis on these data provides a best-fit power-law with spectral index equal to $2.92^{+0.29}_{-0.33}$ so the interpretation of this neutrino flux as a single power-law with spectral index ~ 2.0 results statistically incompatible (p-value smaller than 10^{-2}) especially if the Icecube data are combined with the ANTARES once. This evidence suggests the presence of an exotic component that can be identified thanks to the construction of the new generation KM3NeT telescope.
KM3NeT is based on a novel type of optical sensor, the Digital Optical Module, realized using a multi-photomultipliers approach that allows better performances with respect to the standard single large-area photomultipliers used in ANTARES and IceCube, since photon counting and in particular the direction reconstruction are possible better due to photocatode segmentation.
The important role of the PMTs for the correct working of KM3NeT telescope makes it essential a study aimed at the complete characterization of these devices. The full characterization of about 7000 PMTs has been one of the achievements of this thesis. The profile of the "typical" photomultiplier has been very useful as input for the simulations of the PMTs response.
The correct simulation of the neutrino interactions is essential to explore the possibility of searching for neutrinos generated by Dark Matter particles decay through KM3NeT neutrino telescope. For this reason one of the aims of this work has been the introduction, in the simulation code GENHEN used by the ANTARES and KM3NeT Collaborations, of the process of regeneration of the tauonic neutrino. The introduction of the "regeneration process" allows the correction of the estimation of expected neutrinos number. The introduction of this effect has resulted in an increase of about 10% for energies of the expected events from 10^6 to 10^8 GeV. This gain becomes more important for particles with a zenith angle from 0 to 10° reaching

the 30% for muonic neutrinos and the 100% for electronic neutrinos produced in the regeneration chain.
Encouraged by the results of the combined Icecube-ANTARES analysis and confident of the performance of the PMTs and of the KM3NeT telescope simulation code, we carried out a feasibility study for the indirect research of Dark Matter. This analysis led us to conclude that with only two blocks, composed of 115 detector units, it is possible claim the discovery of a Dark Matter decay neutrino signal in only 9 years and reach the sensitivity of 3σ in less than 4 years of data taking.
The search for Dark Matter could also receive a significant boost due to the real perspective on increasing the sensitive volume and therefore the sensitivity of the Icecube (IceCube-Gen2) and KM3NeT telescopes.

Bibliography

[1] V.F. Hess. „Observations in low level radiation during seven free balloon flights“. In: *Phys. Zeit.* 13 (1912), pp. 1084–1901 (cit. on p. 5).

[2] Bruno Rossi. „On the Magnetic Deflection of Cosmic Rays“. In: *Phys. Rev.* 36 (3 1930), pp. 606–606 (cit. on p. 5).

[3] T. K. Gaisser, F. Halzen, and T. Stanev. „Particle astrophysics with high energy neutrinos“. In: *Physics Reports* 258.3 (1995), pp. 173 –236 (cit. on p. 5).

[4] Jorg R. Horandel. „The Composition of Cosmic Rays at the Knee“. In: (2012). [AIP Conf. Proc.1516,185(2012)]. arXiv: 1212.0739 [astro-ph.HE] (cit. on p. 5).

[5] Anthony M. Hillas. „Cosmic Rays: Recent Progress and some Current Questions“. In: *Conference on Cosmology, Galaxy Formation and Astro-Particle Physics on the Pathway to the SKA Oxford, England, April 10-12, 2006*. 2006. arXiv: astro-ph/0607109 [astro-ph] (cit. on p. 6).

[6] Jorg R. Horandel. „Models of the knee in the energy spectrum of cosmic rays“. In: *Astroparticle Physics* 21.3 (2004), pp. 241 –265 (cit. on p. 7).

[7] R. Aloisio, V. Berezinsky, and A. Gazizov. „Transition from galactic to extragalactic cosmic rays“. In: *Astroparticle Physics* 39-40 (2012). Cosmic Rays Topical Issue, pp. 129 –143 (cit. on p. 7).

[8] Kenneth Greisen. „End to the Cosmic-Ray Spectrum?“ In: *Phys. Rev. Lett.* 16 (17 1966), pp. 748–750 (cit. on p. 7).

[9] G. T. Zatsepin and V. A. Kuzmin. „Upper limiractt of the spectrum of cosmic rays“. In: *JETP Lett.* 4 (1966). [Pisma Zh. Eksp. Teor. Fiz.4,114(1966)], pp. 78–80 (cit. on p. 7).

[10] ENRICO Fermi. „On the Origin of the Cosmic Radiation“. In: *Phys. Rev.* 75 (8 1949), pp. 1169–1174 (cit. on pp. 7, 82).

[11] E. Fermi. „Galactic Magnetic Fields and the Origin of Cosmic Radiation.“ In: *Astrophys. J.* 119 (1954), pp. 1–6 (cit. on p. 7).

[12] Federico Fraschetti. „On the acceleration of ultra-high-energy cosmic rays“. In: *Philosophical Transactions of the Royal Society of London A: Mathematical, Physical and Engineering Sciences* 366.1884 (2008), pp. 4417–4428. eprint: http://rsta.royalsocietypublishing.org/content/366/1884/4417.full.pdf (cit. on p. 16).

[13] Meng Su, Tracy R. Slatyer, and Douglas P. Finkbeiner. „Giant Gamma-ray Bubbles from Fermi-LAT: AGN Activity or Bipolar Galactic Wind?“ In: *Astrophys. J.* 724 (2010), pp. 1044–1082. arXiv: 1005.5480 [astro-ph.HE] (cit. on p. 8).

[14] Roland M. Crocker and Felix Aharonian. „Fermi Bubbles: Giant, Multibillion-Year-Old Reservoirs of Galactic Center Cosmic Rays“. In: *Phys. Rev. Lett.* 106 (10 2011), p. 101102 (cit. on p. 8).

[15] Wim de Boer, Iris Gebauer, Simon Kunz, and Alexander Neumann. „Evidence for a hadronic origin of the Fermi Bubbles and the Galactic Excess“. In: (2015). arXiv: 1509.05310 [astro-ph.HE] (cit. on p. 8).

[16] K.-S. Cheng, D. O. Chernyshov, V. A. Dogiel, and C.-M. Ko. „Multi-wavelength Emission from the Fermi Bubble. II. Secondary Electrons and the Hadronic Model of the Bubble“. In: *The Astrophysical Journal* 799.1 (2015), p. 112 (cit. on p. 8).

[17] Marco Tavani, Andrea Bulgarelli, G Piano, et al. „Extreme particle acceleration in the microquasar Cygnus X-3“. In: *Nature* 462 (Nov. 2009), pp. 620–3 (cit. on p. 9).

[18] P. Abreu, M. Aglietta, E.J. Ahn, et al. „Update on the correlation of the highest energy cosmic rays with nearby extragalactic matter“. In: *Astroparticle Physics* 34.5 (2010), pp. 314 –326 (cit. on p. 9).

[19] In: () (cit. on p. 9).

[20] G. Cavallo and M. J. Rees. „A qualitative study of cosmic fireballs and Îş-ray bursts“. In: *Monthly Notices of the Royal Astronomical Society* 183.3 (1978), pp. 359–365. eprint: /oup/backfile/content_public/journal/mnras/183/3/10.1093/mnras/183.3.359/2/mnras183-0359.pdf (cit. on p. 9).

[21] John David Jackson. *Classical electrodynamics*. 3rd ed. New York, NY: Wiley, 1999 (cit. on pp. 10, 23).

[22] A. A. Abdo, M. Ackermann, M. Ajello, et al. „Gamma-Ray Emission from the Shell of Supernova Remnant W44 Revealed by the Fermi LAT“. In: *Science* 327.5969 (2010), pp. 1103–1106. eprint: http://science.sciencemag.org/content/327/5969/1103.full.pdf (cit. on pp. 10, 18).

[23] M Ackermann, M Ajello, W B. Atwood, et al. „Fermi-LAT Observations of the Diffuse Gamma-Ray Emission: Implications for Cosmic Rays and the Interstellar Medium“. In: *The Astrophysical Journal* 750 (Apr. 2012), p. 3 (cit. on pp. 10, 19).

[24] Yi-Qing Guo, Hong-Bo Hu, and Zhen Tian. „On the contribution of a hard galactic plane component to the excesses of secondary particles“. In: *Chinese Physics C* 40.11 (2016), p. 115001 (cit. on pp. 10, 19).

[25] Thomas Eberl, Sergio Navas, Federico Versari, and Luigi Antonio Fusco. „Search for a diffuse flux of cosmic neutrinos with the ANTARES telescope“. In: *PoS* ICRC2017 (2018), p. 993 (cit. on pp. 11, 81–84, 97).

[26] Torbjorn Sjostrand, Leif Lonnblad, and Stephen Mrenna. „PYTHIA 6.2: Physics and manual“. In: (2001). arXiv: hep-ph/0108264 [hep-ph] (cit. on p. 12).

[27] R. S. Fletcher, T. K. Gaisser, Paolo Lipari, and Todor Stanev. „SIBYLL: An Event generator for simulation of high-energy cosmic ray cascades“. In: *Phys. Rev.* D50 (1994), pp. 5710–5731 (cit. on p. 12).

[28] N.N. Kalmykov, S.S. Ostapchenko, and A.I. Pavlov. „Quark-gluon-string model and EAS simulation problems at ultra-high energies“. In: *Nuclear Physics B - Proceedings Supplements* 52.3 (1997), pp. 17 –28 (cit. on p. 12).

[29] P. Lipari. „Lepton spectra in the earth's atmosphere“. In: *Astropart. Phys.* 1 (1993), pp. 195–227 (cit. on p. 13).

[30] B. Pontecorvo. „Inverse beta processes and nonconservation of lepton charge“. In: *Sov. Phys. JETP* 7 (1958). [Zh. Eksp. Teor. Fiz.34,247(1957)], pp. 172–173 (cit. on p. 21).

[31] Ziro Maki, Masami Nakagawa, and Shoichi Sakata. „Remarks on the unified model of elementary particles“. In: *Prog. Theor. Phys.* 28 (1962). [,34(1962)], pp. 870–880 (cit. on p. 21).

[32] S.M. Bilenky and B. Pontecorvo. „Lepton mixing and neutrino oscillations“. In: *Physics Reports* 41.4 (1978), pp. 225 –261 (cit. on p. 21).

[33] M C. Gonzalez-Garcia, Michele Maltoni, and Thomas Schwetz-Mangold. „Updated fit to three neutrino mixing: status of leptonic CP violation“. In: *Journal of High Energy Physics* 2014 (Sept. 2014) (cit. on p. 22).

[34] J. Pumplin, D. R. Stump, J. Huston, et al. „New generation of parton distributions with uncertainties from global QCD analysis“. In: *JHEP* 07 (2002), p. 012. arXiv: hep-ph/0201195 [hep-ph] (cit. on p. 22).

[35] S. X. Nakamura, K. Sumiyoshi, and T. Sato. „Neutrino deuteron reaction in the heating mechanism of core-collapse supernovae“. In: *Phys. Rev.* C80 (2009), p. 035802. arXiv: 0906.0856 [nucl-th] (cit. on p. 23).

[36] Tommaso Chiarusi and M Spurio. „High-Energy Astrophysics with Neutrino Telescopes“. In: *European Physical Journal C* 65 (June 2009) (cit. on p. 24).

[37] Paolo Lipari and Todor Stanev. „Propagation of multi-TeV muons“. In: *Phys. Rev. D* 44 (11 1991), pp. 3543–3554 (cit. on pp. 25, 52, 54).

[38] M.A. Markov. „Propagation of multi-TeV muons“. In: *Proceedings Int. Conf. on High Energy Physics* (1960), p. 183 (cit. on p. 26).

[39] Gustav Mie. „Beitrage zur Optik truber Medien, speziell kolloidaler Metallosungen“. In: *Annalen der Physik* 330.3 (1908), pp. 377–445. eprint: https://onlinelibrary.wiley.com/doi/pdf/10.1002/andp.19083300302 (cit. on p. 27).

[40] University of Hawaii. *DUMAND at the University of Hawaii*. URL: https://www.phys.hawaii.edu/~dumand/ (visited on Nov. 3, 2018) (cit. on p. 28).

[41] I. A. Belolaptikov, L. B. Bezrukov, B. A. Borisovets, et al. „The Baikal underwater neutrino telescope: Design, performance, and first results“. English. In: *Astroparticle Physics* 7.3 (Jan. 1997), pp. 263–282 (cit. on p. 28).

[42] V. Aynutdinov, V. Balkanov, I. Belolaptikov, et al. „Search for a diffuse flux of high-energy extraterrestrial neutrinos with the NT200 neutrino telescope“. In: *Astroparticle Physics* 25.2 (2006), pp. 140 –150 (cit. on p. 28).

[43] Alrxander Avrorin, Vladimir Aynutdinov, Igor Belolaptikov, et al. „An experimental string of the NT1000 Baikal neutrino telescope“. In: *Instruments and Experimental Techniques* 54 (Sept. 2011), pp. 649–659 (cit. on p. 28).

[44] A Margiotta. „Status of the KM3NeT project“. In: *Journal of Instrumentation* 9.04 (2014), p. C04020 (cit. on p. 29).

[45] The ANTARES Collaboration. *Astronomy with a Neutrino Telescope and Abyss environmental RESearch*. URL: http://antares.in2p3.fr/ (visited on Nov. 3, 2018) (cit. on pp. 28, 33).

[46] T. Feder. „Deep-Sea Km^3 Neutrino Detector Gets Thumbs Up “. In: *Physics Today* 55.10 (2002), p. 20 (cit. on p. 28).

[47] S. Adrian-Martinez et al. „Letter of intent for KM3NeT 2.0“. In: *J. Phys.* G43.8 (2016), p. 084001. arXiv: 1601.07459 [astro-ph.IM] (cit. on pp. 28, 40, 43, 44, 50, 71, 73, 90, 92).

[48] F. Halzen. „Astroparticle physics with the AMANDA neutrino telescope“. In: *Eur. Phys. J. C* 46 (2006), p. 669 (cit. on p. 29).

[49] *Proceedings of the 31st ICRC,* Lodz, Poland, 2009 (cit. on p. 29).

[50] M.G. Aartsen, R. Abbasi, Y. Abdou, et al. „Measurement of South Pole ice transparency with the IceCube LED calibration system“. In: *Nuclear Instruments and Methods in Physics Research Section A: Accelerators, Spectrometers, Detectors and Associated Equipment* 711 (2013), pp. 73 –89 (cit. on pp. 30, 31).

[51] T. Montaruli. „Status report of the ANTARES project“. In: *Nuclear Physics B - Proceedings Supplements* 110 (2002), pp. 513 –515 (cit. on p. 33).

[52] M. Ageron, J.A. Aguilar, A. Albert, et al. „Performance of the first ANTARES detector line“. In: *Astroparticle Physics* 31.4 (2009), pp. 277 –283 (cit. on p. 33).

[53] P Amram, M Anghinolfi, S Anvar, et al. „The ANTARES optical module“. In: *Nuclear Instruments and Methods in Physics Research Section A: Accelerators, Spectrometers, Detectors and Associated Equipment* 484.1 (2002), pp. 369 –383 (cit. on p. 33).

[54] J.A. Aguilar, A. Albert, F. Ameli, et al. „Study of large hemispherical photomultiplier tubes for the ANTARES neutrino telescope“. In: *Nuclear Instruments and Methods in Physics Research Section A: Accelerators, Spectrometers, Detectors and Associated Equipment* 555.1 (2005), pp. 132 –141 (cit. on p. 33).

[55] J.A. Aguilar, A. Albert, F. Ameli, et al. „The data acquisition system for the ANTARES neutrino telescope“. In: *Nuclear Instruments and Methods in Physics Research Section A: Accelerators, Spectrometers, Detectors and Associated Equipment* 570.1 (2007), pp. 107 –116 (cit. on pp. 33, 35, 36, 38, 40).

[56] J.A. Aguilar, A. Albert, P. Amram, et al. „Transmission of light in deep sea water at the site of the Antares neutrino telescope“. In: *Astroparticle Physics* 23.1 (2005), pp. 131 –155 (cit. on p. 33).

[57] Luigi Antonio Fusco. „Search for a diffuse neutrino emission in the Southern Sky with the ANTARES telescope“. PhD Thesis. Alma Mater Studiorum-Universitá diBologna, 2016 (cit. on p. 35).

[58] P Amram, M Anghinolfi, S Anvar, et al. „Sedimentation and fouling of optical surfaces at the ANTARES site“. In: *Astroparticle Physics* 19.2 (2003), pp. 253 –267 (cit. on pp. 36, 37).

[59] Marco Circella. „Time calibration of the NEutrino Mediterranean Observatory (NEMO)“. In: *Nuclear Instruments and Methods in Physics Research Section A: Accelerators, Spectrometers, Detectors and Associated Equipment* 602.1 (2009). Proceedings of the 3rd International Workshop on a Very Large Volume Neutrino Telescope for the Mediterranean Sea, pp. 187 –189 (cit. on p. 38).

[60] P. Bagley et al. „KM3NeT: Technical Design Report for a Deep-Sea Research Infrastructure in the Mediterranean Sea Incorporating a Very Large Volume Neutrino Telescope“. In: (2009) (cit. on p. 40).

[61] Marco Circella. „The Digital Optical Module -DOM- of the KM3NeT detector“. In: *Proceedings, 33rd International Cosmic Ray Conference (ICRC2013): Rio de Janeiro, Brazil, July 2-9, 2013*, p. 1223 (cit. on p. 40).

[62] The KM3NeT collaboration. „Expansion cone for the 3-inch PMTs of the KM3NeT optical modules“. In: *Journal of Instrumentation* 8.03 (2013), T03006 (cit. on pp. 41, 42).

[63] J. P. Yanez and A. Kouchner. „Measurement of atmospheric neutrino oscillations with very large volume neutrino telescopes“. In: *Adv. High Energy Phys.* 2015 (2015), p. 271968. arXiv: 1509.08404 [hep-ex] (cit. on p. 47).

[64] S. Adrián-Martínez, M. Ageron, F. Aharonian, et al. „The prototype detection unit of the KM3NeT detector“. In: *The European Physical Journal C* 76.2 (2016), p. 54 (cit. on pp. 43, 45, 48).

[65] S. Adrián-Martínez, M. Ageron, F. Aharonian, et al. „Deep sea tests of a prototype of the KM3NeT digital optical module“. In: *The European Physical Journal C* 74.9 (2014), p. 3056 (cit. on pp. 48, 49).

[66] Simone Biagi, Tommaso Chiarusi, Paolo Piattelli, and Diego Real. „The data acquisition system of the KM3NeT detector“. In: *PoS* ICRC2015 (2016), p. 1172 (cit. on p. 45).

[67] G. Riccobene and A. Capone. „Deep seawater inherent optical properties in the Southern Ionian Sea“. In: *Astropart. Phys.* 27 (2007), pp. 1–9. arXiv: astro-ph/0603701 [astro-ph] (cit. on p. 51).

[68] D. Bailey. „Monte Carlo tools and analysis methods for under- standing the ANTARES experiment and predicting its sensitivity to Dark Matter“. PhD Thesis. Wolfson College, Oxford, 2002 (cit. on pp. 51, 61).

[69] G Ingelman, A Edin, and J Rathsman. „LEPTO 6.5 - A Monte Carlo generator for deep inelastic lepton-nucleon scattering“. In: *Computer Physics Communications* 101.1 (1997), pp. 108 –134 (cit. on p. 52).

[70] Giles David. Barr. „The separation of signals and background in a nucleon decay experiment“. PhD thesis. University of Oxford, 1987 (cit. on p. 52).

[71] P. Antonioli, C. Ghetti, E. V. Korolkova, V. A. Kudryavtsev, and G. Sartorelli. „A Three-dimensional code for muon propagation through the rock: Music“. In: *Astropart. Phys.* 7 (1997), pp. 357–368. arXiv: hep-ph/9705408 [hep-ph] (cit. on p. 52).

[72] Igor A. Sokalski, Edgar V. Bugaev, and Sergey I. Klimushin. „MUM: Flexible precise Monte Carlo algorithm for muon propagation through thick layers of matter“. In: *Phys. Rev. D* 64 (7 2001), p. 074015 (cit. on p. 52).

[73] B.K. Lubsandorzhiev, R.V. Vasiliev, Y.E. Vyatchin, and B.A.J. Shaibonov. „Photoelectron backscattering in vacuum phototubes“. In: *Nuclear Instruments and Methods in Physics Research Section A: Accelerators, Spectrometers, Detectors and Associated Equipment* 567.1 (2006). Proceedings of the 4th International Conference on New Developments in Photodetection, pp. 12 –16 (cit. on p. 54).

[74] F.C. Brunner. *ANTARES Internal note*. ANTARES-Soft/2000-008. 2000 (cit. on p. 55).

[75] K. Hagiwara, K. Hikasa, K. Nakamura, et al. „Review of Particle Properties“. In: *Phys. Rev. D* 66 (1 2002), p. 010001 (cit. on pp. 55, 62).

[76] T.Montaruli A.L'Abbate and I. Sokalsky. *ANTARES Internal note*. ANTARES-Soft/2004-010. 2004 (cit. on p. 56).

[77] R.Mele O.Pisanti. *Update on τ regeneration in GenHen*. Talk at NTARES and KM3NeT Collaboration Meeting, Rabat. Feb. 2018 (cit. on p. 63).

[78] URL: http://www-ik.fzk.de/corsika/ (visited on Nov. 3, 2018) (cit. on p. 56).

[79] Y. Becherini, A. Margiotta, M. Sioli, and M. Spurio. „A Parameterisation of single and multiple muons in the deep water or ice“. In: *Astropart. Phys.* 25 (2006), pp. 1–13. arXiv: hep-ph/0507228 [hep-ph] (cit. on p. 56).

[80] A. Margiotta. *ANTARES Internal note*. ANTARES-Soft/2004-002. 2002 (cit. on p. 56).

[81] E V Bugaev, T Montaruli, Y Shlepin, and I A Sokalski. *Propagation of Tau Neutrinos and Tau Leptons through the Earth and their Detection in Underwater/Ice Neutrino Telescopes*. Tech. rep. hep-ph/0312295. Comments: 29 pages, 14 figures, uses elsart.cls, elsart.sty, elsart12.sty, accepted by Astroparticle Physycs on March 20th, 2004. Bari: Bari Univ. INFN, 2003 (cit. on p. 56).

[82] L. T. S.Navas. *ANTARES Internal note*. ANTARES-Soft/1999-011. 1999 (cit. on p. 57).

[83] C.M. Mollo, C. Bozza, T. Chiarusi, et al. „A new instrument for high statistics measurement of photomultiplier characteristics“. In: *Journal of Instrumentation* 11.08 (2016), T08002 (cit. on pp. 65–68).

[84] D. Rwal. „KM3NeT Digital Optical Module Electronics“. In: *Proceedings of the VLVNT2015 Conference Eur. Phys. J. Conf. 116 05007*. 2015 (cit. on p. 69).

[85] S. Aiello, S.E. Akrame, F. Ameli, et al. „Characterisation of the Hamamatsu photomultipliers for the KM3NeT Neutrino Telescope“. In: *Journal of Instrumentation* 13.05 (2018), P05035 (cit. on pp. 71–79).

[86] P Timmer, E Heine, and H Peek. „Very low power, high voltage base for a Photo Multiplier Tube for the KM3NeT deep sea neutrino telescope“. In: *Journal of Instrumentation* 5.12 (2010), p. C12049 (cit. on p. 70).

[87] B. Herold, O. Kalekin, and J. Reubelt. „PMT characterisation for the KM3NeT project“. In: *Nuclear Instruments and Methods in Physics Research Section A: Accelerators, Spectrometers, Detectors and Associated Equipment* 639.1 (2011). Proceedings of the Seventh International Workshop on Ring Imaging Cherenkov Detectors, pp. 70 –72 (cit. on p. 73).

[88] S. Adrián-Martínez, M. Ageron, S. Aiello, et al. „A method to stabilise the performance of negatively fed KM3NeT photomultipliers“. In: *Journal of Instrumentation* 11.12 (2016), P12014 (cit. on p. 74).

[89] G.F. Knoll. „Radiation detection and measurements“. In: *John Wiley Sons, Inc.* (1999) (cit. on p. 75).

[90] Brian Feldstein, Alexander Kusenko, Shigeki Matsumoto, and Tsutomu T. Yanagida. „Neutrinos at IceCube from heavy decaying dark matter“. In: *Phys. Rev. D* 88 (1 2013), p. 015004 (cit. on p. 81).

[91] Claudio Kopper. „Observation of Astrophysical Neutrinos in Six Years of IceCube Data“. In: *PoS* ICRC2017 (2018), p. 981 (cit. on pp. 81–83).

[92] Marco Chianese, Rosa Mele, Gennaro Miele, Pasquale Migliozzi, and Stefano Morisi. „Use of ANTARES and IceCube Data to Constrain a Single Power-law Neutrino Flux“. In: *Astrophys. J.* 851.1 (2017), p. 36. arXiv: 1707.05168 [hep-ph] (cit. on pp. 81, 85–87, 89).

[93] Eli Waxman and John Bahcall. „High energy neutrinos from astrophysical sources: An upper bound“. In: *Phys. Rev. D* 59 (2 1998), p. 023002 (cit. on p. 82).

[94] Chien-Yi Chen, P. S. Bhupal Dev, and Amarjit Soni. „Two-component flux explanation for the high energy neutrino events at IceCube“. In: *Phys. Rev. D* 92 (7 2015), p. 073001 (cit. on p. 82).

[95] Andrea Palladino, Maurizio Spurio, and Francesco Vissani. „On the IceCube spectral anomaly“. In: *Journal of Cosmology and Astroparticle Physics* 2016.12 (2016), p. 045 (cit. on p. 82).

[96] Andrea Palladino and Francesco Vissani. „Extragalactic plus Galactic Model for IceCube Neutrino Events“. In: *The Astrophysical Journal* 826.2 (2016), p. 185 (cit. on p. 82).

[97] M. G. Aartsen, K. Abraham, M. Ackermann, et al. „Observation and Characterization of a Cosmic Muon Neutrino Flux from the Northern Hemisphere Using Six Years of IceCube Data“. In: *The Astrophysical Journal* 833.1 (2016), p. 3 (cit. on pp. 82, 88, 89).

[98] M. Honda, T. Kajita, K. Kasahara, S. Midorikawa, and T. Sanuki. „Calculation of atmospheric neutrino flux using the interaction model calibrated with atmospheric muon data“. In: *Phys. Rev. D* 75 (4 2007), p. 043006 (cit. on p. 82).

[99] Rikard Enberg, Mary Hall Reno, and Ina Sarcevic. „Prompt neutrino fluxes from atmospheric charm“. In: *Phys. Rev. D* 78 (4 2008), p. 043005 (cit. on p. 82).

[100] M. G. Aartsen, R. Abbasi, M. Ackermann, et al. „Search for a diffuse flux of astrophysical muon neutrinos with the IceCube 59-string configuration“. In: *Phys. Rev. D* 89 (6 2014), p. 062007 (cit. on p. 82).

[101] M. G. Aartsen, M. Ackermann, J. Adams, et al. „Atmospheric and astrophysical neutrinos above 1 TeV interacting in IceCube“. In: *Phys. Rev. D* 91 (2 2015), p. 022001 (cit. on p. 82).

[102] Steve Baker and Robert D. Cousins. „Clarification of the use of CHI-square and likelihood functions in fits to histograms“. In: *Nuclear Instruments and Methods in Physics Research* 221.2 (1984), pp. 437 –442 (cit. on p. 82).

[103] IceCube Collaboration. „Evidence for High-Energy Extraterrestrial Neutrinos at the IceCube Detector“. In: *Science* 342.6161 (2013). eprint: http://science.sciencemag.org/content/342/6161/1242856.full.pdf (cit. on p. 83).

[104] M. Chianese, G. Miele, S. Morisi, and E. Vitagliano. „Low energy IceCube data and a possible Dark Matter related excess“. In: *Physics Letters B* 757 (2016), pp. 251 –256 (cit. on p. 86).

[105] Marvin Karson. „Handbook of Methods of Applied Statistics. Volume I: Techniques of Computation Descriptive Methods, and Statistical Inference. Volume II: Planning of Surveys and Experiments. I. M. Chakravarti, R. G. Laha, and J. Roy, New York, John Wiley; 1967, $9.00.“ In: *Journal of the American Statistical Association* 63.323 (1968), pp. 1047–1049. eprint: https://doi.org/10.1080/01621459.1968.11009335 (cit. on p. 88).

[106] Jialiang Li, Bee Choo Tai, and David J. Nott. „Confidence interval for the bootstrap P-value and sample size calculation of the bootstrap test“. In: *Journal of Nonparametric Statistics* 21.5 (2009), pp. 649–661. eprint: https://doi.org/10.1080/10485250902770035 (cit. on p. 88).

[107] E. Rodel. „Fisher, R. A.: Statistical Methods for Research Workers, 14. Aufl., Oliver & Boyd, Edinburgh, London 1970. XIII, 362 S., 12 Abb., 74 Tab., 40 s“. In: *Biometrische Zeitschrift* 13.6 (), pp. 429–430. eprint: https://onlinelibrary.wiley.com/doi/pdf/10.1002/bimj.19710130623 (cit. on p. 88).

[108] Chaimae El Aisati, Michael Gustafsson, and Thomas Hambye. „New Search for Monochromatic Neutrinos from Dark Matter Decay“. In: *Phys. Rev.* D92.12 (2015), p. 123515. arXiv: 1506.02657 [hep-ph] (cit. on p. 91).

[109] Julio F. Navarro, Carlos S. Frenk, and Simon White. „The Structure of Cold Dark Matter Halos“. In: *The Astrophysical Journal* 462 (Sept. 1995) (cit. on p. 91).

[110] Planck Collaboration, Ade, P. A. R., Aghanim, N., et al. „Planck 2015 results - XIII. Cosmological parameters“. In: *A&A* 594 (2016), A13 (cit. on p. 91).

[111] B. Hughey A. Karle G. C. Hill J. Hodges and M. Stamatikos. „Examining the balance between optimising an analysis for best limit setting and best discovery potential“. In: *Proceedings of PHYSTAT05* (2005) (cit. on p. 92).

[112] Vivek Agrawal, T. K. Gaisser, Paolo Lipari, and Todor Stanev. „Atmospheric neutrino flux above 1 GeV“. In: *Phys. Rev. D* 53 (3 1996), pp. 1314–1323 (cit. on p. 93).

[113] E. V. Bugaev, A. Misaki, V. A. Naumov, et al. „Atmospheric muon flux at sea level, underground, and underwater“. In: *Phys. Rev. D* 58 (5 1998), p. 054001 (cit. on p. 93).